

Formation of Super-Earth Mass Planets at 125–250 AU from a Solar-type Star

Scott J. Kenyon

Smithsonian Astrophysical Observatory, 60 Garden Street, Cambridge, MA 02138

e-mail: skenyon@cfa.harvard.edu

Benjamin C. Bromley

Department of Physics, University of Utah, 201 JFB, Salt Lake City, UT 84112

e-mail: bromley@physics.utah.edu

ABSTRACT

We investigate pathways for the formation of icy super-Earth mass planets orbiting at 125–250 AU around a $1 M_{\odot}$ star. An extensive suite of coagulation calculations demonstrates that swarms of 1 cm to 10 m planetesimals can form super-Earth mass planets on time scales of 1–3 Gyr. Collisional damping of 10^{-2} – 10^2 cm particles during oligarchic growth is a highlight of these simulations. In some situations, damping initiates a second runaway growth phase where 1000–3000 km protoplanets grow to super-Earth sizes. Our results establish the initial conditions and physical processes required for *in situ* formation of super-Earth planets at large distances from the host star. For nearby dusty disks in HD 107146, HD 202628, and HD 207129, ongoing super-Earth formation at 80–150 AU could produce gaps and other structures in the debris. In the solar system, forming a putative planet X at $a \lesssim 300$ AU ($a \gtrsim 1000$ AU) requires a modest (very massive) protosolar nebula.

Subject headings: planetary systems – planets and satellites: formation – solar system: formation

1. INTRODUCTION

For nearly a century, planet X has haunted the outer Solar System. Originally envisioned as a way to explain irregularities in the orbits of Uranus and Neptune (e.g., Lowell 1915; Bower 1931; Brouwer 1955; Rawlins 1970, 1972; Harrington 1988), planet X – along with the variants Nemesis and Tyche – has since been invoked to explain the orbital properties of some comets and trans-Neptunian objects (e.g., Matese et al. 1999; Gomes et al. 2006; Lykawka

& Mukai 2008) and apparent periodicities in mass extinction events on Earth (Davis et al. 1984; Whitmire & Jackson 1984). Generating these phenomena requires a massive planet X, \sim a few Earth masses to tens of Jupiter masses, with a semimajor axis $a \sim 200\text{--}20,000$ AU.

Observational and theoretical constraints severely limit possibilities for planet X (e.g., Hogg et al. 1991; Zakamska & Tremaine 2005; Iorio 2009; Fernández 2011). Along with improved mass measurements for Uranus and Neptune from *Voyager*, better analyses of positional data eliminate the need for a massive planet to explain any ‘irregularities’ in the orbits of Uranus and Neptune (e.g., Standish 1993). By excluding the possibility of a brown dwarf anywhere in the Solar System, a Jupiter-mass planet inside $\sim 25,000$ AU, and a Saturn-mass planet inside $\sim 10,000$ AU, observations from the *IRAS*, *2MASS*, and *WISE* all-sky infrared surveys specifically rule out Nemesis and some other variants of planet X (e.g., Luhman 2014).

The recent discovery of 2012 VP₁₁₃ (Trujillo & Sheppard 2014) in the ‘inner Oort cloud’ has renewed interest in planet X. With orbital parameters similar to those of Sedna¹, 2012 VP₁₁₃ joins a group of a dozen relatively large ($R \approx 200\text{--}1000$ km) distant objects ($q_p \geq 30$ AU, $e \gtrsim 0.7$) with arguments of perihelion $\omega \approx 0^\circ$. The observed distribution of ω for these objects is statistically unlikely (see also de la Fuente Marcos & de la Fuente Marcos 2014). Although dynamical interactions between the young Sun and a passing star can produce objects on highly eccentric orbits like Sedna and 2012 VP₁₁₃ (e.g., Morbidelli & Levison 2004; Kenyon & Bromley 2004c), the known planets randomize ω on 0.1–1 Gyr time scales (Gomes et al. 2006; Lykawka & Mukai 2008; Trujillo & Sheppard 2014). Super-Earth mass planets at $a \approx 200\text{--}300$ AU can maintain the observed distribution of ω for the age of the Solar System (Trujillo & Sheppard 2014; de la Fuente Marcos & de la Fuente Marcos 2014; Iorio 2014).

In addition to explaining the orbital dynamics of objects beyond 40–50 AU, identifying one or more Earth-mass planets with $a \sim 200$ AU has interesting implications for the architecture of the Solar System beyond Neptune. Despite a lack of massive planets with $a \gtrsim 35$ AU, there is a diverse set of trans-Neptunian objects with radii $R \lesssim 1000\text{--}2000$ km on orbits with a broad range of e and i (e.g., Gladman et al. 2008; Petit et al. 2011). Aside from objects like Sedna and 2012 VP₁₁₃, the distribution of semimajor axes for these objects suggests a clear ‘edge’ at roughly 48 AU. Confirming a massive planet at ~ 200 AU might imply a very large reservoir of material beyond this edge.

Establishing the existence of a massive planet beyond 100 AU has profound consequences for the origin of the Solar System. In current theory, planets grow out of material orbiting within a circumsolar disk of gas and dust. As the gaseous disk dissipates, these planets (i)

¹Sedna: semimajor axis $a = 542$ AU, eccentricity $e = 0.86$, and perihelion distance $q_p = a(1 - e) = 76.23$ AU; 2012 VP₁₁₃: $a = 266$ AU, $e = 0.698$ AU, and $q_p = 80$ AU

clear out material along their orbits and (ii) migrate radially to a more stable orbit (e.g., Youdin & Kenyon 2013; Morbidelli 2013). If an extra super-Earth forms with the known gas giants at $a \approx 10\text{--}20$ AU before the gaseous disk disappears, this planet could migrate radially to much larger semimajor axes as in models for Fomalhaut b (Crida et al. 2009).

Planet-planet scattering is a promising alternative to radial migration (Bromley & Kenyon 2014). In this picture, several massive planets form out of disk material at 5–10 AU. Close orbital encounters among these planets then scatter lower mass planets to large semimajor axes (e.g., Rasio & Ford 1996; Levison et al. 1998; Jurić & Tremaine 2008; Bromley & Kenyon 2011a). If the gaseous component of the disk is massive and extends to 125–250 AU, gas drag and dynamical friction can circularize the orbits of super-Earth-mass planets on time scales comparable to the disk lifetime. Because lower mass planets are left on eccentric orbits, measuring the orbital elements of any planet with $a \gtrsim 100$ AU constrains the mass and outer radius of the solar nebula (Bromley & Kenyon 2014).

Establishing the orbital eccentricity of a super-Earth at 200 AU provides a way to distinguish between these two possibilities. Migrating planets have nearly circular orbits (e.g., Ward 1997; Masset & Papaloizou 2003; Ida & Lin 2008; Crida et al. 2009). Although gas drag can produce nearly circular orbits among scattered massive planets, lower mass planets have more eccentric orbits (Bromley & Kenyon 2014).

To provide a distinct set of predictions for massive planets at 200 AU, we consider models where one or more super-Earths form directly out of solid material well beyond the outer edge of the Kuiper belt (see also Stern 2005; Kenyon & Bromley 2008, 2010, 2012). After summarizing several issues of growth at semimajor axes $a \approx 125\text{--}250$ AU (§2), we describe numerical simulations of planet formation for a variety of initial particle sizes and input parameters (§3–4). Within a ring of width $\delta a \approx 0.2a$ and total mass $M_0 \approx 15 M_\oplus$, ensembles of 1 cm to 10 m particles grow into super-Earth mass planets on time scales of 1–2 Gyr at 125–250 AU. After considering the implications of these results (§5), our discussion concludes with a brief summary (§6).

2. BACKGROUND

In the current core accretion theory, planets form in circumstellar disks of gas and dust (e.g., Goldreich et al. 2004; Chiang & Youdin 2010; Youdin & Kenyon 2013). After micron-sized grains within the disk agglomerate into cm-sized objects (e.g., Birnstiel et al. 2010), continued coagulation (e.g., Windmark et al. 2012; Garaud et al. 2013) or some type of instability (e.g., Youdin & Goodman 2005; Johansen et al. 2012) concentrates solids into km-sized or larger planetesimals. When most of the solids end up in planetesimals, these objects collide, merge, and grow into planets (e.g., Kenyon & Bromley 2006; Chambers 2008; Kenyon & Bromley 2008; Kobayashi et al. 2010; Raymond et al. 2011). In a popular variant

of this picture, coagulation or instabilities produce only a few large planetesimals, which then rapidly accrete cm-sized pebbles (Ormel & Klahr 2010; Bromley & Kenyon 2011a; Lambrechts & Johansen 2012, 2014; Chambers 2014).

Here, we focus on the growth of large swarms of planetesimals into super-Earth mass planets. When planetesimals form, their relative velocities are small. Physical collisions among planetesimals yield larger, merged objects. As planetesimals merge into larger and larger protoplanets, dynamical friction and viscous stirring excite the orbits of all the solids (e.g., Wetherill & Stewart 1989; Ida & Makino 1992a,b; Wetherill & Stewart 1993; Goldreich et al. 2004). Relative collision velocities grow in step with the escape velocity of the largest protoplanet. Eventually, collisions between small planetesimals produce debris instead of mergers. Collisions between debris particles make even more debris. The resulting collisional cascade grinds the debris into small dust grains; radiation pressure ejects these grains from the nascent planetary system (e.g., Dohnanyi 1969; Burns et al. 1979; Williams & Wetherill 1994). Together, the collisional cascade and radiation pressure typically remove 80% to 95% of the initial mass in solids from the outer disk of a planetary system (Kenyon & Bromley 2002b, 2008, 2010; Kobayashi et al. 2010). As a result, the largest planets have maximum radii of $\sim 3000\text{--}7000$ km and maximum masses of $0.1\text{--}0.5 M_{\oplus}$ (e.g., Kenyon 2002; Kenyon & Bromley 2002b; Inaba et al. 2003; Kenyon & Bromley 2008, 2010; Kobayashi et al. 2010).

Within this evolutionary sequence, there are several ways to limit the loss of small objects and to promote the formation of super-Earth mass planets at 125–250 AU.

- Increase the binding energy Q_D^* of small planetesimals. Larger binding energies delay the collisional cascade, allowing protoplanets to grow to larger sizes.
- Change the size distribution of the fragments produced in a collision. If the fragments have a steeper size distribution, it takes longer for the collisional cascade to grind them to dust. Longer collisional cascades enable larger protoplanets.
- Include collisional damping of the smallest objects. If collisional damping can reduce the velocities of small collision fragments, collisional grinding proceeds more slowly and protoplanets grow larger.

Of these options, modifying Q_D^* seems the least realistic. Modest changes to Q_D^* consistent with numerical simulations of the binding energy for small objects (e.g., Benz & Asphaug 1999; Leinhardt & Stewart 2009, 2012) lead to factor of ~ 2 changes in the mass of the largest object (e.g., Kenyon & Bromley 2010; Kobayashi et al. 2010; Kenyon & Bromley 2012). Achieving much larger protoplanets requires factor of $\gtrsim 10$ increases in the binding energy of 0.1–10 km objects. Calculations of the likely structure of these objects appear to preclude such large increases in Q_D^* . Thus, we eliminate this possibility.

Modifying the size distribution of the fragments is more promising. In all numerical simulations of planet formation, the size distribution of the debris is a power law $n(r) \propto r^{-q}$ with a maximum size $r_{max,d}$ and a minimum size $r_{min,d}$ (e.g., Wetherill & Stewart 1993; Kenyon & Luu 1999; O’Brien & Greenberg 2003; Kenyon & Bromley 2004a; Chambers 2008; Morbidelli et al. 2009; Kobayashi et al. 2010; Weidenschilling 2010). If m_{esc} is the mass in fragments, defining $r_{max,d}$ and q establishes the mass distribution uniquely (e.g., Kenyon et al. 2014). Many investigators set $r_{max,d} \approx \gamma r_{esc}$ where r_{esc} is the radius of a particle with mass m_{esc} and $\gamma \approx 0.1$ – 0.3 . Because the equilibrium size distribution for a collisional cascade has $q \approx 3.5$ – 3.7 (Dohnanyi 1969; Williams & Wetherill 1994; O’Brien & Greenberg 2003), many investigators fix $q = 3.5$. Although others employ more complicated formulae for $r_{max,d}$ and q (Morbidelli et al. 2009; Weidenschilling 2010), these also require $q \lesssim 4.0$ at small sizes.

In contrast to these restrictive approaches, detailed numerical simulations of binary collisions between planetesimals often yield debris with steep size distributions (e.g., Durda et al. 2004, 2007; Leinhardt & Stewart 2012). For planetesimal radii $R_0 \approx 10$ – 100 km, the debris has typical $r_{max,d} \approx 0.1$ – $1.0 R_0$. The smallest debris particles have sizes equal to the smallest size resolved in the calculation, $r_{min,d} \sim 0.1$ – 1 km. Over this range of sizes, the slope of the size distribution depends on the ratio r_c of the collision energy to the binding energy. Collisions with larger r_c have larger q . For $r_c \gtrsim 1$, extreme values for the slope of the size distribution are $q \approx 4$ – 6 (Leinhardt & Stewart 2012) or $q \approx 8$ – 10 (Durda et al. 2004; Morbidelli et al. 2009).

In addition to exploring calculations with a range in q , it is important to consider the impact of collisional damping on the cascade (Goldreich et al. 2004). For typical surface densities of solid particles, collisional damping is effective for particle sizes of 1–10 mm (see also Kenyon & Bromley 2002a, 2014). Numerical simulations which follow such small particles generally do not include collisional damping (e.g., Stark & Kuchner 2009; Thébault et al. 2012; Gáspár et al. 2013). Calculations which include collisional damping rarely follow particles with sizes smaller than 1 cm (e.g., Wetherill & Stewart 1993; Kenyon & Bromley 2008; Morbidelli et al. 2009; Kobayashi et al. 2010; Weidenschilling 2010; Kobayashi & Löhne 2014). Thus, it is possible that a full evolutionary calculation with particle sizes smaller than 1 cm will yield new phenomena.

In the following section, we outline the tools we use to calculate the evolution of a swarm of particles with sizes of $1 \mu\text{m}$ to $\gtrsim 10^4$ km. The Appendix summarizes several tests of our algorithms and comparisons with results of other approaches. Once the approach is set, §4 describes results for evolutionary calculations at 125–250 AU.

3. PLANET FORMATION CALCULATIONS

Over the past decade, we have developed *Orchestra*, an ensemble of computer codes for the formation and evolution of planetary systems. *Orchestra* consists of a radial diffusion code which derives the time evolution of a gaseous or a particulate disk (Bromley & Kenyon 2011a), a multiannulus coagulation code which infers the time evolution of a swarm of planetesimals (Kenyon & Bromley 2004a, 2008, 2012), and an n -body code which follows the orbits of gravitationally interacting protoplanets (Bromley & Kenyon 2006, 2011b, 2013). Within the coagulation code, *Orchestra* includes algorithms for treating interactions between small particles and the gaseous disk (e.g., Adachi et al. 1976; Weidenschilling 1977) and between coagulation mass bins and n -bodies (Bromley & Kenyon 2006). To treat interactions between small particles and the n -bodies more rigorously, the n -body calculations include tracer particles. Massless tracer particles allow us to calculate the evolution of the orbits of small particles in response to the motions of massive protoplanets. Massless and massive tracer particles enable calculations of the response of n -bodies to the changing gravitational potential of small particles (Bromley & Kenyon 2011a,b, 2013).

3.1. Numerical Grid

To explore a reasonable parameter space with good statistics, we perform coagulation calculations within a single annulus with semimajor axis a and width δa around a star with mass $M_\star = 1 M_\odot$. Within this annulus, there are M mass batches with characteristic mass m_k and radius r_k (Wetherill & Stewart 1993; Kenyon & Luu 1998). Batches are logarithmically spaced in mass, with mass ratio $\delta \equiv m_{k+1}/m_k$. Each mass batch contains N_k particles with total mass M_k and average mass $\bar{m}_k = M_k/N_k$. Particle numbers $N_k < 10^{15}$ are always integers. Throughout the calculation, the average mass is used to calculate the average physical radius \bar{r}_k , collision cross-section, collision energy, and other necessary physical variables. As mass is added and removed from each batch, the average mass changes (Wetherill & Stewart 1993).

For any δ , numerical calculations lag the result of an ideal calculation with infinite mass resolution (see the Appendix). At $a = 125$ – 250 AU, calculations with $\delta = 1.05$ – 1.19 yield better solutions to the growth of 100+ km objects than calculations with $\delta = 1.41$ – 2.00 . Although simulations with $\delta = 1.05$ – 1.10 allow somewhat better tracking of the late stages of planet growth, the improvement over results with $\delta = 1.19$ does not compensate for the factor of 2–4 extra cpu time required to complete these calculations. Thus, we consider a suite of calculations with $\delta = 1.19$ ($= 2^{1/4}$).

In this suite of calculations, we follow particles with sizes ranging from a minimum size $r_{min} = 1 \mu\text{m}$ to the maximum size in the annulus r_{max} . The algorithm for assigning material to the mass bins extends the maximum size as needed to accommodate the largest particles.

Typically, the number of large objects with $r_{max} \gtrsim 1000$ km in each calculation is small $N_k \lesssim 10$; each protoplanet generally lies in its own mass bin. To conserve cpu time, we do not promote these objects into the n -body code.

3.2. Initial Conditions

All calculations begin with a mono-disperse swarm of planetesimals with initial size r_0 and mass density $\rho_p = 1.5 \text{ g cm}^{-3}$. These particles have initial surface density Σ_0 , total mass M_0 , and horizontal and vertical velocities h_0 and v_0 relative to a circular orbit. The horizontal velocity is related to the orbital eccentricity, $e = 1.6 (h/V_K)^2$, where V_K is the circular orbital velocity. The orbital inclination is $\sin i = \sqrt{2}v/V_K$.

For conditions at 125–250 AU, typical growth times are longer than the 1–5 Myr lifetime of the gaseous disk (Haisch et al. 2001; Williams & Cieza 2011; Cloutier et al. 2014). Thus, we set the initial surface density of the gas to zero and ignore gas drag on small solids (Adachi et al. 1976; Weidenschilling 1977; Rafikov 2004). Compared to calculations which include gas drag (e.g., Wetherill & Stewart 1993; Chambers 2008; Kenyon & Bromley 2008; Kobayashi et al. 2010), our simulations retain a larger fraction of small particles which might experience significant radial drift during the likely lifetime of the gaseous disk. However, our goal is to isolate initial conditions and physical processes which might allow formation of super-Earths at 125–250 AU. We plan to consider the impact of gas drag in future papers.

3.3. Evolution

The mass and velocity distributions of the planetesimals evolve in time due to inelastic collisions, drag forces, and gravitational encounters. As summarized in Kenyon & Bromley (2004a, 2008), we solve a coupled set of coagulation equations which treats the outcomes of mutual collisions between all particles in all mass bins. We adopt the particle-in-a-box algorithm, where the physical collision rate is $n\sigma v f_g$, n is the number density of objects, σ is the geometric cross-section, v is the relative velocity, and f_g is the gravitational focusing factor (Wetherill & Stewart 1993; Kenyon & Luu 1998). Depending on physical conditions in the disk, we derive f_g in the dispersion or the shear regime (Kenyon & Luu 1998; Kenyon & Bromley 2012). For a specific mass bin, the solutions include terms for (i) loss of mass from mergers with other objects and (ii) gain of mass from collisional debris and mergers of smaller objects.

As discussed in Wetherill & Stewart (1993), the most massive protoplanets on roughly circular orbits are ‘isolated’ from one another. Isolated protoplanets can accrete smaller objects but cannot collide with other isolated protoplanets. To identify isolated protoplanets, we find an ensemble of the largest objects whose combined gravitational range is smaller than

the width of the annulus. For an individual protoplanet, the gravitational range is

$$R_{g,k} = KaR_{H,kk} + 2ae_k \quad (1)$$

Here, $K = 2\sqrt{3}$ and $R_{H,kk} = [(m_k + m_k)/3M_\odot]^{1/3}$ is the mutual Hill radius. The gravitational ranges of the isolated protoplanets satisfy the summation,

$$\sum_{k_{min}}^{k_{max}} n_k R_{g,k} \leq \delta a, \quad (2)$$

where n_k is the number of protoplanets in mass bin k .

Collision outcomes depend on the ratio Q_c/Q_D^* , where Q_D^* is the collision energy needed to eject half the mass of a pair of colliding planetesimals to infinity and Q_c is the center of mass collision energy (see also Wetherill & Stewart 1993; Williams & Wetherill 1994; Tanaka et al. 1996; Stern & Colwell 1997; Kenyon & Luu 1999; O’Brien & Greenberg 2003; Kobayashi & Tanaka 2010). Following Wetherill & Stewart (1993), two colliding planetesimals with horizontal velocity h_1, h_2 and vertical velocity v_1, v_2 have relative horizontal and vertical velocities $h_c = (h_1^2 + h_2^2)^{1/2}$ and $v_c = (v_1^2 + v_2^2)^{1/2}$ (see also Kenyon & Luu 1998). The escape velocity of the colliding pair is $v_{esc} = (2Gm_c/r_c)^{1/2}$, where $m_c = m_1 + m_2$ is the combined mass and $r_c = r_1 + r_2$ is the combined radius. The center of mass collision energy is then

$$Q_c = 0.5\mu(h_c^2 + v_c^2 + v_{esc}^2)/m_c \quad (3)$$

where $\mu = m_1 m_2 / m_c$ is the reduced mass.

Consistent with N-body simulations of collision outcomes (e.g., Benz & Asphaug 1999; Leinhardt et al. 2008; Leinhardt & Stewart 2009), we set

$$Q_D^* = Q_b r^{\beta_b} + Q_g \rho_p r^{\beta_g} \quad (4)$$

where $Q_b r^{\beta_b}$ is the bulk component of the binding energy, $Q_g \rho_p r^{\beta_g}$ is the gravity component of the binding energy, and r is the radius of a planetesimal.

In this study, planetesimals have $Q_b = 2 \times 10^5 \text{ erg g}^{-1} \text{ cm}^{0.4}$, $\beta_b = -0.40$, $Q_g = 0.22 \text{ erg g}^{-2} \text{ cm}^{1.7}$, and $\beta_g = 1.30$. These parameters are broadly consistent with published analytic and numerical simulations (e.g., Davis et al. 1985; Holsapple 1994; Love & Ahrens 1996; Housen & Holsapple 1999). At small sizes, they agree with results from laboratory (e.g., Ryan et al. 1999; Arakawa et al. 2002; Giblin et al. 2004; Burchell et al. 2005) and numerical (e.g., Leinhardt & Stewart 2009) experiments of impacts between icy objects. For the weakest objects with $r \approx 10\text{--}100 \text{ m}$, our adopted Q_D^* is a factor of 3–10 smaller than in other studies (e.g., Bottke et al. 2010). Thus, our small planetesimals are relatively weak and easy to break.

For two colliding planetesimals with masses m_1 and m_2 , the mass of the merged planetesimal is

$$m = m_1 + m_2 - m_{esc}, \quad (5)$$

where the mass of debris ejected in a collision is

$$m_{esc} = 0.5 (m_1 + m_2) \left(\frac{Q_c}{Q_D^*} \right)^b. \quad (6)$$

The exponent b is a constant of order unity (e.g., Davis et al. 1985; Wetherill & Stewart 1993; Kenyon & Luu 1999; Benz & Asphaug 1999; O’Brien & Greenberg 2003; Leinhardt & Stewart 2012). In previous calculations, we adopted $b = 9/8$; here, we also consider $b = 1$ (see also Kobayashi & Tanaka 2010; Kobayashi et al. 2010).

To place the debris in the grid of mass bins, we set the mass of the largest collision fragment as $m_{max,d} = 0.2 m_{esc}$ and adopt a differential size distribution $n(r) \propto r^{-q}$. After placing a single object with mass $m_{max,d}$ in the grid, we place material in successively smaller mass bins until (i) the mass is exhausted or (ii) mass is placed in the smallest mass bin. Any material left over is removed from the grid. To explore a broad range of q (§2), we derive results for $q = 3.5, 4.0, 4.5, 4.5, 5.0, \text{ and } 5.5$.

To illustrate the general impact of b and q on the evolution, we consider two simple examples. When $Q_c/Q_D^* = 0.5$ (early in the evolution), our approach yields $(m_{esc}, m_{max,d}) = (0.25, 0.05) m_c$ when $b = 1$ and $(0.23, 0.045) m_c$ when $b = 9/8$. The larger exponent results in less debris which is placed in bins with smaller average mass. When $Q_c/Q_D^* = 1.5$ (late in the evolution), $(m_{esc}, m_{max,d}) = (0.75, 0.15) m_c$ when $b = 1$ and $(0.79, 0.16) m_c$ when $b = 9/8$. The larger exponent produces more debris which is placed in bins with larger average mass. More debris makes collisional damping and dynamical friction more effective, which enhances the growth of the largest objects. Thus, the smaller (larger) exponent tends to enhance (retard) growth early in the evolution at the expense of slower (more rapid) growth later in the evolution.

The broad range of q we consider has a similar impact on the timing and magnitude of runaway growth. When the size distribution is shallow ($q = 3.5\text{-}4.0$), debris is placed in a broad range of mass bins, limiting the impact of collisional damping and dynamical friction. When q is larger, debris is placed in a narrower range of mass bins, enhancing the impact of collisional damping and dynamical friction. Overall, we then expect calculations with larger q and larger b to have faster growth; calculations with smaller q and smaller b have slower growth. In §4, we discuss the impact of these choices in more detail.

As we place the debris in specific mass bins, we also redistribute the kinetic energy per unit mass of each colliding pair of planetesimals. As in Kenyon & Luu (1998), we assume all collisions between mass batches conserve the horizontal and vertical components of kinetic energy. For an initial kinetic energy, $m_1(h_1^2 + v_1^2) + m_2(h_2^2 + v_2^2)$, any merged planetesimal with mass m receives a fraction $m/(m_1 + m_2)$ of this kinetic energy; any fragment with mass m_f receives a fraction $m_f/(m_1 + m_2)$. Recalling the center of mass collision energy from eq. (3), this approach assumes that the escape velocity component of the collision energy is equal to the energy required to disperse the fragments to infinity.

To compute the evolution of the velocity distribution, we also include collisional damping from inelastic collisions and gravitational interactions. For inelastic and elastic collisions, we follow the statistical, Fokker-Planck approaches of Ohtsuki (1999) and Ohtsuki et al. (2002), which treat pairwise interactions (e.g., dynamical friction and viscous stirring) between all objects. For evaluating these interactions within a single annulus, we eliminate terms to calculate the probability that objects in one annulus interact with objects in other annuli (Kenyon & Bromley 2001, 2004b, 2008). We also compute long-range stirring from distant oligarchs (Weidenschilling 1989). The Appendix describes several tests of these algorithms.

4. EVOLUTION OF THE LARGEST OBJECTS

To evolve a sea of mono-disperse planetesimals in a single annulus, we set the size r_0 , the surface density Σ_0 , and the orbital elements e_0 and i_0 . For these simulations, $r_0 = 10^n$ cm where n is an integer between 0 and 8 inclusive. Beyond the snow line, the standard minimum mass solar nebula has $\Sigma \approx 30 \text{ g cm}^{-2} (a/1 \text{ AU})^{-3/2}$ (Kenyon & Bromley 2008), which implies $\Sigma = 0.0215 \text{ g cm}^{-2}$ at $a = 125 \text{ AU}$. In an annulus with $\delta a = 0.2a$, the total mass is $M_0 = 15.8 M_\oplus$. For simplicity, we adopt the same mass in an annulus at 250 AU. In this annulus, $\Sigma = 5.37 \times 10^{-3} \text{ g cm}^{-2}$, roughly 70% of the surface density of a minimum mass solar nebula extrapolated to 250 AU. Previous calculations suggest the growth time for large objects scales inversely with the mass in solid objects (Kenyon & Luu 1999; Kenyon & Bromley 2002b, 2008, 2010). Thus, we consider only one surface density.

In most published simulations, the initial orbital elements of planetesimals are set to match the escape velocity of the largest objects (e.g., Kobayashi et al. 2010; Weidenschilling 2010). For particles with $r_0 \gtrsim 10\text{--}100$ m at 125–250 AU, the time scale to reach equilibrium is longer than the 1–5 Myr lifetime of the gaseous disk (Appendix). Here, we set $i_0 = e_0/2$ and adopt $e_0 = 10^{-4}$ for $r_0 = 1$ cm to 1 km, $e_0 = 10^{-3}$ for $r_0 = 10$ km, and $e_0 = 10^{-2}$ for $r_0 = 100\text{--}1000$ km. For the adopted Σ at 125–250 AU and these e_0 , swarms of particles are gravitationally stable and have e_0 intermediate between the likely e for particles within a turbulent gaseous disk and an equilibrium e set by a balance between stirring and damping (Appendix). After describing results for these initial conditions, we consider how different choices impact the results.

In the next two sub-sections, we focus on the evolution of the largest objects at 125 AU (§4.1) and at 250 AU (§4.2). We then conclude this section with a brief discussion of the limitations of our calculations.

4.1. Results at 125 AU

4.1.1. Super-Earth Formation

Without gas drag, all calculations follow a similar pattern (e.g., Kenyon 2002; Kenyon & Bromley 2002b, 2004a, 2008, 2010). Starting from a mono-disperse set of planetesimals, collisions produce mergers and negligible debris. Growth of larger planetesimals allows dynamical friction to circularize the orbits of the largest particles at the expense of raising the e and i of the smallest particles. Collisional damping gradually reduces the velocities of the smallest objects. Eventually, significant gravitational focusing factors enable runaway growth, where the largest planetesimals grow rapidly by factors of 10–100. As these protoplanets grow, viscous stirring raises the velocities of smaller planetesimals. Gravitational focusing factors diminish considerably. Runaway growth ends; oligarchic growth begins. Throughout oligarchic growth, collisions produce more and more debris. Once protoplanets reach radii of 1000 km or larger, the collisional cascade tries to remove nearly all of the small particles remaining in the annulus. As the cascade proceeds, protoplanets reach a maximum radius which remains fixed for the rest of the calculation.

When $b = 9/8$ and $q = 3.5$, protoplanets reach radii of 1000 km or larger in roughly 1 Gyr (Fig. 1). In all calculations, growth starts slowly. Ensembles of 1 cm particles take $\sim 10^5$ yr to reach 10 cm sizes and another $\sim 10^6$ yr to reach 1 m sizes. After a very brief period of runaway growth, the largest objects have $r_{max} \approx 0.1$ – 0.3 km and make the transition to oligarchic growth. Large protoplanets then reach 100 km sizes in 200–300 Myr. During a second period of runaway growth at 300–500 Myr, protoplanets grow past 1000 km. Some reach sizes of 5000–7000 km. We address the origin of this second phase of runaway growth in §4.1.2.

Calculations starting with larger planetesimals follow the same steps. For $r_0 = 1$ cm to 1 km, the time scale to reach the first runaway growth phase increases roughly linearly with the initial particle size. When $r_0 = 10$ – 1000 km, the largest planetesimals endure a long phase of slow growth, make a smooth transition to oligarchic growth, and then gradually accumulate enough material to reach sizes of 500–3000 km.

This evolution is fairly independent of b (Fig. 2). At the smallest sizes ($r_0 \approx 1$ cm to 1 km), the evolution of $r_{max}(t)$ for $b = 1$ is nearly identical to the evolution for $b = 9/8$. Because planetesimals with $r_0 = 100$ – 1000 km hardly grow in 10 Gyr, this evolution is also insensitive of b . For 10 km objects, however, growth is somewhat faster when $b = 1$ than when $b = 9/8$. In our suite of calculations, it takes 150–175 Myr (225–275 Myr) to produce 100 km objects and 1000–1250 Gyr (1250–1250 Myr) to produce 1000 km objects when $b = 1$ ($b = 9/8$). The relative abundance of lower mass fragments causes this difference. During slow growth, calculations with $b = 1$ produce somewhat more fragments than calculations with $b = 9/8$. The larger population of fragments circularizes the orbits of the largest protoplanets

more effectively, enabling a stronger runaway growth phase. Despite this difference, the largest protoplanets reach sizes of roughly 5000 km for all b .

To test the sensitivity of these results to stochastic variations within each simulation, we perform 5–10 calculations for $q = 3.5$ and each combination of b and r_0 . For $b = 9/8$ and $r_0 = 1$ cm to 0.1 km, the largest objects have radii $r_{max} \approx 3000$ –4500 km, with a median size $r_{max} \approx 3500$ km. With $r_0 = 1$ km, the median $r_{max} \approx 6900$ km; the median r_{max} drops to 4700 km for $r_0 = 10$ km. Ensembles of larger planetesimals grow very little: $r_{max} = 500$ km for $r_0 = 100$ km and $r_{max} = 1500$ km for $r_0 = 1000$ km.

When $b = 1$, protoplanets typically reach smaller maximum sizes. Among the suite of calculations, variations in r_{max} are similar to those for $b = 9/8$, 8% to 10% for sets of 5–10 calculations with identical starting conditions. However, the median r_{max} is 10% to 15% smaller. When $b = 1$, two factors conspire to produce smaller protoplanets. During runaway and the early stages of oligarchic growth, collisions produce more debris when $b = 1$. At this time, collisional damping is ineffective. Thus, calculations with $b = 1$ lose somewhat more mass from the grid than those with $b = 9/8$. Throughout the late stages of oligarchic growth and the second phase of runaway growth, relative particle velocities are much larger. Collisions then produce more debris when $b = 9/8$. With so much debris, collisional damping becomes more effective for calculations with $b = 9/8$ than those with $b = 1$. Damping promotes the growth of super-Earths, which are therefore more common when $b = 9/8$.

Although protoplanets with $r_{max} = 3000$ –7000 km are characteristic of growth with $q = 3.5$, the largest protoplanets in several calculations reach sizes exceeding 10^4 km ($m \gtrsim 1 M_{\oplus}$). Each of these simulations yields 2–3 super-Earths. For $r_0 = 1$ cm to 10 km, 3% (2%) of simulations with $b = 9/8$ (1) produce super-Earth mass planets. Each of these examples began with small planetesimals, $r_0 \leq 100$ cm; however, small number statistics precludes correlating occasional super-Earth formation with r_0 .

Super-Earth formation is much more common in calculations with $q \gtrsim 4.5$ (Fig. 3). For all q , protoplanets grow at similar rates for 100 Myr to 1 Gyr. At later times, protoplanets in calculations with $q \gtrsim 4.5$ grow much more rapidly. In simulations with $r_0 = 1$ cm to 1 km and $b = 9/8$, protoplanets reach median maximum sizes $r_{max} \approx 9000$ –12000 km ($m \approx 0.75$ –1.8 M_{\oplus}). The variations about the medians are much larger, $\sim 20\%$ to 25% instead of the 10% range for $q = 3.5$ –4.0. When $r_0 = 10$ km, maximum sizes are roughly 20% smaller. None of the simulations with larger planetesimals ($r_0 \gtrsim 10$ km) yields a super-Earth.

Results for $b = 1$ are similar. Suites of simulations with identical starting conditions have typical protoplanet radii of 7500–10000 km, roughly 15% smaller than calculations with $b = 9/8$. Because the variations about the median size are large, $\sim 25\%$, many simulations with $b = 1$ and $r_0 = 1$ cm to 1 km produce super-Earth mass planets. Ensembles of larger protoplanets with $r_0 \gtrsim 10$ km never produce super-Earths.

Figs. 4–5 summarize results for r_{max} as a function of b , r_0 , and q . When $r_0 = 1$ cm to 0.1 km, $b = 9/8$, and $q = 3.5$ or 4, fewer than 5% of all simulations produce super-Earth mass planets (Fig. 4). Although rings composed of larger planetesimals ($r_0 = 1$ km) usually yield more massive planets when $q = 3.5$ or 4, super-Earths are still rare. In contrast, super-Earths form in more than half of the simulations with $r_0 = 1$ cm to 1 km and $q = 4.5, 5$, or 5.5. When $b = 1$ and $q = 4.5, 5$, or 5.5, super-Earth formation is somewhat less common (Fig. 5). With $r_0 \lesssim 1$ km, super-Earths form in roughly 25% of the simulations with $q \gtrsim 4.5$. Among simulations with $q \lesssim 4$, super-Earth formation is rare.

4.1.2. Collisional Damping when $q = 3.5$ – 4.0

Compared to previous calculations of planet formation at 100–150 AU with similar starting conditions and fragmentation parameters, our new calculations yield fairly similar results. Published multiannulus calculations at 100–150 AU with identical fragmentation parameters and $q = 3.4$ have a median $r_{max} \approx 1250$ km (Kenyon & Bromley 2010). In the calculations for this paper with $q = 3.4$ (3.5), the median r_{max} is 1500–2000 km (2000–3000 km). By neglecting gas drag and including the evolution of small particles with radii smaller than 1 m, the calculations in this paper produce somewhat more massive large objects.

Although the new calculations allow the growth of larger objects when $q = 3.4$ – 3.5 , the collisional cascade still converts most of the initial solid mass into particles with sizes smaller than 1 μ m. Radiation pressure rapidly ejects these particles. In Kenyon & Bromley (2010), the cascade removes from 0.1% ($r_0 = 100$ km) to 90% ($r_0 = 1$ km) of the initial mass. Our new results suggest a weak dependence of mass loss on the initial planetesimal radius for small planetesimals; the cascade removes 80% of the initial mass when $r_0 = 1$ cm and more than 90% when $r_0 = 1$ km. When $r_0 \gtrsim 10$ km, the cascade removes very little mass as in the Kenyon & Bromley (2010) simulations; the slow evolution of swarms of large planetesimals then prevents the formation of large planets (see also Kenyon & Bromley 2010).

Despite the rough similarity in r_{max} and the ejected mass among these simulations, the time evolution of the size distribution is very different. In previous multiannulus simulations, the cumulative size distribution can be split into three power-laws (e.g., Kenyon & Bromley 2004d):

$$n_c(r) = \begin{cases} n_s r^{-q_s} & r \leq r_2 \\ n_i r^{-q_i} & r_2 \leq r < r_1 \\ n_l r^{-q_l} & r \geq r_1 \end{cases} \quad (7)$$

Here, $r_1 \approx 10$ – 100 km, $r_2 \approx 0.1$ – 1 km, $q_s \approx 2.5$ – 2.7 , $q_i \approx 0$ – 2 , and $q_l \approx 3$ – 4 (see also Kenyon & Bromley 2012). Growth sets the slope at large sizes, $r \geq r_1$; collisional debris is responsible

for the slope at small sizes, $r \leq r_2$ (Kenyon & Bromley 2004d, 2008, 2012; Pan & Sari 2005; Schlichting & Sari 2011; Schlichting et al. 2013). At intermediate sizes, competition between collisional destruction and debris production sets the slope.

To visualize the evolution of the size distribution in the new simulations, we normalize the cumulative size distribution to the expected size distribution at small sizes, $n_{c,rel}(r) = n_c(r)/n_s r^{-q_s}$. With this normalization, the expected cumulative size distribution is:

$$n_{c,rel}(r) = \begin{cases} 1 & r \leq r_2 \\ n_2 r^{q_s - q_i} & r_2 \leq r < r_1 \\ n_1 r^{q_s - q_l} & r \geq r_1 \end{cases} \quad (8)$$

For this expression, we set $n_1 = n_l/n_s$ and $n_2 = n_i/n_s$.

Fig. 6 illustrates some of the advantages of the relative size distribution. In the lower panel, three cumulative size distributions with different power-law components look fairly similar. Shifting to the relative size distribution in the upper panel, the three curves are very distinct. With $q_i < q_s < q_l$, the relative cumulative size distribution rises from r_2 to r_1 and then falls from r_1 to r_{max} . This normalization makes it fairly easy to infer r_1 and r_2 from the breaks in the relative size distribution.

Fig. 7 shows the evolution of the cumulative relative size distribution for the first 300 Myr of a calculation with $r_0 = 1$ cm, $b = 9/8$, and $q = 3.5$. At 0.1–1.0 Myr, the size distribution approximately follows the expected shape, with (i) a flat debris tail at $r \approx 1$ –100 μm ; (ii) a sharp rise at $r \approx 100$ μm to $r \approx 1$ –10 cm; and (iii) a steep fall for $r \gtrsim 1$ –10 cm. The small dip at $r \approx 100$ μm establishes particle sizes where removal of particles by merger with much larger particles dominates debris production by destructive collisions. The peak of the curves corresponds to particle sizes which contain most of the mass.

As the calculation proceeds, larger and larger particles contain more and more of the mass. It takes ~ 30 Myr for the peak in the relative size distribution to reach 10 m and another 270 Myr to reach 100 m. The growth of the largest particles follows this evolution, with 10 m particles in 1 Myr, 1 km particles in 3 Myr, and 10 km particles in 30 Myr. By 300 Myr, the largest particles have reached sizes of 200 km.

Throughout this evolution, the size distribution develops several distinctive features. At small sizes ($r \approx 10$ –100 μm to 1–10 cm), the debris tail contains more particles and evolves towards a single power-law. Among larger particles with $r \approx 1$ –100 km, there is a steeper power-law composed of large objects which grow by accreting much smaller objects (see also Kenyon 2002; Goldreich et al. 2004; Kenyon & Bromley 2008, 2010, 2012; Schlichting & Sari 2011).

Once the largest particles have sizes exceeding 500–1000 km, the size distribution

changes dramatically (Fig. 8). From 300 Myr to 500 Myr, (i) the dip at sizes of 10 m shifts to smaller and smaller particles and becomes progressively deeper; (ii) the peak at sizes of 100 m shifts to larger and larger sizes; and (iii) the fraction of mass in the debris tail grows significantly. These changes herald a short (second) runaway growth phase, where the largest particles with $r \approx 100$ km to 1000 km begin to contain most of the mass and achieve a size distribution with a standard slope $q_l \approx 3$ (see also Kenyon & Bromley 2012). By ~ 1.5 Gyr, collisions have removed most of the mass in small particles, effectively ending growth of the largest particles.

To understand the interesting evolution of the size distribution, it is helpful to consider the behavior of the velocity distribution. To simplify this discussion, we calculate the eccentricity e_k of each mass bin relative to the Hill eccentricity $e_h = (m_{max}/3M_\odot)^{1/3}$,

$$e_{k,rel} = e_k/e_h , \quad (9)$$

where m_{max} is the mass of the largest object in the annulus.

During the first period of runaway growth and oligarchic growth, the relative eccentricity distribution follows a standard pattern (Fig. 9; see also Wetherill & Stewart 1993; Kenyon & Luu 1999; Ohtsuki et al. 2002; Kenyon & Bromley 2002b; Goldreich et al. 2004; Kenyon & Bromley 2004a, 2008). When the largest objects reach sizes of 1 km, collisional damping and viscous stirring have established an equilibrium where the random velocities of small particles ($r \lesssim 0.1$ km) are \sim ten times the Hill velocity of the largest particles, a factor of 2–4 smaller than in our previous calculations where $r_{min} = 1$ m (e.g., Kenyon & Bromley 2008, 2010, 2012). At the largest sizes, dynamical friction reduces the eccentricities to a minimum $e_{k,rel} \approx 0.1$ –0.2. In between, dynamical friction maintains an approximate power-law, with $e_{k,rel} \propto r^{-n}$ and $n \approx 0.5$ –1. Despite the larger stirring as r_{max} reaches 30 km, a rough balance between collisional damping and viscous stirring preserves (i) the constant relative eccentricity, $e_{k,rel} = e_k/e_H \approx 10$, among the small particles and (ii) the power law decline among the larger particles.

As the evolution proceeds past 100 Myr, it is convenient to consider the behavior of large, intermediate, and small particles. For our adopted Q_D^* , large objects with $r \gtrsim 10$ km do not shatter; they gain mass and energy from collisions with smaller particles in the grid. Growing protoplanets also try to stir all other particles to larger and larger velocities. The magnitude of the stirring grows with the size of the protoplanet; the impact on smaller particles is fairly independent of the size of the small particles. Dynamical friction with small objects circularizes the orbits of the protoplanets.

Intermediate mass particles with $r \approx 10$ –100 m contain most of the mass but are easily shattered. Collisions among these objects place mass and energy into smaller mass bins. Compared to stirring by large particles, damping is relatively inefficient. Thus, intermediate mass bins lose mass and gain velocity with time.

Small objects with $r \lesssim 1$ cm contain little mass but do not shatter. These particles gain mass from the debris of collisions among intermediate mass particles and lose mass from collisions with large objects. Slow growth among these particles gradually shifts material to larger bins. As this material moves into the intermediate mass bins, destructive collisions cycle it back into smaller mass bins. With most of the mass in intermediate mass particles, the small particles gain mass with time.

The evolution of $e_{k,rel}$ for small particles depends on the relative importance of collisional damping and stirring by large particles. Without any gain in mass from destructive collisions, stirring by large particles dominates damping. However, destructive collisions rapidly cycle material from 10–100 m particles into smaller particles. Collisions among stronger small particles are not destructive. Thus, the net mass in small particles grows (Figs. 7–8). During this evolution, collisional damping gradually overcomes stirring by larger particles; $e_{k,rel}$ gradually declines.

Ultimately, the shape of the Q_D^* relation drives this evolution. In alternative calculations where $Q_D^* \propto r^{-\beta_b}$ and $\beta_b \leq 0$ at small radii, dramatic reductions in $e_{k,rel}$ among small particles cannot occur. When the largest particles reach 10–100 km sizes, the smallest particles in the grid shatter first. As large objects continue to grow, shattering impacts larger and larger particles, but the mass in the smallest particles always decreases. This evolution severely limits collisional damping and allows a collisional cascade to destroy all objects below some size limit.

With $\beta_b > 0$, intermediate mass particles always shatter first. For our adopted parameters, particles with $r \approx 30$ m have the smallest Q_D^* . As the random velocities of all particles slowly increase, debris from collisions of these weak planetesimals populates mass bins where particles are stronger and do not shatter. Collisional damping can then reduce $e_{k,rel}$ for objects in these mass bins.

The drop in $e_{k,rel}$ from collisional damping is responsible for a second runaway in the growth of the largest objects. With $e_{k,rel} \approx 0.5$ –2 at 300–500 Myr, gravitational focusing factors rise dramatically. As the largest protoplanets grow from 500 km to 2000 km, viscous stirring overcomes collisional damping for smaller and smaller objects. Thus, the ‘collisional damping front’ moves from roughly 10 m at 300 Myr to 10 cm at 500 Myr to 0.1 cm at 1.5 Gyr; the relative eccentricities for the larger objects rise from $e_{k,rel} \approx 5$ –6 at 500 Myr to $e_{k,rel} \approx 20$ at 1.5 Gyr to $e_{k,rel} \approx 30$ –40 at 10 Gyr.

In all simulations with $q = 3.5$ –4.0, the ultimate sizes of the largest objects depend on the timing of the dramatic reduction in $e_{k,rel}$ for the smallest objects. Usually, oligarchic growth produces large objects with $e_{k,rel} \gtrsim 3$ –10 before collisional damping is able to reduce the relative eccentricities for the smallest objects. Collisions between small objects and oligarchs then occur in the dispersion regime, where gravitational focusing factors are small and growth is slow. Despite damping, collisions among small objects are destructive. The

cascade then slowly removes the mass in small objects before oligarchs reach super-Earth sizes.

Sometimes, conditions conspire to enable the production of several super-Earth mass planets. When oligarchs and small objects have $e_{k,rel} \lesssim 1-3$, collisions are in the shear regime where gravitational focusing factors are large. Growth is then very rapid. For simulations with $q = 3.5-4.0$, the debris from every destructive collision is spread out over several orders of magnitude in radius. The large radius spread in the debris (i) limits the impact of dynamical friction on the oligarchs (enabling higher orbital eccentricities) and (ii) reduces the ability of collisional damping. Thus, super-Earth formation is very rare.

4.1.3. Collisional Damping when $q = 4.5-5.5$

When $q \gtrsim 4.5$, the second phase of runaway growth becomes more explosive (Figs. 3). At 300 Myr to 1 Gyr, the largest particles rapidly grow from $r_{max} = 2000-4000$ km to super-Earth sizes with $r_{max} \gtrsim 10^4$ km. Although super-Earth production is fairly insensitive to q for $q \gtrsim 4.5$, maximum planet sizes depend on b . Calculations with $b = 9/8$ almost always yield larger planets than calculations with $b = 1$.

Two factors enable routine super-Earth formation when $q \gtrsim 4.5$. In all calculations, the collisional cascade begins after the formation of large objects with $r_{max} \gtrsim 500-1000$ km. Debris production grows dramatically. Because radiation pressure ejects particles smaller than $1 \mu\text{m}$, the mass loss rate from the grid also grows. Although the debris production rate is insensitive to q , calculations with larger q concentrate the debris into a smaller range of radii and eject fewer particles with radii smaller than $1 \mu\text{m}$. At similar stages of evolution, more mass remains in the grid. Thus, the largest protoplanets tend to grow to larger masses.

Calculations with larger q also enhance the impact of collisional damping. When q is small (3.5–4.0), debris is spread out over a broad range of sizes. Collisional damping – which depends on the collision rate – then reduces the eccentricities of small particles more efficiently than those of larger particles (Fig. 10). With less mass in smaller objects than in larger objects, the growth of the largest protoplanets is fairly slow. When q is large (4.5–5.5), debris is concentrated in the largest particles. Collisional damping is then more effective for larger particles, which now contain much more mass than the smaller particles. Once relative eccentricities fall below the Hill velocity, protoplanets rapidly accrete the more massive particles and reach super-Earth sizes.

Fig. 11 compares the relative size distributions for calculations with various q . To illustrate the differences clearly, we focus on evolution times where the largest objects have $r_{max} = 2000-3000$ km and are just starting their second phase of runaway growth. When $q = 3.5$, the slope of the size distribution for small particles with $r \lesssim 1-10$ cm is shallow. Calculations with larger q have steeper size distributions with more mass in the largest objects.

Among larger particles with $r \gtrsim 10^4$ cm, the size distributions are nearly independent of q . At intermediate sizes ($10 \text{ cm} \lesssim r \lesssim 10\text{--}100 \text{ m}$), the concentration of mass in larger particles is striking.

Fig. 12 compares the relative eccentricity distributions for the same epochs as Fig. 11. At small sizes ($r \lesssim 1\text{--}10 \text{ cm}$), the changing impact of collisional damping with increasing q is apparent: damping is more effective at small sizes when $q = 3.5$ and at large sizes when $q = 4.5$ and 5.5 . With more debris in larger particles, the damping front – which marks the transition between particles with large e and small e – extends to larger r for calculations with larger q . For all particles with $r \gtrsim 1\text{--}10 \text{ cm}$, calculations with larger q have smaller relative eccentricities. When $q = 3.5$, the largest protoplanets have $e_{k,rel} > 1$; despite the small $e_{k,rel}$ for the smallest particles, these planets grow relatively slowly during the second runaway growth phase. When $q = 4.5\text{--}4.5$, the largest protoplanets have $e_{k,rel} < 1$; these planets can grow rapidly.

4.1.4. Evolution with Different Starting Conditions

To examine how the results of these simulations depend on initial conditions, we consider suites of simulations where the initial eccentricity and inclination are a factor of three larger or smaller than our nominal e_0 and i_0 . For each r_0 , we perform another 3–5 calculations with the different starting values of e and i . Within each suite of simulations, the median r_{max} is nearly identical; there is no obvious variation of r_{max} with e_0 . The range in r_{max} for these simulations is also similar, $\sim 20\%$ to 25% .

Within the full suite of simulations, there are modest differences in the time evolution of r_{max} and the size distribution as a function of starting e and i . In rings composed of small objects with $r_0 \lesssim 10\text{--}100 \text{ m}$, gravitational focusing is negligible at the start of the simulation. Thus, growth rates depend only on the geometric cross-section and the relative numbers of small and large objects. Although collisions produce more debris when the initial e and i are large, the debris contains a negligible amount of mass. Thus, the initial slow growth of small particles is independent of e_0 .

As the evolution proceeds, the rapid growth of the largest particles has two regimes. When the largest objects make the transition from slow growth to runaway growth, gravitational focusing factors increase dramatically. Ensembles of particles with smaller initial e reach this transition earlier than ensembles of particles with larger initial e . Defining t_R as the time of this transition, our results suggest $t_R(e_0/3) \approx 0.25t_R(3e_0)$.

When the largest objects make the transition from runaway to oligarchic growth, the growth rate again depends on the initial eccentricity. Throughout runaway growth, collisions in simulations with the largest e_0 produce the most debris. More debris leads to more effective collisional damping and somewhat more effective dynamical friction between the largest and

smallest objects. As a result, oligarchs grow faster in calculations with larger e_0 . Despite starting out more slowly, these oligarchs overtake the oligarchs in calculations with smaller e_0 . Thus, calculations with larger e_0 produce super-Earths somewhat more rapidly than calculations with smaller e_0 .

Among swarms of large particles with $r_0 \gtrsim 1$ km, the evolution seems to depend little on e_0 . Over typical growth times of 10–100 Myr for 1 km particles, collisional damping, dynamical friction, and viscous stirring produce similar size distributions for calculations with different e_0 . At the start of runaway growth, all calculations then appear to follow a similar sequence. Within this sequence, there is a large dispersion of outcomes due to stochastic variations in the collision rate. This dispersion dominates small differences in outcomes due to the starting conditions.

Fig. 13 illustrates some of these points for calculations with $b = 1$ and $q = 4.5$. When $r_0 = 10$ cm, particles with smaller initial e grow somewhat faster. Once r_{max} exceeds 10 km, oligarchs in calculations with larger e grow faster and eventually overtake oligarchs with smaller initial e . At late times, the largest objects enter a second runaway growth phase, where they accrete material rapidly at rates independent of e_0 . Eventually, the largest objects reach similar (super-Earth) sizes. When $r_0 = 1$ km, growth is more stochastic. Sometimes, small e calculations lag those with larger e (as in the Figure). In other simulations, large e calculations lag. All eventually produce 1–2 protoplanets with large radii.

4.2. Results at 250 AU

At 250 AU, the evolution from small planetesimals into super-Earth mass planets follows the behavior described for calculations at 125 AU. To avoid repeating the discussion of §4.1, we summarize differences between the two sets of simulations in the rest of this section.

The time scale for planet formation is the simplest difference between sets of calculations at 125 AU and at 250 AU. At any semimajor axis, the time scale for planets to reach identical sizes scales inversely with the initial mass in planetesimals and linearly with the orbital period. With identical initial planetesimal masses in our two sets of calculations, the formation time scales with orbital period. Thus, planets at 250 AU take roughly 3 times longer to form than those at 125 AU. For calculations with $r_0 = 1$ cm, this difference is not a major issue: 1 Gyr formation times at 125 AU become 3 Gyr time scales at 250 AU. Both time scales are shorter than the age of the Solar System. For calculations with $r_0 \approx 10$ –100 m, this difference is crucial: 2–3 Gyr formation time scales at 125 AU become 6–10 Gyr time scales at 250 AU. Thus, large particles at 250 AU do not form super-Earth mass planets over the age of the Solar System.

Fig. 14 illustrates this point for the growth of 1 cm and 10 m particles. When $r_0 = 1$ –10 cm, growth follows the same stages outlined in §4.1. After 1–10 Myr of slow growth,

periods of runaway growth, oligarchic growth, and runaway growth produce super-Earth mass planets in 2–4 Gyr. The growth time is roughly 3 times longer than the time scale at 125 AU (see Figs. 1–2). When $r_0 \gtrsim 10$ m, every phase of growth takes longer. Thus, the first runaway growth phase begins at 100 Myr to 1 Gyr, instead of 1–10 Myr. Although collisional damping still promotes rapid growth during the second runaway growth phase, rapid growth begins at 5–10 Gyr – too late to allow super-Earth formation within the age of the Solar System.

Although growth at 250 AU takes longer, small particles reach super-Earth sizes independently of q (Fig. 14). For $r_0 = 1$ –10 cm and all q , collisional damping drives the second period of runaway growth, where 2000–3000 km protoplanets rapidly grow into super-Earths. The time scale to produce super-Earths is also insensitive to q , 2–4 Gyr. Although super-Earths form for all q , calculations with $q = 4.5$ –5.5 typically yield planets roughly twice as massive as calculations with $q = 3.5$ –4.0.

At larger sizes ($r_0 \gtrsim 1$ –10 m), final planet masses depend on q . Calculations with $q = 3.5$ –4.5 stall at typical sizes of 4000–5000 km; simulations with $q = 4.5$ –5.5 reach radii of 7000–8000 km at 10 Gyr. On longer time scales, calculations with large q eventually reach super-Earth masses. Models with smaller q never produce massive planets.

Results at 250 AU seem fairly insensitive to b . For $r_0 = 1$ –10 cm, all calculations yield super-Earths. The largest planets have masses of 2–3 M_\oplus for $b = 1$ and $b = 9/8$. For $r_0 \gtrsim 10$ m, planets also have maximum sizes that do not depend on b . When $r_0 = 1$ m, calculations with $b = 9/8$ and $q = 4.5$ –5.5 routinely yield super-Earth mass planets on time scales of 2–4 Gyr. Simulations with $b = 9/8$ (1) and $q = 3.5$ –4.0 (3.5–5.5) cannot produce super-Earths in 10 Gyr.

Figs. 15–16 summarize r_{max} for the complete suite of calculations at 250 AU. When $b = 1$, nearly all calculations with $r_0 = 1$ –10 cm yields a super-Earth mass planet. Although roughly half of simulations with $r_0 = 1$ m yield a super-Earth, many produce smaller planets with $r_0 = 3000$ –7000 km. These results are fairly insensitive to q . With $r_0 = 10$ m, only a few calculations yield super-Earths. Ensembles of larger planetesimals never produce super-Earths. When $b = 9/8$ and $r_0 = 1$ cm to 1 m, super-Earth formation is also common. Larger planetesimals almost never produce a super-Earth. These results are also fairly independent of q .

4.3. Limitations of the Models

In previous papers, we have summarized various limitations in coagulation calculations for planet formation (e.g., Kenyon & Luu 1999; Kenyon & Bromley 2004a, 2008). Here, we focus on how choices in methods and initial conditions impact our results.

4.3.1. Resolution

Finite resolution – in the mass spacing parameter δ and the width of the annulus δa – is characteristic of all numerical coagulation calculations. As noted in the Appendix, simulations with finite δ lag the results of a calculation with ‘perfect’ mass resolution (see also Wetherill 1990; Kenyon & Luu 1998). For $\delta = 1.2$, this lag is negligible relative to simulations with $\delta = 1.05$ – 1.10 (Appendix). Thus, uncertainties due to finite δ are small.

Adopting a single annulus for our calculations limits our ability to follow the evolution of a planetesimal swarm as a function of semimajor axis (e.g., Spaute et al. 1991; Weidenschilling et al. 1997; Kenyon & Bromley 2004a, 2008). Despite this disadvantage, single annulus calculations yield fairly accurate estimates for the growth times and outcomes of coagulation calculations. For the initial conditions adopted here, the formation time depends only on the orbital period. Across the width of our single annulus, $\delta a/a = 0.2$, the orbital period changes by 35%. If the surface density is constant across the annulus, planetesimals at the inner edge of the annulus grow 35% faster than planetesimals at the outer edge of the grid. With typical formation times of ~ 1 Gyr and a factor of two range in the formation time, uncertainties due to the size of the annulus are small. Thus, our results yield good first estimates for the growth of super-Earths at 125–250 AU.

Although we allow any maximum size in the coagulation grid, setting a finite lower limit on particle size r_{min} changes the evolution of larger particles. During slow and runaway growth, particles with $r \sim r_{min}$ have negligible mass and little impact on the evolution of larger particles. Once the collisional cascade begins, debris rapidly fills the smallest mass bins. Particles with sizes $r \sim 10$ – $100 r_{min}$ are swept up by much larger protoplanets and destroyed by particles with somewhat smaller sizes $r \sim 1$ – $10 r_{min}$. With no particles smaller than r_{min} in the grid, our calculations have fewer destructive collisions among particles with $r \lesssim r_{min}$ compared to a calculation with an infinitesimally small r_{min} . Thus, our calculations produce an ‘excess’ of small particles relative to an ‘ideal’ calculation (see also Campo Bagatin et al. 1994; O’Brien & Greenberg 2003; Krivov et al. 2006, 2008, and references therein).

The standard method to address this issue is to extend the size distribution below r_{min} , assume these particles have relative velocities similar to particles with $r \approx r_{min}$, derive collision rates and outcomes with particles in the grid, and correct the excess number of particles with $r \approx r_{min}$ (e.g., Campo Bagatin et al. 1994; O’Brien & Greenberg 2003). Although this approach is attractive when $r_{min} \approx 1$ – 100 cm, it is problematic when $r_{min} \approx 1$ μ m. For solar-type stars, radiation pressure likely places smaller particles on highly eccentric or hyperbolic orbits as long as the ensemble of solids is optically thin (e.g., Burns et al. 1979). Relative collision velocities are then much larger, but collision rates are much smaller.

We plan to perform a set of multiannulus calculations to quantify outcomes with realistic

orbital geometry for small particles. To provide an initial estimate of the importance of the small size cut-off, we perform several calculations with $r_{min} = 0.1 \mu\text{m}$. Aside from shifting the excess of small particles to smaller sizes, this change has a modest impact on the overall size distribution or the growth of small objects. Thus, this uncertainty is minimal.

4.3.2. Fragmentation

The fragmentation algorithm is another uncertainty. We use a standard energy scaling approach which mimics the results of more detailed SPH and n -body calculations of binary collisions. Although our fragmentation parameters – Q_b , Q_g , β_b , and β_g – are consistent with the detailed calculations, other choices are possible (e.g., Morbidelli et al. 2009; Bottke et al. 2010; Kenyon & Bromley 2010; Kobayashi & Löhne 2014). Based on published results, it is straightforward to assess how alternative choices impact our results. For simplicity, we separate the discussion into the gravity regime for large objects ($r \gtrsim 0.1 \text{ km}$) and the strength regime for small objects ($r \lesssim 0.1 \text{ km}$).

In the gravity regime, there is general agreement among n -body and SPH calculations for β_g (Benz & Asphaug 1999; Leinhardt & Stewart 2012). Small variations about the adopted value have little impact on collision outcomes. Current simulations suggest at least a factor of 2–3 uncertainty in Q_g (Morbidelli et al. 2009; Bottke et al. 2010). Although the ultimate sizes of protoplanets grow with increasing Q_g (e.g., Kenyon & Bromley 2010), efficient collisional damping probably limits the importance of this parameter on our conclusions. Reducing Q_g by a factor of 100 or more probably prevents the formation of 1000 km or larger protoplanets. More modest changes, however, probably have little impact on our results.

In the strength regime, different choices for Q_b and β_b do not affect runaway and oligarchic growth (Kenyon & Bromley 2010). Making small particles harder to break (by increasing Q_b and decreasing β_b) increases the population of small objects and the effectiveness of collisional damping, enabling a broader set of initial conditions to produce super-Earths.

For smaller particles, likely outcomes depend on the relative importance of shattering and collisional damping. As an example, we consider the impact of reducing Q_D^* by a factor of ten for particles with $r \lesssim 100 \text{ m}$ in the strength regime. In our nominal calculations, collisions with impact velocities $v \gtrsim 400 \text{ cm s}^{-1}$ shatter 30 m particles. As the largest particles grow past 100 km, collisional damping maintains collision velocities for these particles just above this limit (Fig. 9). Although these particles shatter, particles much smaller than 10 m and much larger than 100 m do not shatter, which allows collisional damping to initiate the second phase of runaway growth. When Q_D^* is a factor of ten smaller, impact velocities $v \gtrsim 125 \text{ cm s}^{-1}$ shatter small particles, distributing debris into smaller mass bins. If the collisional damping rate remains identical to that in our nominal calculations, continued shattering removes the debris rapidly. Collisions of much more massive particles cannot

produce debris fast enough to replenish material lost from smaller mass bins. The collisional cascade then stalls the growth of the largest objects, which never reach super-Earth masses.

However, increased debris production associated with a smaller Q_D^* also increases the effectiveness of collisional damping. A simple estimate suggests that damping counters the impact of a larger rate of shattering. When Q_D^* is a factor of ten smaller, debris production for fixed Q_c is a factor of ten larger (eq. 6). With a factor of ten more mass in small particles, the damping rate is a factor of ten larger. Setting the approximate rates for viscous stirring and dynamical friction from large particles to this damping rate (e.g., Goldreich et al. 2004), the likely equilibrium velocity of small particles, 75–100 cm s⁻¹, is smaller than the 125 cm s⁻¹ shattering velocity. Thus, collisional damping appears capable of countering any large reduction in Q_D^* and maintaining the evolution on the path to super-Earth formation.

As noted in §4.1.2, setting $\beta_g \leq 0$ limits the impact of collisional damping on the velocity evolution of small particles. When $\beta_g \leq 0$, the smallest particles in the grid shatter first. Debris from these collisions permanently leaves the grid. As successively larger particles begin to shatter, smaller particles continue to shatter. More debris leaves the grid. With too little mass among smaller particles, collisional damping is ineffective. Velocities for small particles remain large, preventing a second runaway growth phase leading to the formation of super-Earth mass planets. Maximum protoplanet radii are then small, ~ 2000 km. Repeating our calculations with different parameters for Q_D^* is necessary to confirm this conclusion.

Aside from choosing q and the four parameters in the Q_D^* relation, we also set the mass of the largest fragment in the debris, $m_L = 0.2m_{esc}$, where m_{esc} is the total mass of the debris (see also Wetherill & Stewart 1993; Kenyon & Luu 1999). This approach differs from Morbidelli et al. (2009), $m_L \approx 0.004e^{(Q_c/4Q_D^*)^2} m_{esc}$; Kobayashi & Tanaka (2010), $m_L \approx \epsilon(Q_c/Q_D^*)^{-1} m_{esc}$ and $\epsilon \approx 0.01-0.5$; and Weidenschilling (2010), $m_L = 0.5(Q_c/Q_D^*)^{-0.78} m_{esc}$. For moderate collision energies ($Q_c \approx Q_D^*$), our algorithm places a somewhat smaller fraction (Weidenschilling 2010), a similar fraction for $\epsilon = 0.2$ (Kobayashi & Tanaka 2010), or a much larger fraction (Morbidelli et al. 2009) of the ejected mass in the largest particle within the debris. At low collision energies ($Q_c \ll Q_D^*$), Kobayashi & Tanaka (2010) and Weidenschilling (2010) have more massive fragments; Morbidelli et al. (2009) has less massive fragments. At high collision energies ($Q_c \gg Q_D^*$), all other algorithms place more material in smaller fragments.

Although accurately assessing the impact of these choices requires a broad set of additional simulations, we can outline the probable role of m_L in our calculations at 125–250 AU. The Morbidelli et al. (2009) algorithm always places more mass in less massive particles within the debris. Per collision, this approach thus assigns more mass to particles with $r < r_{min}$, leading to less mass among debris with $r > r_{min}$. Fewer debris particles results in less efficient collisional damping and limited growth during any second phase of runaway growth. Super-Earth formation seems unlikely.

In the Kobayashi & Tanaka (2010) and Weidenschilling (2010) approaches, super-Earth formation probably follows a similar path as in our calculations. At the start of the second runaway growth phase, most of the mass is in particles with $r \gtrsim 1$ km and $Q_c \approx Q_D^*$. For identical q , these algorithms place the debris in similar mass bins. Among small objects ($r \lesssim 1$ cm) with $Q_c \lesssim Q_D^*$, our algorithm removes mass from the grid more rapidly than these two approaches and thus underestimates the growth rate for super-Earths. At intermediate sizes (10 cm to 0.1 km), our approach places mass in larger fragments, removing mass less rapidly and thus overestimating the growth rate for super-Earths. For collisions among particles with these sizes, however, producing smaller fragments probably enhances collisional damping. If this enhanced collisional damping is sufficient to retain these small particles before low velocity destructive collisions remove them, super-Earth formation is likely.

To summarize, fragmentation is a critical issue in the growth of super-Earths at 125–250 AU. For reasonable choices of parameters in Q_D^* , likely outcomes are similar to the results discussed in §4.1–4.2. Plausible choices for m_L have a broader range of consequences. In our assessment, the Morbidelli et al. (2009) algorithm probably prevents super-Earth formation; other algorithms (e.g., Kobayashi & Tanaka 2010; Weidenschilling 2010) probably allow super-Earth formation. Verifying these conclusions require additional simulations which are beyond the scope of the present effort.

4.3.3. *Initial Conditions*

Aside from the initial radius for planetesimals r_0 , our choices for the initial conditions have little impact on our results. Our adopted set of r_0 spans a broad range of plausible sizes. Calculations with smaller r_0 will behave almost identically to simulations with $r_0 = 1$ cm. Because collision times scale with initial radius, outcomes for swarms of planetesimals with $r_0 > 1000$ km will follow those for $r_0 = 1000$ km but on longer time scales. Thus, calculations with much smaller (larger) r_0 yield (do not yield) super-Earth mass planets.

Another initial condition – the size distribution of planetesimals – is probably also not important. When planetesimals initially have a broad range of sizes, dynamical friction starts to modify the velocity distribution at the start of the calculation. Growth of large particles ($r_0 = 1$ –100 km) then usually proceeds as much as a factor of two faster than growth from a mono-disperse set of particles (Kenyon & Bromley 2010, 2012). We expect similar differences at 125–250 AU. Thus, starting with a broad range of sizes might enable some initial conditions to yield super-Earths on 2–3 Gyr time scales instead of 4–6 Gyr time scales.

A broad range of sizes probably has much less impact on the outcomes of calculations with small particles. When r_0 is small, dynamical friction and gravitational focusing are less important. Independent of the initial conditions, short collision times and slow growth

rapidly produce a broad range of sizes. Thus, our conclusions for the growth of small particles into super-Earths are fairly independent of the initial range of sizes.

Our results indicate that the starting eccentricity also has little impact on the outcomes of the calculations. For simulations with $r_0 \gtrsim 1$ km, our choices for the initial eccentricity span the likely range of possibilities. At smaller sizes, the equilibrium e and i are much smaller than our adopted e_0 and i_0 . If interactions with the gas circularize the orbits of small particles effectively, the initial e and i might be much smaller. Gravitational instability of the swarm is then very likely (e.g., Michikoshi et al. 2007, 2009), leading to much more rapid growth of large particles.

4.3.4. Dynamics

The approximations used in coagulation codes begin to break down when (i) most of the mass is in a few planets and (ii) the dynamical interactions between these objects dominates collective interactions between small and large objects. To quantify these limits, we first consider dynamical constraints. At 125–250 AU, the escape velocity from the Solar System is roughly 2.5–4 km s⁻¹. With $\rho_s = 1.5$ g cm⁻³, planets have escape velocity

$$v_{esc} \approx 9 \left(\frac{R_p}{10^4 \text{ km}} \right) \text{ km s}^{-1} . \quad (10)$$

Gravitational interactions raise the relative velocities of massless particles to roughly 60% of the escape velocity. Thus, planets with $R_p \gtrsim 5000$ km can eject small particles from the solar system.

At the same time, collisional damping opposes gravitational scattering. Our calculations suggest damping overcomes scattering until planets reach super-Earth sizes. Thus, dynamical ejection of small particles is probably unimportant throughout most of each calculation.

When protoplanets are large enough, their dynamical interactions are stronger and more chaotic than suggested by our Fokker-Planck approximation. Using the isolation criterion of eq. (2), two (four) equal-mass oligarchs on roughly circular orbits are isolated from one another when they have $R_H \approx 0.028 a$ (0.014 a). These limits correspond to planets with masses of roughly 20 M_\oplus (3 M_\oplus). With typical masses of 2–3 M_\oplus , the two super-Earths produced in many of our calculations are clearly isolated. Large groups (10–20) of much lower mass planets are also stable. Although four super-Earths are nominally isolated, these planets are close to the dynamical stability limits and could be dynamically unstable (e.g., Kenyon & Bromley 2006; Bromley & Kenyon 2006, and references therein).

Deriving the number of massive protoplanets in each calculations allows us to quantify the importance of strong dynamical interactions between protoplanets. Among 200 (150) calculations at 125 AU (250 AU), 45% (0%) produce one super-Earth, 47% (78%) produce

two, 6% (12%) produce three, and 2% (10%) produce four. In most of these calculations – 98% at 125 AU and 90% at 250 AU – dynamical interactions among super-Earths are very unlikely. In others, dynamical interactions are probably common.

During the other 800 (450) calculations at 125 AU (250 AU) which do not yield a super-Earth, protoplanets almost never interact dynamically. Because calculating these interactions is very cpu intensive (e.g., Kenyon & Bromley 2006), our neglect of these interactions is reasonable. Once we consider multiannulus calculations of super-Earth formation at 125–250 AU, we will revisit this issue.

Although protoplanets eventually contain most of the mass remaining in each simulation, the approximations in our coagulation code rarely break down. Most simulations do not produce one or more super-Earths. In these situations, most of the mass is in protoplanets with sizes ranging from a few hundred km to a few thousand km. Our code accurately handles these situations. When 1–2 super-Earths form, these objects begin as 2000–3000 km objects which accrete material from the swarm of small particles with low eccentricity. Because these two objects do not interact dynamically, our statistical approach accurately derives the accretion rate of small particles.

In a few cases, 3–4 oligarchs accrete small particles and grow to super-Earth masses. Our approach handles the growth of these oligarchs accurately. Dynamical interactions among these protoplanets become important near the end of the accretion process, when their masses approach an Earth mass. At this point our approximations begin to break down. Usually, we promote these objects into an n -body code and follow their dynamical interactions precisely (e.g., Kenyon & Bromley 2006; Bromley & Kenyon 2006, 2011a). Here, we simply note the formation of 3–4 objects with near super-Earth masses and save the more cpu intensive calculation for another study.

5. DISCUSSION

Our analysis indicates a plausible path for *in situ* production of super-Earth mass planets at 125–250 AU around solar-type stars. This path begins with a massive ring, $M_0 \gtrsim 15 M_\oplus$, composed of small particles, $r_0 \approx 1$ cm to 10 m. Successive mergers of these objects lead to larger and larger protoplanets. On a time scale of ~ 1 Gyr, coagulation yields several planets with masses $m \approx 1\text{--}4 M_\oplus$.

Although we did not consider a range of initial masses for rings at 125–250 AU, previous studies demonstrate how the growth times and final masses of protoplanets depend on the initial mass and semimajor axis of a swarm of solid objects (e.g., Kenyon & Bromley 2008, 2010). For all initial disk masses, the time scale for protoplanets to reach a fiducial radius (e.g., 1000 km) depends inversely on the initial disk mass. When $M_0 \approx 15 M_\oplus$ at 125 AU, it takes protoplanets 400 Myr to 1 Gyr to reach radii of 1000 km. Doubling (halving) the

initial disk mass halves (doubles) these time scales to 200–500 Myr (0.8–2 Gyr). Although the total masses of the most massive protoplanets also scale roughly linearly with mass, gravitational interactions among the protoplanets set the ultimate masses of the most massive protoplanets. For the conditions we consider, halving the initial disk mass reduces this ultimate mass by roughly 50%; however, doubling the initial mass may simply double the number of super-Earths rather than double the masses of the most massive super-Earths. Finally, the time scale for planet formation depends linearly on the orbital period. Doubling the initial semimajor axis nearly triples the formation times.

Our conclusions raise several interesting issues concerning planet formation theory. Super-Earth formation at 100–250 AU also has direct observational consequences for the structure of debris disks around solar-type stars and for the architecture of the outer Solar System. After a brief discussion of several theoretical points, we describe how the new calculations impact our understanding of debris disks and the outer Solar System. We conclude this section with several observational tests which can help to constrain plausible models.

5.1. Theoretical Issues: Initial Conditions

Our model for *in situ* super-Earth formation at 125–250 AU requires a massive reservoir of solids in the outer regions of the protosolar nebula. Observations of nearby star-forming regions suggest these initial conditions are plausible. In the ρ Oph and Taurus-Auriga molecular clouds, disks with radii of 100–300 AU are fairly common around pre-main sequence stars with ages of roughly 1 Myr (e.g., Andrews & Williams 2005; Andrews et al. 2009, 2010; Williams & Cieza 2011, and references therein). Of the twelve ρ Oph disks with outer radii larger than 100 AU, five have measured surface densities at least as large as the 0.02 g cm^{-2} (125 AU) or the 0.005 g cm^{-2} (250 AU) required by our simulations. Within most disks around young stars, observations require particles at least as large as 1–10 mm (e.g., Williams & Cieza 2011). In many cases, observations also reveal that these particles have scale heights much smaller than the local scale height of the gas (e.g., Furlan et al. 2006, 2009). Thus, current evidence implies that these disks have particle sizes and total masses similar to those required by our calculations.

Once cm-sized ‘pebbles’ form and settle towards the disk midplane, various processes shape their evolution. Collisions can slowly merge pebbles into larger objects or shatter them into fine dust grains (e.g., Birnstiel et al. 2010, 2012; Windmark et al. 2012; Garaud et al. 2013). At 125–250 AU, viscous evolution slowly drives the gas (and any solids coupled to the gas) to larger distances (e.g., Lynden-Bell & Pringle 1974; Stepinski 1998; Chambers 2009). Large solids feel a headwind from the gas, which drags them towards (and perhaps into) the Sun (e.g., Adachi et al. 1976; Weidenschilling 1977; Rafikov 2004). However, the gas can also concentrate pebbles into much larger solid objects (e.g., Youdin & Goodman 2005; Johansen et al. 2007). Nearly all published studies of these phenomena focus on outcomes inside

30 AU, where planet formation is a common process. Scaling these results to conditions at 125–250 AU, it appears that 1 cm and larger particles can survive for the 1–3 Myr lifetime of the gaseous disk. Detailed studies of grain evolution are necessary to consider whether this conclusion is robust. If it is, our calculations suggest super-Earth formation is a likely outcome in large protostellar disks.

Observations of solid objects beyond 30 AU might constrain the outer radius of the gaseous component of the protosolar nebula. Kretke et al. (2012) show that the gaseous disk excites Kozai oscillations in planetesimal leftovers from the formation of gas giant planets at 5–20 AU. Some of these planetesimals end up on orbits with low eccentricity and high inclination. The current lack of these objects suggests an outer edge of ~ 80 AU for the protosolar nebula. Observations over the next decade should allow significant refinement in this estimate.

5.2. Theoretical Issues: Fragmentation

The calculations in §4 illustrate the complex interplay between collisional damping, fragmentation, and the growth of the largest protoplanets in a gas-free environment. When protoplanets reach sizes of 500–1000 km, they initiate a collisional cascade which gradually grinds km-sized and smaller objects into micron-sized dust grains. Radiation pressure then ejects these grains from the planetary system. In our calculations, ejected grains comprise $\sim 25\%$ to 80% of the initial mass in the ring.

Throughout the collisional cascade, the largest protoplanets try to accrete smaller planetesimals and collision fragments. The rate these protoplanets grow depends on the magnitude and timing of collisional damping (see also Kenyon & Bromley 2002a, 2004a; Goldreich et al. 2004). When the largest protoplanets *and* small fragments have relative eccentricity, $e_{k,rel} < 1$ (see eq. 9), protoplanets rapidly accrete the fragments. Super-Earth formation is likely. When either of these conditions is *not* met, protoplanets cannot accrete fragments as rapidly as the cascade grinds the fragments to dust. Protoplanets grow slowly and almost never reach super-Earth masses.

In our calculations, the two conditions for super-Earth formation depend on the slope q of the power-law size distribution for collisional debris and the slope b in the relation for the mass of the debris produced in a collision ($m_{esc} \propto (Q_c/Q_D^*)^b$; see eq. 6). At 125 AU, calculations with $q \approx 4.5$ – 5.5 and $b \approx 9/8$ are much more likely to meet these constraints on $e_{k,rel}$ than calculations with $q \approx 3.5$ – 4.0 and $b \approx 1$. At 250 AU, super-Earth formation is fairly independent of q and weakly dependent on b .

Collisional damping is the physical mechanism that sets the final masses of protoplanets as a function of (q, b) . When q is large, more fragments are concentrated into a smaller range of fragment masses. These fragments collide more rapidly, enabling collisional damping

to reduce collision velocities more effectively. Smaller velocities initiate a second runaway growth phase where protoplanets reach super-Earth masses. When q is small, fragments are spread out among a much larger range of masses. Damping is less effective; protoplanets grow more slowly. The b parameter magnifies this behavior. When b is large (small), high velocity collisions produce more (fewer) fragments, enhancing (reducing) collisional damping and the second runaway growth phase.

Choosing the ‘best’ b and q for coagulation calculations is not straightforward. Despite recent advances in numerical simulations of debris production during binary collisions (e.g., Durda et al. 2004, 2007; Leinhardt & Stewart 2012; Benavidez et al. 2012), theory offers mixed guidance on several aspects of the algorithms used to model fragmentation. Currently, there is reasonable agreement on the binding energy Q_D^* in the gravity and strength regimes (see also Housen & Holsapple 1999, 2011). Modest changes consistent with the range of results from numerical simulations have modest impact on the growth of protoplanets (e.g., Kenyon & Bromley 2010, 2012).

There is also reasonable agreement on the magnitude of b . For a broad variety of approaches, $b = 1$ – 1.25 (e.g., Davis et al. 1985; Housen & Holsapple 1990; Benz & Asphaug 1999; Housen & Holsapple 1999; Kobayashi & Tanaka 2010; Leinhardt & Stewart 2012). For high velocity collisions between roughly equal mass objects, our approach is consistent with analytic derivations and numerical simulations. For cratering collisions where objects have very unequal masses, analytic fits to experimental data infer the ejected mass as a function of the impact velocity and the escape velocity of the more massive target (e.g., Housen & Holsapple 2011). When $b = 1$ or $9/8$, our algorithm for the ejected mass generally agrees with these detailed fits (e.g., Kenyon et al. 2014).

However, there is less agreement on $r_{max,d}$, the size of the largest fragment within the debris. For example, the recommended procedure of Leinhardt & Stewart (2012) results in two large fragments with total mass of roughly 10% of the total mass in the debris. From the results of the Durda et al. (2007) calculations, Morbidelli et al. (2009) derive a factor of 5–10 smaller mass than Leinhardt & Stewart (2012). Our approach – where we place 20% of the total debris mass into the largest fragment – is similar to Leinhardt & Stewart (2012) but very different from Morbidelli et al. (2009). In future calculations, we plan to see if these differences have a clear impact on the overall outcomes of coagulation calculations.

Moreover, there is little agreement on the size distribution for the debris. Leinhardt & Stewart (2012) propose a single power-law with $q = 3.85$ which extends from the largest remnant to the smallest particle allowed in the calculation. In contrast, Morbidelli et al. (2009) adopt $q \approx 9$ – 10 for the largest particles in the debris and $q = 3.5$ for the smallest particles. In both approaches, the largest particles contain most of the mass; thus, Morbidelli et al. (2009) have a much larger effective q than Leinhardt & Stewart (2012). Our calculations show that the magnitude of q has a dramatic impact on the size of the largest protoplanets. Using SPH/ n -body simulations of binary collisions to derive a better appreciation of the

behavior of q as a function of the collision velocity, mass ratio, and composition would enable a better understanding of the outcomes of planet formation simulations.

Finally, there has been little discussion of $r_{min,d}$ the minimum size of fragments produced during destructive collisions. Usually, $r_{min,d}$ is zero; sometimes $r_{min,d} \ll r_{max,d}$. Together with the binding energy of planetesimals and larger protoplanets, $r_{min,d}$, $r_{max,d}$, and q establish the importance of collisional damping and the likelihood of super-Earth formation in swarms of icy planetesimals. Robust predictions for the outcomes of planet formation calculations therefore require a broader discussion of these fragmentation parameters.

In an interesting approach to these issues, Krijt & Kama (2014) infer a minimum size for debris fragments $r_{min,d}$ using constraints on the *surface energy* of colliding particles. In their model, a fraction f of the impact kinetic energy makes new surface area. When $f = 0$, the surface energy of colliding particles is conserved. When $f > 0$, the collision produces additional surface area. For size distributions with $3 < q < 4$, they derive $r_{min,d}$ as a function of the bulk properties of the colliding planetesimals. In high velocity collisions with fixed q , their picture produces size distributions similar to our algorithm. At lower velocities, collisions produce only a few (sometimes one) particles rather than a broad size distribution.

Although the Krijt & Kama (2014) analytic model provides an interesting way to choose some aspects of the size distribution, it is valid only for $3 < q < 4$ and does not directly constrain f or q . Expanding on their methods might yield a more general analytic prescription for the size distribution of the debris and narrow the allowed range for q (see also Housen & Holsapple 1999).

Without a useful analytic model, numerical collision calculations with a larger dynamic range in the sizes of debris particles would provide useful guidance on collision outcomes and the properties of the debris. Larger simulations would place better limits on plausible values for $r_{min,d}$ and q in coagulation calculations.

5.3. Applications: Debris Disks

Aside from these theoretical issues, our results have clear consequences for the origin of the Solar System and debris disks at large distances from their host stars. Among known debris disks around solar-type stars, several have material at $a \approx 100$ – 200 AU. The disk in HD 107146 (G2 V spectral type, age ~ 100 Myr) extends from ~ 30 AU to ~ 150 AU (Corder et al. 2009; Ricci et al. 2014). Recent *ALMA* data indicate a reduction in dust surface density at 70–80 AU (Ricci et al. 2014). The large ring observed in HD 202628 (G2 V, 2 Gyr) lies at ~ 200 AU and has a structure similar to the ring in Fomalhaut (Krist et al. 2012). In HD 207129 (G2 V, 2–3 Gyr; Krist et al. 2010; Marshall et al. 2011), a ring with roughly similar geometry is somewhat smaller (~ 160 AU).

Published analyses suggest fairly large masses of solids in HD 107146 and HD 207129. For HD 107146, fits to the dust distribution from *ALMA* data indicate a mass of roughly $0.2 M_{\oplus}$ in cm-sized and smaller particles (Ricci et al. 2014). Deriving the total mass in solids requires an adopted size distribution. If $n(r) \propto r^{-q}$ for $r = 1$ cm to 100 km, likely values for q yield total masses ranging from $2\text{--}3 M_{\oplus}$ for $q \approx 4$ to $100 M_{\oplus}$ for $q \approx 3.5$ (see also Ricci et al. 2014).

In HD 207129, detailed analysis of *Herschel* images and the spectral energy distribution implies a total mass of $0.007 M_{\oplus}$ in mm and smaller particles (Löhne et al. 2012). Adopting a power-law size distribution for 1 mm to 100 km objects yields masses ranging from $0.1 M_{\oplus}$ ($q \approx 4$) to $70 M_{\oplus}$ ($q \approx 3.5$).

Together with our numerical simulations, the large solid masses derived for these systems show that super-Earth mass planets are reasonable outcomes of the planet formation process. The geometries of the rings in HD 202628 and HD 207129 are similar to the geometry adopted for our rings at 125 AU and at 250 AU. With ages of 1–3 Gyr, our models suggest several super-Earths might be growing within the dusty debris of each system.

In HD 107146, Ricci et al. (2014) infer a reduced surface density of dust at 70–80 AU within the extended disk of debris. If the lower surface density is a ‘gap’ in the disk produced by a planet, the likely mass of the planet is a few Earth masses. Based on our calculations, super-Earth formation at 70–80 AU around a 100 Myr old star requires a larger initial surface density than we considered for this study (see also Kenyon & Bromley 2008, 2010). With a factor of 3–5 increases in surface density, super-Earth formation in 100 Myr is a plausible outcome of our simulations (see also Ricci et al. 2014).

5.4. Applications: Solar System

The calculations in this study provide interesting constraints on the formation of a suspected planet X beyond 100 AU in the Solar System. Scaling the results at 125 AU and 250 AU, the time scale to grow Earth-mass or larger planets from 1–10 cm pebbles is

$$t_{SE} \approx 1 \left(\frac{M_0}{15 M_{\oplus}} \right)^{-1} \left(\frac{a}{125 \text{ AU}} \right)^{3/2} \text{ Gyr} , \quad (11)$$

where M_0 is the initial mass in an annulus of width $\delta a \approx 0.2a$ centered at semimajor axis a . Requiring planet formation to conclude within 3–4 Gyr allows super-Earths in annuli with $M_0 \approx 15 M_{\oplus}$ at $a \lesssim 300$ AU. More massive rings enable super-Earths outside 300 AU.

Together with Bromley & Kenyon (2014), this study outlines plausible alternatives to standard migration models for super-Earths located at large distances from their host stars. In the migration hypothesis, a planet forms close to the host star and migrates out through a disk of gas or small planetesimals (e.g., Crida et al. 2009). In the scattering picture, a gas

giant planet dynamically scatters a much smaller planet from 5–10 AU to 100–200 AU; the gaseous disk then circularizes the orbit of the smaller planet at large a (Bromley & Kenyon 2014). The *in situ* model envisions a massive swarm of solids in a ring at large a ; coagulation within the ring allows the solid to grow into one or more super-Earth mass planets.

In each of these scenarios, it is easier to understand a planet X in orbit at $a \approx 100$ –250 AU than at $a \gtrsim 1000$ AU. For the *in situ* picture, formation at $a \approx 1000$ AU requires a large reservoir of solids, $\gtrsim 300 M_{\oplus}$. Fewer than 1% of the protostellar disks around Taurus-Auriga pre-main sequence stars and only 10% to 15% of the disks around Taurus-Auriga embedded protostars contain this much mass (see the discussion in Najita & Kenyon 2014, and references therein). In contrast, 20% to 60% of the disks around young stars contain enough mass to produce a super-Earth at 100–200 AU. Thus, *in situ* formation well beyond 200–300 AU seems unlikely.

Observations of young stars similarly limit the migration and scattering scenarios. In both mechanisms, the planet ends up on a roughly circular orbit within the gaseous disk surrounding the newly-formed central star. With typical characteristic radii of 20–200 AU (e.g., Andrews et al. 2010), disks around young stars rarely extend to 500–1000 AU. Thus, formation at 5–10 AU followed by migration/scattering to 500–1000 AU is also very unlikely.

5.5. Tests

Testing theories for super-Earths beyond 100 AU requires additional observations. Although recent observations identify Jovian mass planets associated with several circumstellar disks (e.g., Lagrange et al. 2010; Currie et al. 2014), direct imaging observations of isolated super-Earths with $a \gtrsim 100$ AU around other stars is unlikely with current or planned facilities (e.g., Hugot et al. 2012; Jovanovic et al. 2013; Macintosh et al. 2014). However, detecting super-Earths with surrounding debris clouds might allow direct tests as in Fomalhaut b (e.g., Kalas et al. 2005; Chiang et al. 2009; Kennedy & Wyatt 2011; Currie et al. 2012; Galicher et al. 2013; Kalas et al. 2013; Kenyon et al. 2014). Unless planet X has a moderate albedo, direct detection within the Solar System is also very challenging (Trujillo & Sheppard 2014). Observations of debris disks and Sedna-like objects provide alternate ways to test the various theoretical possibilities.

Among debris disks, comparisons between observations and the debris predicted from collisional cascade or planet formation calculations allow indirect tests (e.g., Kenyon & Bromley 2002b, 2008, 2010; Löhne et al. 2012; Kobayashi & Löhne 2014). Although discrepancies between predictions and observations remain, these results generally confirm the cascade models (see also Gáspár et al. 2013). However, previous analyses did not include collisional damping of small particles within the cascade. In our calculations, damping enhances the population of $10^{-2} - 10^2$ cm particles and thus probably enhances the predicted emission

from small particles. As we learn more about the importance of damping as a function of the initial disk mass and semimajor axis, we will be able to compare the predicted emission with observations of complete ensembles of debris disks observed with *IRAS*, *Spitzer*, and *Herschel*.

For nearby debris disks, *ALMA* observations offer the best hope of placing better limits on super-Earths at large distances from the parent star. When super-Earths form within a ring of small solid particles, they should clear out a gap with a half-width of roughly 3 Hill radii (e.g., Ida et al. 2000; Kirsh et al. 2009; Bromley & Kenyon 2011b, 2013). If *ALMA* detects narrow regions of low dust surface density in other disks and rings (as in HD 107146), comparisons with the predicted surface density within a gap might yield constraints on super-Earth formation in debris disks (e.g., Ricci et al. 2014).

Within the Solar System, current evidence for a massive planet beyond 100 AU in the Solar System is limited and indirect. In the discovery paper for 2012 VP₁₁₃, Trujillo & Sheppard (2014) suggest the need for a planet at 200–250 AU to explain the clustering of ω among a dozen objects with perihelion distance $q_p \gtrsim 30$ AU and orbital eccentricity $e \gtrsim 0.7$. In addition to confirming the clustering, de la Fuente Marcos & de la Fuente Marcos (2014) note other clusterings in the orbital parameters. They propose two super-Earth mass planets at roughly 200 AU and 250 AU. However, constraints on the precession of the inner planets appear to constrain any planet X to much larger $a \gtrsim 1000$ AU (e.g., Iorio 2009, 2012, 2014, and references therein). Future studies need to reconcile the distribution of orbital parameters for Sedna-like objects with the precession rates for the gas giants and terrestrial planets.

New calculations can place better constraints on the formation of planet X and lower mass objects like Sedna and 2012 VP₁₁₃. For the *in situ* picture, ensembles of Earth-mass planets formed at 200 AU will eventually overcome collisional damping and scatter smaller objects (and possibly themselves) throughout the Solar System. Comparing the orbital elements of known objects on Sedna-like orbits with orbits derived from detailed numerical simulations of planet formation will allow good tests of this formation model (see also Kretke et al. 2012; Bromley & Kenyon 2014).

Larger samples of Sedna-like objects can also test formation mechanisms. For 100–1000 km particles, coagulation calculations produce a size distribution with power-law slope $q \approx 4$ (e.g., Kenyon & Bromley 2004d; Schlichting & Sari 2011; Kenyon & Bromley 2012; Schlichting et al. 2013). Among smaller objects, the slope has a broader range and depends on a variety of parameters. If 100–1000 km objects on Sedna-like orbits are as common as current surveys suggest (e.g., Trujillo & Sheppard 2014), measuring the slope of the size distribution could constrain the formation mechanism.

6. SUMMARY

We analyze aspects of three mechanisms – migration, scattering, and *in situ* formation – for placing indigenous super-Earth mass planets on orbits with large semimajor axes, $a \gtrsim 100$ AU, around a solar-type star. In migration and scattering models, a super-Earth forms within a few Myr at $a \approx 5$ –10 AU. Interactions with other protoplanets and a massive disk then stabilize the orbit at large a . The *in situ* picture requires a massive reservoir of solid material where super-Earths form directly. For all three hypotheses, super-Earths at 100–300 AU are much more likely than super-Earths beyond 300 AU.

Using a suite of single-annulus coagulation calculations, we investigate the physical requirements to form super-Earth mass planets at 125–250 AU around solar-type stars. In annuli with $M_0 \approx 15 M_\oplus$, super-Earth formation is common. When this mass is in planetesimals with $r_0 \approx 1$ cm to 1 m, super-Earths form in 1–3 Gyr at 125 AU and in 2–5 Gyr at 250 AU. Although swarms of larger planetesimals ($r_0 \approx 10$ m to 10 km) can produce super-Earths in $\lesssim 4$ Gyr at 125 AU, growth at 250 AU takes longer than the age of the Solar System. Thus, *in situ* growth of super-Earths at 200–300 AU requires a massive ring of small planetesimals.

Collisional damping of the debris from destructive collisions is an essential ingredient in super-Earth formation at 125–250 AU. During the first 300 Myr to 1 Gyr of evolution, the usual pattern of slow growth, runaway growth, and oligarchic growth leads to the formation of 1000–3000 km protoplanets and a swarm of leftover small (0.1–10 km) planetesimals with large relative velocities (see also Kenyon 2002; Kenyon & Bromley 2002b, 2004a, 2008, 2010). Destructive collisions among these leftovers generates a multitude of mm-sized to m-sized fragments. Damping reduces the relative velocities of the fragments by 1–2 orders of magnitude, to $e_{k,rel} \lesssim 1$ where $e_{k,rel} = e/r_H$ and $r_H = (m_{max}/3M_\odot)^{1/3}$ is the relative size of the Hill sphere of the most massive protoplanet. *The small fragment velocities enable a second runaway growth phase, where protoplanets grow rapidly. When protoplanets have $e_{k,rel} \lesssim 1$, they reach super-Earth sizes in 1–2 Gyr.*

Fragmentation also plays a crucial role in the formation of super-Earths at 125–250 AU. In our calculations, the debris from destructive collisions has a power-law size distribution, $n(r) \propto r^{-q}$. At 125 AU, setting $q = 4.5$ –5.5 promotes the formation of super-Earths. When $q = 3.5$ –4.0, super-Earth formation is very rare. At 250 AU, all $q \approx 3.5$ –5.5 allow super-Earth formation. In models with $q \approx 4.5$ –5.5, however, super-Earths tend to be more massive than in calculations with $q \approx 3.5$ –4.0. Within the fragmentation algorithm, the variation of ejected mass with impact energy is also important. In our approach, $m_{esc} \propto (Q_c/Q_D^*)^b$. Calculations with $b = 9/8$ tend to produce more massive protoplanets than calculations with $b = 1$.

Improving the calculations requires a better understanding of several parameters in the fragmentation algorithm. In our approach, the mass of the debris ejected during a collision

is $m_{esc} = 0.5(Q_c/Q_D^*)^b$, where Q_c is the collision energy, Q_D^* is the collision energy required to eject half of the mass involved in the collision, and $b = 1.00$ – 1.25 . For the mass of the debris, we set $m_L = 0.2 m_{esc}$ and adopt a constant value q for slope of the power-law size distribution of the debris. In a future study, we plan to investigate the impact of adopting a functional form for the largest object in the debris, $m_L = m_{L,0}(Q_c/Q_D^*)^{-b_L}$ where $b_L \approx 0.5$ – 1.0 (e.g., Kobayashi et al. 2010; Weidenschilling 2010). However, analytic studies and more comprehensive numerical simulations of binary collisions would enable more informed choices for $m_{L,0}$, b , b_L , and q as a function of the collision energy and the bulk properties of the planetesimals.

Observations of debris disks allow interesting tests of the models. Expanding our single-annulus models to a full multi-annulus calculation will enable comparisons between predictions and observations of the time-dependent debris disk luminosities. *ALMA* observations of the dust surface density in the gaps of debris disks can place limits on super-Earth formation rates.

Discovery of planet X and additional dwarf planets on Sedna-like orbits would also test the plausibility of *in situ* super-Earth formation at 125–250 AU. From the mass distribution of protostellar disks, indigenous super-Earths with $a \gtrsim 500$ AU are unlikely (see also Najita & Kenyon 2014). Robust estimates of the semimajor axis of any planet X directly constrain planet formation theory. Aside from placing better constraints on an orbit for planet X (Trujillo & Sheppard 2014; de la Fuente Marcos & de la Fuente Marcos 2014), orbital elements and (eventually) the size distribution for new members of the inner Oort cloud can test the predictions of the coagulation models.

We acknowledge generous allotments of computer time on the NASA ‘discover’ cluster. We thank the referee, K. Ohtsuki, for a constructive and thorough review. Advice and comments from T. Currie and M. Geller also greatly improved our presentation. Portions of this project were supported by the *NASA Astrophysics Theory and Origins of Solar Systems* programs through grant NNX10AF35G and the *NASA Outer Planets Program* through grant NNX11AM37G.

A. Appendix

Orchestra contains many algorithms to follow the formation and evolution of a planetary system. With few analytic solutions available, verifying these algorithms requires comparisons with other approaches. In previous papers (e.g., Kenyon & Luu 1998; Kenyon & Bromley 2001; Bromley & Kenyon 2006; Kenyon & Bromley 2008; Bromley & Kenyon 2011a), we compare our numerical results with analytic solutions and n -body simulations.

Here, we describe several additional tests.

A.1. Runaway and Oligarchic Growth

Accurate calculations for runaway and oligarchic growth depend on the spacing factor $\delta = m_{k+1}/m_k$ between adjacent mass bins (e.g., Ohtsuki & Nakagawa 1988; Ohtsuki et al. 1990; Wetherill & Stewart 1989; Wetherill 1990). When bins have fixed masses, adopting large δ risks severe underestimates in the growth times for massive objects. Ohtsuki et al. (1990) derive the constraints on δ which allow accurate solutions (see also Fraser 2009). In our approach, mass bins have fixed boundaries but variable masses (see also Wetherill & Stewart 1993; Kenyon & Luu 1998). Calculations with $\delta > 1$ always lag a ‘perfect’ solution, reaching a fiducial size later in time. Larger δ ’s always produce larger lags.

To understand the origin of the lag, we consider a simplified example. With preset boundaries $m_{k+1/2}$, the average mass of objects in a bin is \bar{m}_k , where $m_{k+1/2} < \bar{m}_{k+1} < m_{k+3/2}$ and $m_{k+3/2} = \delta \cdot m_{k+1/2}$. When an object in bin $k + n$ merges with an object in bin k , the mass of the new object is $m_c = \bar{m}_k + \bar{m}_{k+n}$. In an ideal calculation with an infinite number of mass bins, the mass of the new object is placed in a new bin which is distinct from all other bins. In a real calculation, however, placing this object in a new bin with index $k_c > k + n$ requires $m_c > m_{k+n+1/2}$. To derive a simple estimate of when this inequality is satisfied, we set $\bar{m}_{k+n} = \delta^n \bar{m}_k$. The constraint on promoting the new object to a new bin then becomes:

$$\frac{(\delta^n + 1)\bar{m}_k}{\delta^{n+1/2}m_k} > 1 . \tag{A1}$$

Throughout a calculation, \bar{m}_k is distributed uniformly in the range $\delta^{-1/2} - \delta^{1/2} m_k$. The *minimum* \bar{m}_k which satisfies eq. (A1) is $\delta^{-1/2}m_k$. We can then write a much simpler inequality for promotion to a new bin:

$$\delta^{n+1} - \delta^n - 1 < 0 . \tag{A2}$$

When this inequality is satisfied, promotion to a new bin *always* occurs. Otherwise, promotion fails some fraction of the time. This failure is the source of the lag in all coagulation calculations with variable mass bins. The fraction of failures grows with increasing δ . Thus, the lag grows with larger δ .

Before describing results of our test calculations, it is worth examining several examples. When $n = 1$, we consider a simple collision between objects in adjacent mass bins. Calculations with $\delta \lesssim 1.62$ satisfy the inequality in eq. (A2). In solutions with $\delta > 1.62$, collisions fail to promote the merged object into a higher mass bin roughly 20% of the time. When merged objects are not promoted, the average mass of the largest object in the grid is smaller than the mass of a promoted object. Smaller objects have smaller collision rates and longer collision times. Thus, calculations with $\delta > 1.62$ always lag an ideal calculation for this simple merger.

As n increases, we consider collisions between objects with larger and larger mass ratios. Automatic promotion to the next bin requires smaller and smaller δ . When $n = 3, 10, 25$, or 62 , promotions never fail when $\delta \lesssim 1.38, 1.19, 1.10, 1.05$. For collisions with large n , smaller δ yields smaller failure rates. Thus, the lag declines with decreasing δ .

Previous discussions of the magnitude of the lag as a function of δ focus on the evolution of the overall size distribution (Wetherill 1990; Kenyon & Luu 1998; Morbidelli et al. 2009). Here, we illustrate the lag by following the growth of the largest object. In the first example, we consider growth when the cross-section is $A_{ij} = \gamma m_i m_j$ where γ is a constant. Defining the dimensionless time $\eta = \gamma n_0 t$ where n_0 is the initial number of particles with mass m_0 , there is an analytic solution for the size of the largest object as a function of n_0 and η (Wetherill 1990).

Fig. 17 compares results for four values of δ with the analytic solution. Independent of δ , r_{max} follows the same evolution: slow growth for $\eta \approx 0.0$ – 0.95 and exponential growth for $\eta \approx 1$. The precise timing of exponential growth depends on δ . Models with $\delta = 2$ reach the runaway when $\eta = 1.091$, lagging the exact solution by 9.1%. When $\delta = 1.05$, runaway begins when $\eta = 1.001$. With a lag of only 0.1%, these calculations almost precisely match the analytic solution.

Although solutions for $A_{ij} \propto m_i m_j$ provide excellent tests of a coagulation code, realistic cross-sections for particles in circumstellar disks are not as extreme (see also Wetherill 1990; Lee 2000; Malyshkin & Goodman 2001). When the collision rate depends solely on the geometric cross-section, $A_{ij} \propto (m_i + m_j)^{2/3}$. If gravitational focusing is important, $A_{ij} \propto (m_i + m_j)^{4/3}$. Calculating the evolution for either cross-section yields a more appropriate assessment of the lag as a function of δ in actual protostellar disks. With no analytic solution available, we adopt calculations with $\delta = 1.10$ as the reference. For clarity, we rescale the dimensionless time to place exponential growth for $\delta = 1.10$ at $\eta = 1$.

Fig. 18 compares results for six values of δ with $A_{ij} \propto (m_i + m_k)^{4/3}$ (see also Wetherill 1990). All solutions have the same form. Compared to the analytic model in Fig. 17, the largest object grows somewhat faster for $\eta = 0.0$ – 0.95 ; close to $\eta = 1$, runaway growth is somewhat less explosive. The timing of the runaway is very sensitive to δ . Models with $\delta = 2$ reach runaway roughly 40% later in time than models with $\delta = 1.05$.

When $A_{ij} \propto (m_i + m_j)^{2/3}$, growth is insensitive to δ (Fig. 19). Solutions with $\delta = 2$ lag calculations with $\delta = 1.1$ by less than 2%. Calculations with $\delta = 1.25$ – 1.7 have lags ranging from 0.5–1.5%. Thus, mass spacing has little impact on growth with purely geometric cross-sections (Wetherill 1990).

These examples suggest that δ is an important factor in models of runaway growth but not slow or oligarchic growth (see also Wetherill 1990). To confirm this point, Fig. 20 compares the evolution of r_{max} for complete evolutionary calculations with different values of δ . During an early phase of slow growth (when $t \lesssim 1$ Myr), 1 cm particles reach maximum

sizes of a few meters on time scales that are independent of δ . After runaway growth begins, small particles rapidly grow to km sizes. Once particles have $r_{max} \approx 0.1$ km, calculations with larger δ enter the oligarchic phase before those with smaller δ . Eventually all calculations reach oligarchic growth; the rate of growth is then fairly independent of δ . After several Gyr of evolution, all models have $r_{max} \approx 3000$ – 7000 km (Fig 20).

When $0.1 \text{ km} \lesssim r_{max} \lesssim 100 \text{ km}$, the growth times in these calculations depend on δ . For $\delta \lesssim 1.2$, the time scale to produce 100 km objects is $t_{100} \approx 500$ – 800 Myr. Although calculations for each δ exhibit a range in t_{100} , the median time to reach $r_{max} \approx 100$ km is independent of δ . For larger δ , the median growth time lags the $\delta \lesssim 1.2$ solutions by 10%–20% ($\delta = 1.41$) to 25%–50% ($\delta = 2.0$). Thus, calculations with $\delta \lesssim 1.2$ yield a better estimate of the time scale to produce 100 km objects.

As objects grow larger than 100 km, the growth time depends less on δ and more on the fragmentation history. For any δ , collisional damping of small fragments can enable a second runaway growth phase at $t \sim 100$ Myr to 1 Gyr. The timing and magnitude of this phase depends on (i) the amount of material available in small objects and (ii) the ability of collisional damping to reduce particle velocities significantly. Sometimes conditions allow the production of massive objects with $r_{max} \gtrsim 10^4$ km. Other simulations produce objects with $r_{max} \approx 3000$ – 4000 km.

A.2. Collisional Damping and Gravitational Stirring

In our coagulation calculations, we derive changes in particle velocities from collisional damping, dynamical friction, gas drag, and viscous stirring. Kenyon & Luu (1998, Appendix) and Kenyon & Bromley (2008, §2) describe the algorithms for each of these processes. Collisional damping is a central issue in this study; thus, we summarize our treatment for a single annulus. We then discuss results for several standard examples.

To treat collisional damping in a single annulus, we solve two sets of differential equations²:

$$\frac{dh_{in,k}^2}{dt} = \sum_{l=0}^{l=k} \frac{C_{in}}{2} (m_l h_l^2 - m_k h_k^2 - (m_k + m_l) h_k^2) I_e(\beta_{kl}) \quad (\text{A3})$$

and

$$\frac{dv_{in,ik}^2}{dt} = \sum_{l=0}^{l=k} \frac{C_{in}}{\beta_{kl}^2} (m_l v_l^2 - m_k v_k^2 - (m_k + m_l) v_k^2) I_i(\beta_{kl}) \quad (\text{A4})$$

²This discussion is adapted from the multiannulus approach of eqs. 8–9 from Kenyon & Bromley (2008). For a single annulus, we drop the subscripts for annulus i and annulus j and eliminate the term which treats the overlap between adjacent annuli.

where $C_{in} = \alpha_{coll} \epsilon_{kl} \rho_l V_{kl} F_{g,kl} (r_k + r_l)^2$, $\beta_{kl}^2 = (i_k^2 + i_l^2)/(e_k^2 + e_l^2)$, and ρ_l is the volume density of planetesimals with mass m_l (Wetherill & Stewart 1993; Kenyon & Luu 1998). In these expressions, $\alpha_{coll} = 0.57\text{--}0.855$ (Wetherill & Stewart 1993), $\epsilon_{jk} = 1/2$ for $k = l$ and 1 for $k \neq l$, V_{kl} is the relative particle velocity, and $F_{g,kl}$ is the gravitational focusing factor. The integrals I_e and I_i are elliptic integrals described in previous publications (e.g., Hornung et al. 1985; Wetherill & Stewart 1993).

Together with similar equations for coagulation, dynamical friction, gas drag, and viscous stirring (see Kenyon & Luu 1998; Kenyon & Bromley 2002a, 2008, and references therein), we solve these equations explicitly using an adaptive time step which conserves mass and kinetic energy to machine accuracy. We use more accurate and more cpu intensive fourth-order Runge Kutta and Richardson extrapolation algorithms to verify the explicit solutions. Kenyon & Luu (1998) summarize comparisons of our single annulus solutions for terrestrial planet formation with those of Wetherill & Stewart (1993).

To demonstrate our ability to treat collisional damping accurately, we consider several idealized problems. In the first test, we follow Levison & Morbidelli (2007) and consider the evolution of 1 cm particles in a single annulus at 30–35 AU. The particles have initial eccentricity $e_0 = 0.1$, inclination $i_0 = e_0/2$, mass density $\rho_s = 1 \text{ g cm}^{-3}$, and total mass $M_0 = 10 M_\oplus$. The calculations include gravitational stirring and collisional damping, but particles cannot merge or fragment during a collision.

Our results closely match those summarized in Levison & Morbidelli (2007) and Morbidelli et al. (2009). Particle random velocities damp rapidly and reach an equilibrium at $e_{eq} = 9.3 \times 10^{-10}$ and $i_{eq} = 5.1 \times 10^{-10}$ in 7300 yr (Fig. 21). The e-folding times of $t_e \approx 350$ yr and $t_i \approx 400$ yr are close to the Levison & Morbidelli (2007) results of 320 yr and 360 yr. The ratio $t_e/t_i = 0.875$ is essentially identical to their $t_e/t_i = 0.889$.

To compare this approach to analyses of Saturn’s rings (e.g., Goldreich & Tremaine 1978; Bridges et al. 1984; Supulver et al. 1995; Porco et al. 2008), we modify the damping algorithm. Defining the coefficient of restitution as

$$c_R = c_0 v_{rel}^{-k_R} , \tag{A5}$$

with $c_0 = 0\text{--}1$ and $k_R = 0.1\text{--}0.3$, the kinetic energy loss rate is $\delta E_{ij} = A_{ij} v_{ij} (1 - c_R^2)/V_{ij}$ where v_{ij} is the relative velocity of two particles and V_{ij} is the volume occupied by the particles. Replacing our standard loss term with δE_{ij} allows us to compare damping rates derived with two different approaches.

The grey lines in Fig. 21 plot results for $c_0 = 0.99$ (upper curve) and $c_0 = 0.01$ (lower curve) with $k_R = 0.15$. In these solutions, the e-folding times for the eccentricity are $t_e \approx 435$ yr ($c_0 = 0.99$) and 425 yr ($c_0 = 0.01$); for inclination, $t_i \approx 435$ yr ($c_0 = 0.99$) and 425 yr ($c_0 = 0.01$). Standard collisional damping in our calculations proceeds on time scales similar to models with a very small coefficient of restitution $c_0 \lesssim 10^{-3}$ (see also Kenyon & Luu 1999,

and references therein).

To test the evolution in an annulus relevant to the calculations described in the main text, we examine damping and stirring in a ring of mono-disperse particles with $\rho_s = 1.5 \text{ g cm}^{-3}$ and $M_0 = 15.79 M_\oplus$ at 112.5–137.5 AU. For the damping calculations, we set $e_0 = 10^2 e_{eq}$ and $i_0 = e_0/2$. To address time scales for gravitational stirring, we set $e_0 = 10^{-2} e_{eq}$ and $i_0 = e_0/2$.

In both sets of simulations, particles reach an equilibrium where the 3D velocity dispersion is roughly 60% of the escape velocity. The equilibrium has $h/v = 0.49$, $i/e = 0.55$, and $e_{eq} = 2.38 \times 10^{-4} (R/1 \text{ km})$. The time scales to reach equilibrium are typically much longer at 125 AU than at 30–35 AU (Figs. 22–23). When gravitational stirring dominates (Fig. 22), particles reach equilibrium on time scales ranging from ~ 1000 yr for 1 cm particles to roughly 1 Gyr for 10 km particles. Damping time scales are roughly a factor of 30 longer (Fig. 23).

Aside from validating the algorithms for stirring and damping, these simulations help us to set likely initial conditions for e and i at 125–250 AU. For a swarm of particles with velocity dispersion c_p , surface density Σ , and angular velocity Ω , the swarm is gravitationally unstable when $c_p \Omega < \pi G \Sigma$ (e.g., Chiang & Youdin 2010). Setting $\Sigma = \Sigma_0 (a/1 \text{ AU})^{-3/2}$, the swarm is gravitationally stable when the eccentricity has $e \gtrsim e_s$, where

$$e_s \approx 10^{-4} \left(\frac{\Sigma_0}{30 \text{ g cm}^{-2}} \right) \left(\frac{a}{100 \text{ AU}} \right)^{1/2}. \quad (\text{A6})$$

For our initial surface density at 125–250 AU, the minimum e for gravitational stability is $e_s \approx 10^{-4}$.

Particles with $r \gtrsim 0.4 \text{ km}$ have e_{eq} larger than e_s . At 125–250 AU, these particles reach equilibrium on time scales longer than the lifetime of the protosolar nebula and other protoplanetary disks (e.g., Dauphas & Pourmand 2011; Williams & Cieza 2011; Cloutier et al. 2014, and references therein). Thus, we can safely set e_0 somewhere between e_s and e_{eq} .

Although particles with radii $r \approx 10\text{--}100 \text{ m}$ have $e_q < e_s$, the time scale to reach this equilibrium is longer than the disk lifetime. On these time scales, particles also grow considerably (see Figs. 1–2). Thus, we set $e_0 \approx e_s$.

Particles with much smaller radii $r \approx 1\text{--}100 \text{ cm}$ reach very small equilibrium e on relatively short time scales, $\sim 0.05\text{--}5 \text{ Myr}$. For our adopted Σ and $e_0 = 10^{-4}$, these particles grow on similar time scales. To avoid the complications of gravitational instabilities, we also set $e_0 = e_s$ for these particles.

In any swarm of particles at 125–250 AU, the likely e and i depend on the evolutionary history, which is sensitive to the structure of the disk. In this paper, the adopted e_0 and i_0 are intermediate between the e_{eq} and values expected for a turbulent disk. The calculations

in §4 describe how these choices impact our results. The discussion in §5 considers how to improve these choices.

REFERENCES

- Adachi, I., Hayashi, C., & Nakazawa, K. 1976, *Progress of Theoretical Physics*, 56, 1756
- Andrews, S. M., & Williams, J. P. 2005, *ApJ*, 631, 1134
- Andrews, S. M., Wilner, D. J., Hughes, A. M., Qi, C., & Dullemond, C. P. 2009, *ApJ*, 700, 1502
- . 2010, *ApJ*, 723, 1241
- Arakawa, M., Leliwa-Kopystynski, J., & Maeno, N. 2002, *Icarus*, 158, 516
- Benavidez, P. G., Durda, D. D., Enke, B. L., Bottke, W. F., Nesvorný, D., Richardson, D. C., Asphaug, E., & Merline, W. J. 2012, *Icarus*, 219, 57
- Benz, W., & Asphaug, E. 1999, *Icarus*, 142, 5
- Birnstiel, T., Andrews, S. M., & Ercolano, B. 2012, *A&A*, 544, A79
- Birnstiel, T., Dullemond, C. P., & Brauer, F. 2010, *A&A*, 513, A79+
- Bottke, W. F., Nesvorný, D., Vokrouhlický, D., & Morbidelli, A. 2010, *AJ*, 139, 994
- Bower, E. C. 1931, *Lick Observatory Bulletin*, 15, 171
- Bridges, F. G., Hatzes, A., & Lin, D. N. C. 1984, *Nature*, 309, 333
- Bromley, B. C., & Kenyon, S. J. 2006, *AJ*, 131, 2737
- . 2011a, *ApJ*, 731, 101
- . 2011b, *ApJ*, 735, 29
- . 2013, *ApJ*, 764, 192
- . 2014, *ApJ*, 796, 141
- Brouwer, D. 1955, *MNRAS*, 115, 221
- Burchell, M. J., Leliwa-Kopystyński, J., & Arakawa, M. 2005, *Icarus*, 179, 274
- Burns, J. A., Lamy, P. L., & Soter, S. 1979, *Icarus*, 40, 1

- Campo Bagatin, A., Cellino, A., Davis, D. R., Farinella, P., & Paolicchi, P. 1994, *Planet. Space Sci.*, 42, 1079
- Chambers, J. 2008, *Icarus*, 198, 256
- Chambers, J. E. 2009, *ApJ*, 705, 1206
- . 2014, *Icarus*, 233, 83
- Chiang, E., Kite, E., Kalas, P., Graham, J. R., & Clampin, M. 2009, *ApJ*, 693, 734
- Chiang, E., & Youdin, A. N. 2010, *Annual Review of Earth and Planetary Sciences*, 38, 493
- Cloutier, R., Currie, T., Rieke, G. H., Kenyon, S. J., Balog, Z., & Jayawardhana, R. 2014, *ApJ*, 796, 127
- Corder, S., et al. 2009, *ApJ*, 690, L65
- Crida, A., Masset, F., & Morbidelli, A. 2009, *ApJ*, 705, L148
- Currie, T., et al. 2012, *ApJ*, 760, L32
- . 2014, *ApJ*, 796, L30
- Dauphas, N., & Pourmand, A. 2011, *Nature*, 473, 489
- Davis, D. R., Chapman, C. R., Weidenschilling, S. J., & Greenberg, R. 1985, *Icarus*, 63, 30
- Davis, M., Hut, P., & Muller, R. A. 1984, *Nature*, 308, 715
- de la Fuente Marcos, C., & de la Fuente Marcos, R. 2014, *MNRAS*, 443, L59
- Dohnanyi, J. S. 1969, *J. Geophys. Res.*, 74, 2531
- Durda, D. D., Bottke, W. F., Enke, B. L., Merline, W. J., Asphaug, E., Richardson, D. C., & Leinhardt, Z. M. 2004, *Icarus*, 170, 243
- Durda, D. D., Bottke, W. F., Nesvorný, D., Enke, B. L., Merline, W. J., Asphaug, E., & Richardson, D. C. 2007, *Icarus*, 186, 498
- Fernández, J. A. 2011, *ApJ*, 726, 33
- Fraser, W. C. 2009, *ApJ*, 706, 119
- Furlan, E., et al. 2006, *ApJS*, 165, 568
- . 2009, *ApJ*, 703, 1964
- Galicher, R., Marois, C., Zuckerman, B., & Macintosh, B. 2013, *ApJ*, 769, 42

- Garaud, P., Meru, F., Galvagni, M., & Olczak, C. 2013, *ApJ*, 764, 146
- Gáspár, A., Rieke, G. H., & Balog, Z. 2013, *ApJ*, 768, 25
- Giblin, I., Davis, D. R., & Ryan, E. V. 2004, *Icarus*, 171, 487
- Gladman, B., Marsden, B. G., & Vanlaerhoven, C. 2008, in *The Solar System Beyond Neptune*, ed. Barucci, M. A., Boehnhardt, H., Cruikshank, D. P., & Morbidelli, A. (University of Arizona Press, Tucson, AZ), 43–57
- Goldreich, P., Lithwick, Y., & Sari, R. 2004, *ARA&A*, 42, 549
- Goldreich, P., & Tremaine, S. D. 1978, *Icarus*, 34, 227
- Gomes, R. S., Matese, J. J., & Lissauer, J. J. 2006, *Icarus*, 184, 589
- Haisch, Jr., K. E., Lada, E. A., & Lada, C. J. 2001, *ApJ*, 553, L153
- Harrington, R. S. 1988, *AJ*, 96, 1476
- Hogg, D. W., Quinlan, G. D., & Tremaine, S. 1991, *AJ*, 101, 2274
- Holsapple, K. A. 1994, *Planet. Space Sci.*, 42, 1067
- Hornung, P., Pellat, R., & Barge, P. 1985, *Icarus*, 64, 295
- Housen, K. R., & Holsapple, K. A. 1990, *Icarus*, 84, 226
- . 1999, *Icarus*, 142, 21
- . 2011, *Icarus*, 211, 856
- Hugot, E., Ferrari, M., El Hadi, K., Costille, A., Dohlen, K., Rabou, P., Puget, P., & Beuzit, J. L. 2012, *A&A*, 538, A139
- Ida, S., Bryden, G., Lin, D. N. C., & Tanaka, H. 2000, *ApJ*, 534, 428
- Ida, S., & Lin, D. N. C. 2008, *ApJ*, 673, 487
- Ida, S., & Makino, J. 1992a, *Icarus*, 96, 107
- . 1992b, *Icarus*, 98, 28
- Inaba, S., Wetherill, G. W., & Ikoma, M. 2003, *Icarus*, 166, 46
- Iorio, L. 2009, *MNRAS*, 400, 346
- . 2012, *Celestial Mechanics and Dynamical Astronomy*, 112, 117
- . 2014, *MNRAS*, 444, L78

- Johansen, A., Oishi, J. S., Mac Low, M.-M., Klahr, H., Henning, T., & Youdin, A. 2007, *Nature*, 448, 1022
- Johansen, A., Youdin, A. N., & Lithwick, Y. 2012, *A&A*, 537, A125
- Jovanovic, N., et al. 2013, in *Proceedings of the Third AO4ELT Conference*, ed. S. Esposito & L. Fini
- Jurić, M., & Tremaine, S. 2008, *ApJ*, 686, 603
- Kalas, P., Graham, J. R., & Clampin, M. 2005, *Nature*, 435, 1067
- Kalas, P., Graham, J. R., Fitzgerald, M. P., & Clampin, M. 2013, *ArXiv e-prints*
- Kennedy, G. M., & Wyatt, M. C. 2011, *MNRAS*, 412, 2137
- Kenyon, S. J. 2002, *PASP*, 114, 265
- Kenyon, S. J., & Bromley, B. C. 2001, *AJ*, 121, 538
- . 2002a, *AJ*, 123, 1757
- . 2002b, *ApJ*, 577, L35
- . 2004a, *AJ*, 127, 513
- . 2004b, *ApJ*, 602, L133
- . 2004c, *Nature*, 432, 598
- . 2004d, *AJ*, 128, 1916
- . 2006, *AJ*, 131, 1837
- . 2008, *ApJS*, 179, 451
- . 2010, *ApJS*, 188, 242
- . 2012, *AJ*, 143, 63
- . 2014, *AJ*, 147, 8
- Kenyon, S. J., Currie, T., & Bromley, B. C. 2014, *ApJ*, 786, 70
- Kenyon, S. J., & Luu, J. X. 1998, *AJ*, 115, 2136
- . 1999, *AJ*, 118, 1101
- Kirsh, D. R., Duncan, M., Brasser, R., & Levison, H. F. 2009, *Icarus*, 199, 197

- Kleine, T., et al. 2009, *Geochim. Cosmochim. Acta*, 73, 5150
- Kobayashi, H., & Löhne, T. 2014, *MNRAS*, 442, 3266
- Kobayashi, H., & Tanaka, H. 2010, *Icarus*, 206, 735
- Kobayashi, H., Tanaka, H., Krivov, A. V., & Inaba, S. 2010, *Icarus*, 209, 836
- Kretke, K. A., Levison, H. F., Buie, M. W., & Morbidelli, A. 2012, *AJ*, 143, 91
- Krijt, S., & Kama, M. 2014, *A&A*, 566, L2
- Krist, J. E., Stapelfeldt, K. R., Bryden, G., & Plavchan, P. 2012, *AJ*, 144, 45
- Krist, J. E., et al. 2010, *AJ*, 140, 1051
- Krivov, A. V., Löhne, T., & Sremčević, M. 2006, *A&A*, 455, 509
- Krivov, A. V., Müller, S., Löhne, T., & Mutschke, H. 2008, *ApJ*, 687, 608
- Lagrange, A.-M., et al. 2010, *Science*, 329, 57
- Lambrechts, M., & Johansen, A. 2012, *A&A*, 544, A32
- . 2014, *ArXiv e-prints*
- Lee, M. H. 2000, *Icarus*, 143, 74
- Leinhardt, Z. M., & Stewart, S. T. 2009, *Icarus*, 199, 542
- . 2012, *ApJ*, 745, 79
- Leinhardt, Z. M., Stewart, S. T., & Schultz, P. H. 2008, in *The Solar System Beyond Neptune*, ed. Barucci, M. A., Boehnhardt, H., Cruikshank, D. P., & Morbidelli, A. (University of Arizona Press, Tucson, AZ), 195–211
- Levison, H. F., Lissauer, J. J., & Duncan, M. J. 1998, *AJ*, 116, 1998
- Levison, H. F., & Morbidelli, A. 2007, *ArXiv Astrophysics e-prints*
- Löhne, T., et al. 2012, *A&A*, 537, A110
- Love, S. G., & Ahrens, T. J. 1996, *Icarus*, 124, 141
- Lowell, P. 1915, *Memoir on a Trans-Neptunian Planet* (Press of T. P. Nichols, Lynn, MA)
- Luhman, K. L. 2014, *ApJ*, 781, 4
- Lykawka, P. S., & Mukai, T. 2008, *AJ*, 135, 1161

- Lynden-Bell, D., & Pringle, J. E. 1974, MNRAS, 168, 603
- Macintosh, B., et al. 2014, ArXiv e-prints
- Malyshkin, L., & Goodman, J. 2001, Icarus, 150, 314
- Marshall, J. P., et al. 2011, A&A, 529, A117
- Masset, F. S., & Papaloizou, J. C. B. 2003, ApJ, 588, 494
- Matese, J. J., Whitman, P. G., & Whitmire, D. P. 1999, Icarus, 141, 354
- Michikoshi, S., Inutsuka, S.-i., Kokubo, E., & Furuya, I. 2007, ApJ, 657, 521
- Michikoshi, S., Kokubo, E., & Inutsuka, S.-i. 2009, ApJ, 703, 1363
- Morbidelli, A. 2013, Dynamical Evolution of Planetary Systems, ed. T. D. Oswalt, L. M. French, & P. Kalas (Dordrecht: Springer Science & Business Media), 63
- Morbidelli, A., Bottke, W. F., Nesvorný, D., & Levison, H. F. 2009, Icarus, 204, 558
- Morbidelli, A., & Levison, H. F. 2004, AJ, 128, 2564
- Najita, J. R., & Kenyon, S. J. 2014, MNRAS, 445, 3315
- O’Brien, D. P., & Greenberg, R. 2003, Icarus, 164, 334
- Ohtsuki, K. 1999, Icarus, 137, 152
- Ohtsuki, K., & Nakagawa, Y. 1988, Progress of Theoretical Physics Supplement, 96, 239
- Ohtsuki, K., Nakagawa, Y., & Nakazawa, K. 1990, Icarus, 83, 205
- Ohtsuki, K., Stewart, G. R., & Ida, S. 2002, Icarus, 155, 436
- Ormel, C. W., & Klahr, H. H. 2010, A&A, 520, A43
- Pan, M., & Sari, R. 2005, Icarus, 173, 342
- Petit, J.-M., et al. 2011, ArXiv e-prints
- Porco, C. C., Weiss, J. W., Richardson, D. C., Dones, L., Quinn, T., & Throop, H. 2008, AJ, 136, 2172
- Rafikov, R. R. 2004, AJ, 128, 1348
- Rasio, F. A., & Ford, E. B. 1996, Science, 274, 954
- Rawlins, D. 1970, AJ, 75, 856

- . 1972, *Nature*, 240, 457
- Raymond, S. N., et al. 2011, *A&A*, 530, A62
- Ricci, L., Carpenter, J. M., Fu, B., Hughes, A. M., Corder, S., & Isella, A. 2014, *ArXiv e-prints*
- Ryan, E. V., Davis, D. R., & Giblin, I. 1999, *Icarus*, 142, 56
- Schlichting, H. E., Fuentes, C. I., & Trilling, D. E. 2013, *AJ*, 146, 36
- Schlichting, H. E., & Sari, R. 2011, *ApJ*, 728, 68
- Spaute, D., Weidenschilling, S. J., Davis, D. R., & Marzari, F. 1991, *Icarus*, 92, 147
- Standish, E. M. 1993, *AJ*, 105, 2000
- Stark, C. C., & Kuchner, M. J. 2009, *ApJ*, 707, 543
- Stepinski, T. F. 1998, *Icarus*, 132, 100
- Stern, S. A. 2005, *AJ*, 129, 526
- Stern, S. A., & Colwell, J. E. 1997, *AJ*, 114, 841
- Supulver, K. D., Bridges, F. G., & Lin, D. N. C. 1995, *Icarus*, 113, 188
- Tanaka, H., Inaba, S., & Nakazawa, K. 1996, *Icarus*, 123, 450
- Thébault, P., Kral, Q., & Ertel, S. 2012, *A&A*, 547, A92
- Trujillo, C. A., & Sheppard, S. S. 2014, *Nature*, 507, 471
- Ward, W. R. 1997, *Icarus*, 126, 261
- Weidenschilling, S. J. 1977, *MNRAS*, 180, 57
- . 1989, *Icarus*, 80, 179
- . 2010, *ApJ*, 722, 1716
- Weidenschilling, S. J., Spaute, D., Davis, D. R., Marzari, F., & Ohtsuki, K. 1997, *Icarus*, 128, 429
- Wetherill, G. W. 1990, *Icarus*, 88, 336
- Wetherill, G. W., & Stewart, G. R. 1989, *Icarus*, 77, 330
- . 1993, *Icarus*, 106, 190

- Whitmire, D. P., & Jackson, A. A. 1984, *Nature*, 308, 713
- Williams, D. R., & Wetherill, G. W. 1994, *Icarus*, 107, 117
- Williams, J. P., & Cieza, L. A. 2011, *ARA&A*, 49, 67
- Windmark, F., Birnstiel, T., Ormel, C. W., & Dullemond, C. P. 2012, *A&A*, 544, L16
- Youdin, A. N., & Goodman, J. 2005, *ApJ*, 620, 459
- Youdin, A. N., & Kenyon, S. J. 2013, *From Disks to Planets*, ed. T. D. Oswalt, L. M. French, & P. Kalas (Dordrecht: Springer Science & Business Media), 1
- Zakamska, N. L., & Tremaine, S. 2005, *AJ*, 130, 1939

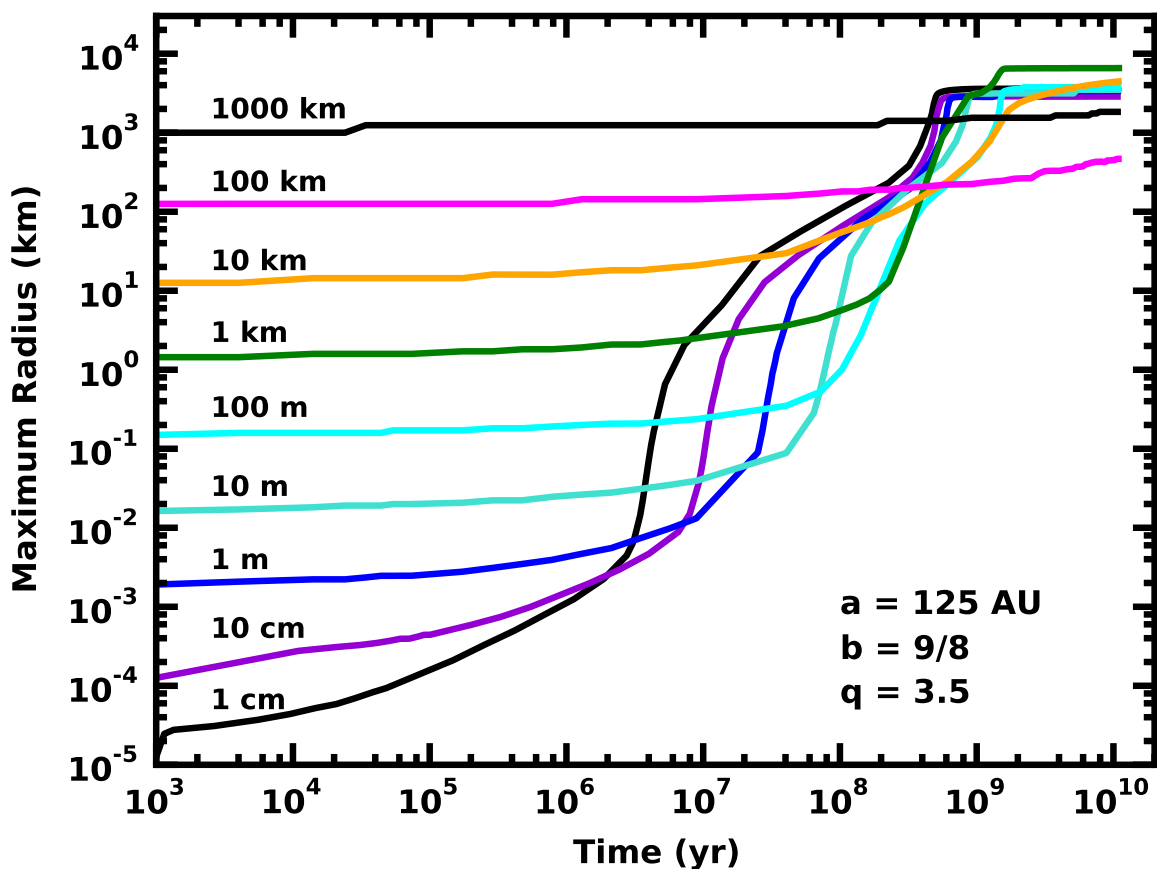


Fig. 1.— Growth of the largest object at 125 AU as a function of initial planetesimal size for calculations with $b = 9/8$ and $q = 3.5$. Although simulations starting with smaller planetesimals produce large planets faster than those with larger planetesimals, all systems with $M_0 \approx 15.8 M_\oplus$ and $r_0 \lesssim 10 \text{ km}$ yield planets with $r_{max} \approx 3000\text{--}6000 \text{ km}$. In rings with $r_0 \gtrsim 100 \text{ km}$, collisions are too infrequent to produce planets with $r_{max} \gtrsim 500\text{--}2000 \text{ km}$.

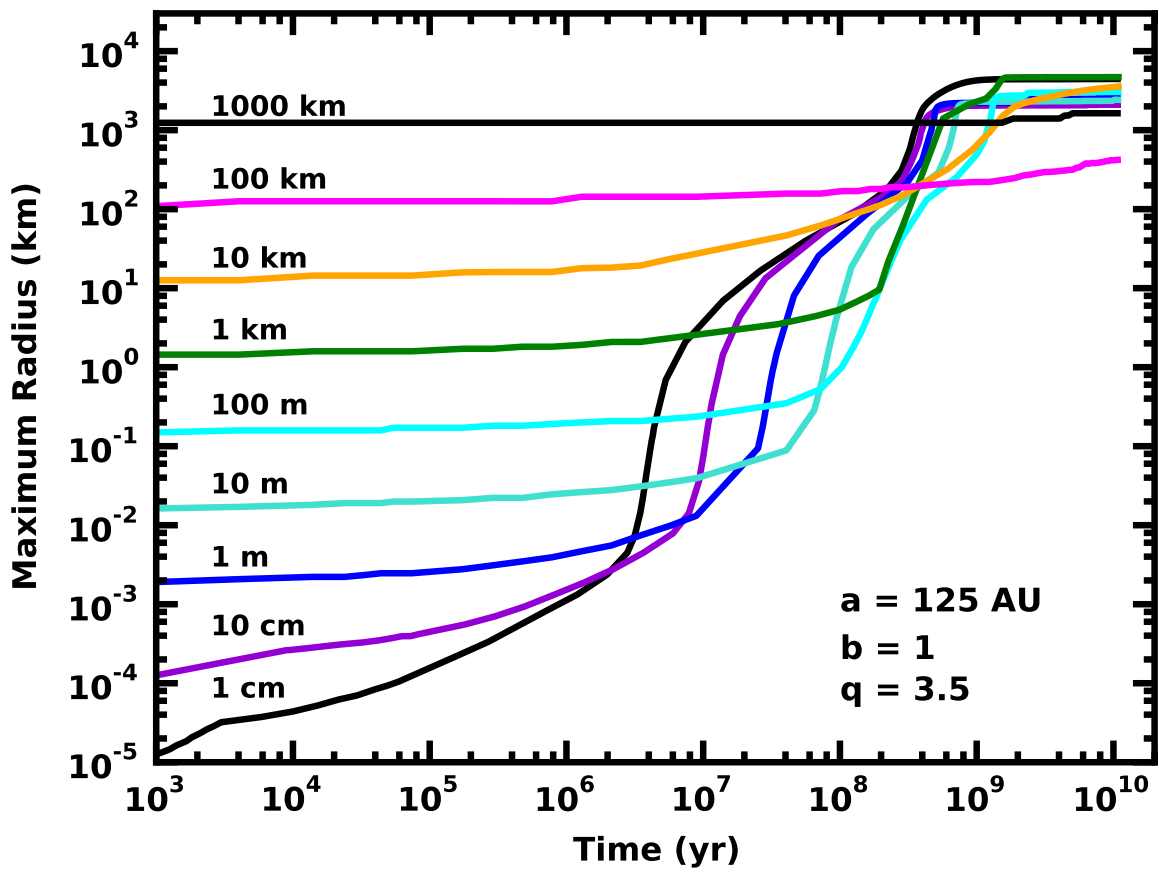


Fig. 2.— As in Fig. 1 for calculations with $b = 1$.

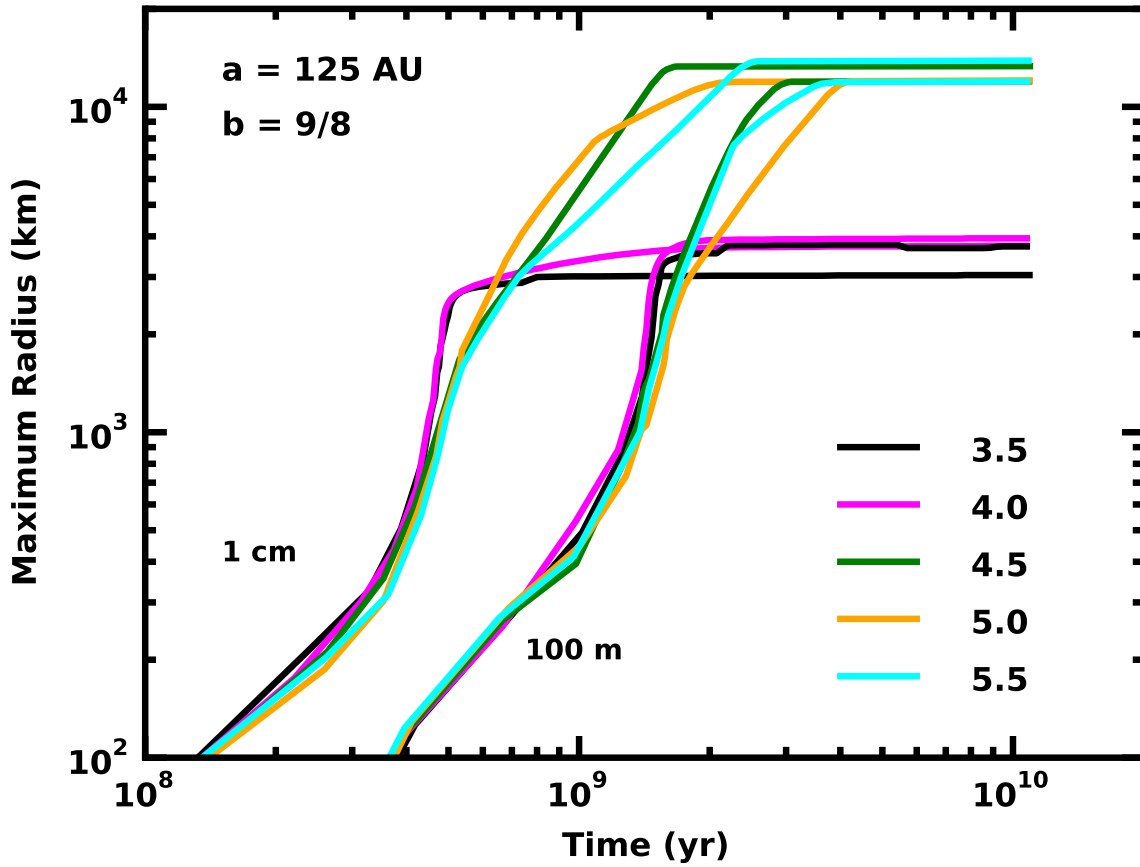


Fig. 3.— As in Fig. 1 for calculations with $r_0 = 1$ cm or 100 m, $b = 9/8$, and various q as indicated in the legend. In calculations with $q \gtrsim 4.5$, planets reach super-Earth masses in 1–3 Gyr.

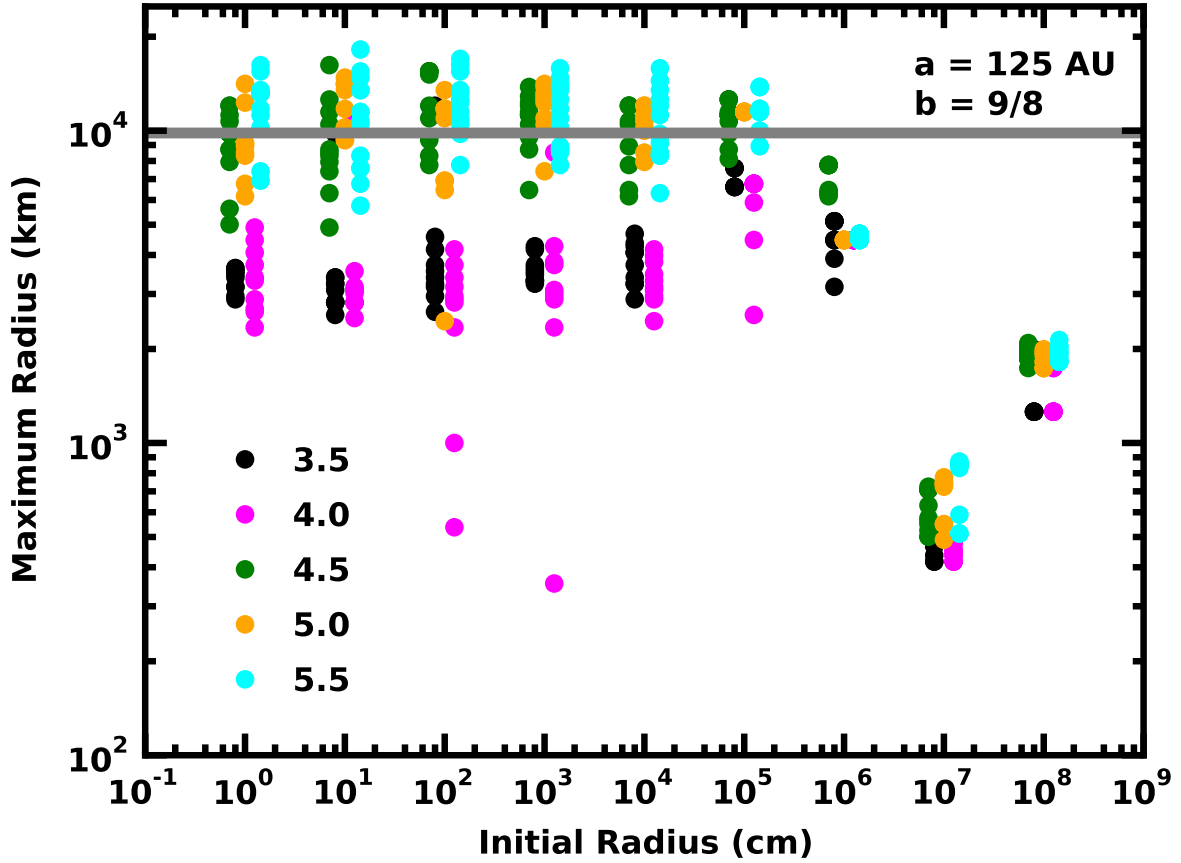


Fig. 4.— Maximum planet radius at $a = 125$ AU as a function of r_0 and q for $b = 9/8$. To improve clarity, points are slightly offset from the nominal r_0 . The horizontal grey bar indicates the radius of an Earth-mass planet with $\rho_s = 1.5 \text{ g cm}^{-3}$. Calculations with $r_0 = 1 \text{ cm}$ to 1 km and $q \gtrsim 4.5$ produce super-Earth mass planets.

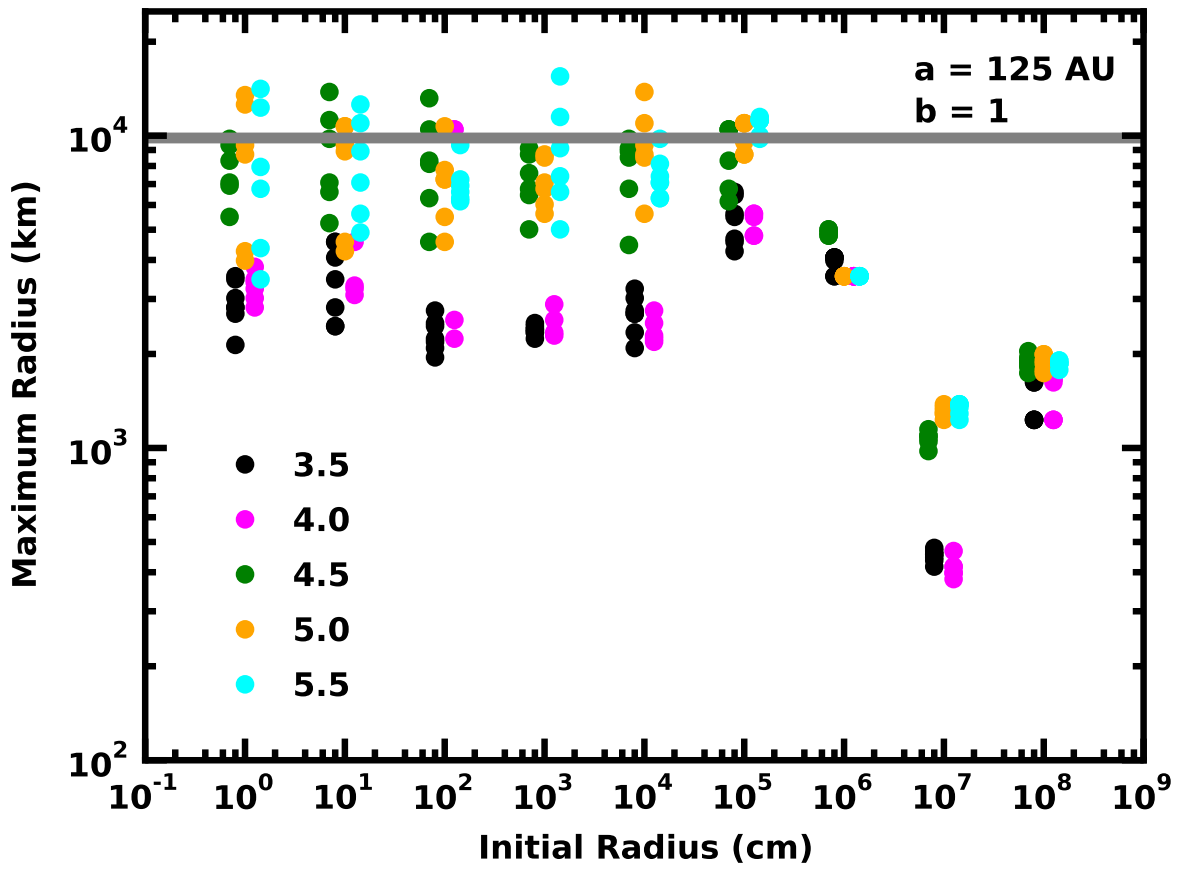


Fig. 5.— As in Fig. 4 for calculations with $b = 1$.

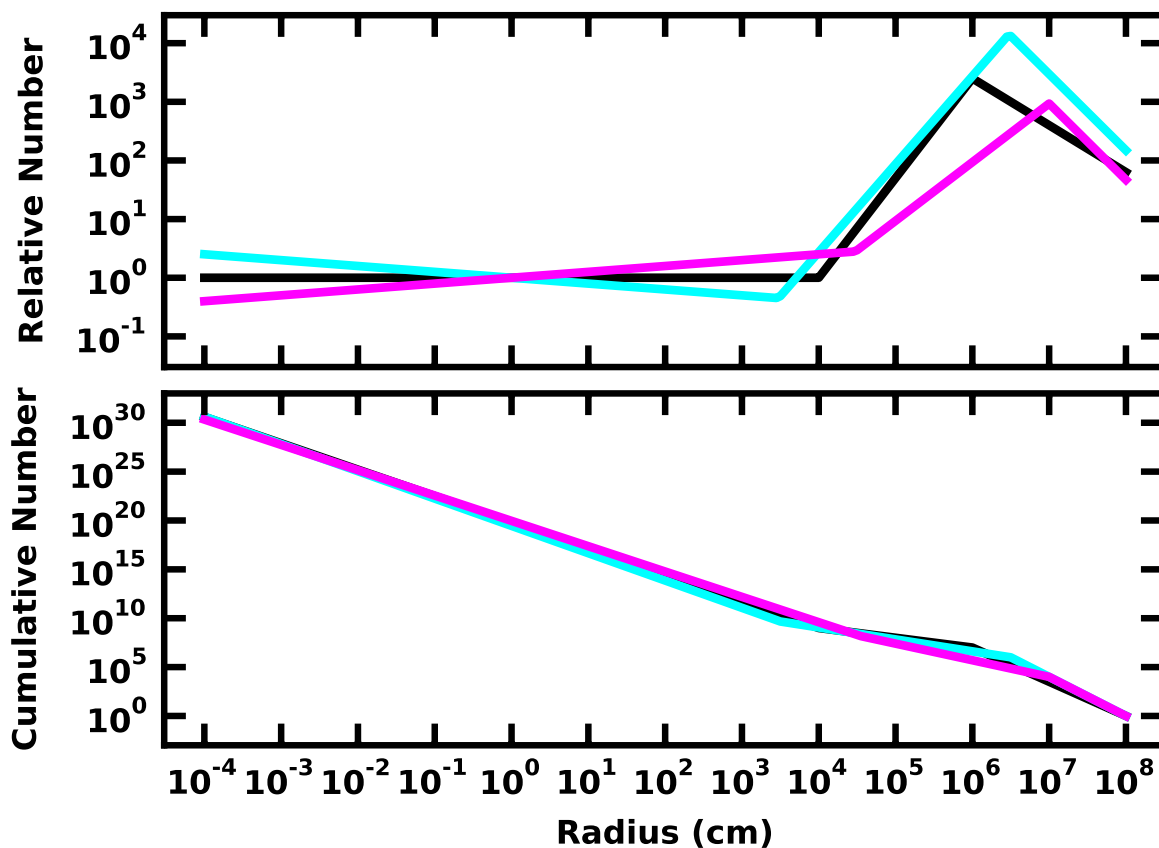


Fig. 6.— Comparison of cumulative (lower panel) and relative cumulative (upper panel) size distributions for three idealized power law size distributions. To construct the relative size distribution, we adopt a normalization with $q_s = 2.7$ which yields $n_{c,rel} \equiv 1$ at $r = 1$ cm. *Black curves:* $n_l = 1$, $q_s = 2.7$, $q_i = 1.0$, $q_l = 3.5$, $r_1 = 0.1$ km, $r_2 = 10$ km. *Cyan curves:* $n_l = 1$, $q_s = 2.8$, $q_i = 1.2$, $q_l = 4.0$, $r_1 = 0.03$ km, $r_2 = 30$ km. *Magenta curves:* $n_l = 1$, $q_s = 2.6$, $q_i = 1.7$, $q_l = 4.0$. $r_1 = 0.3$ km, $r_2 = 100$ km. Relative size distributions allow an easier assessment of the differences between power-law components.

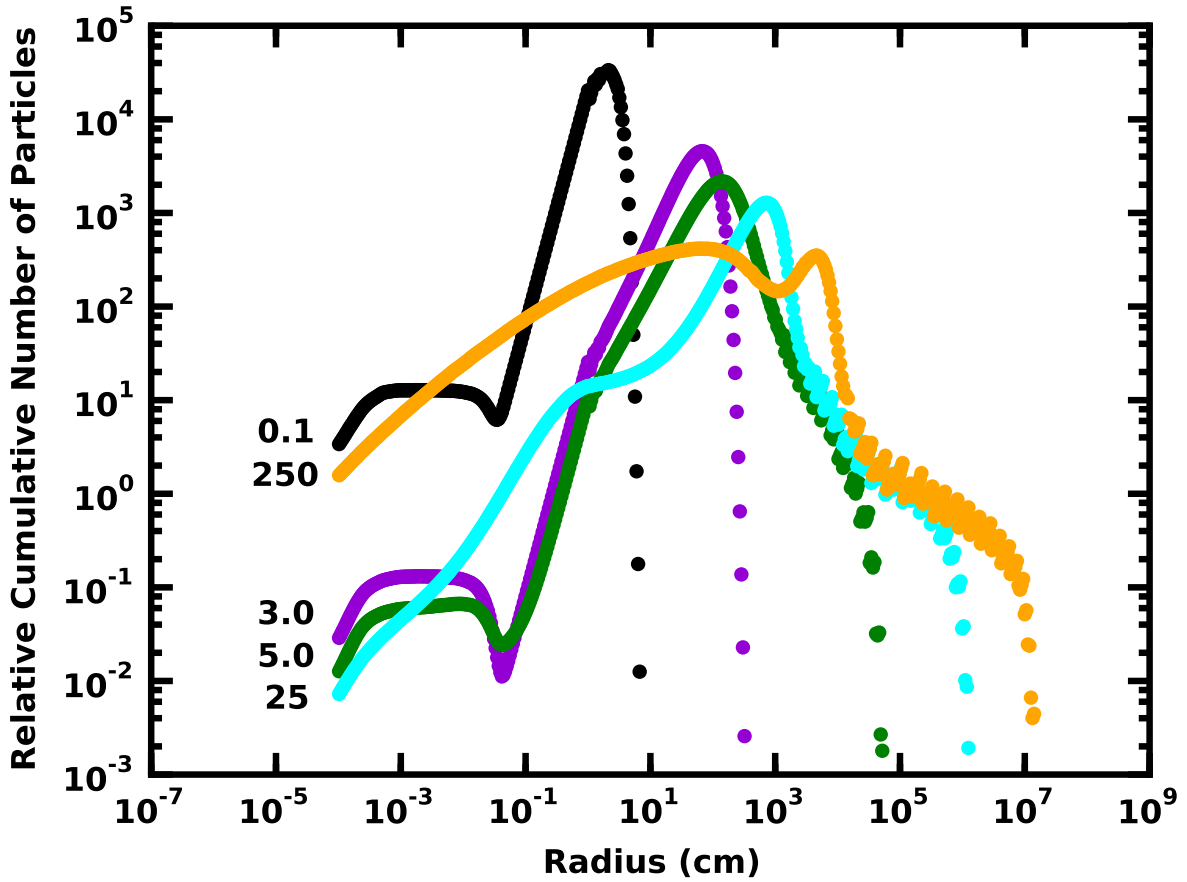


Fig. 7.— Evolution of the relative cumulative size distribution $n_{c,rel}$ for a calculation with $r_0 = 1$ cm, $B = 9/8$, and $q = 3.5$. Here, $n_{c,rel} = n_c/n_r$ where n_c is the cumulative number distribution from the calculation, $n_r = n_0 r^{-2.5}$, and $n_0 = 10^{23}$. Numbers to the left of each curve indicate time in Myr.

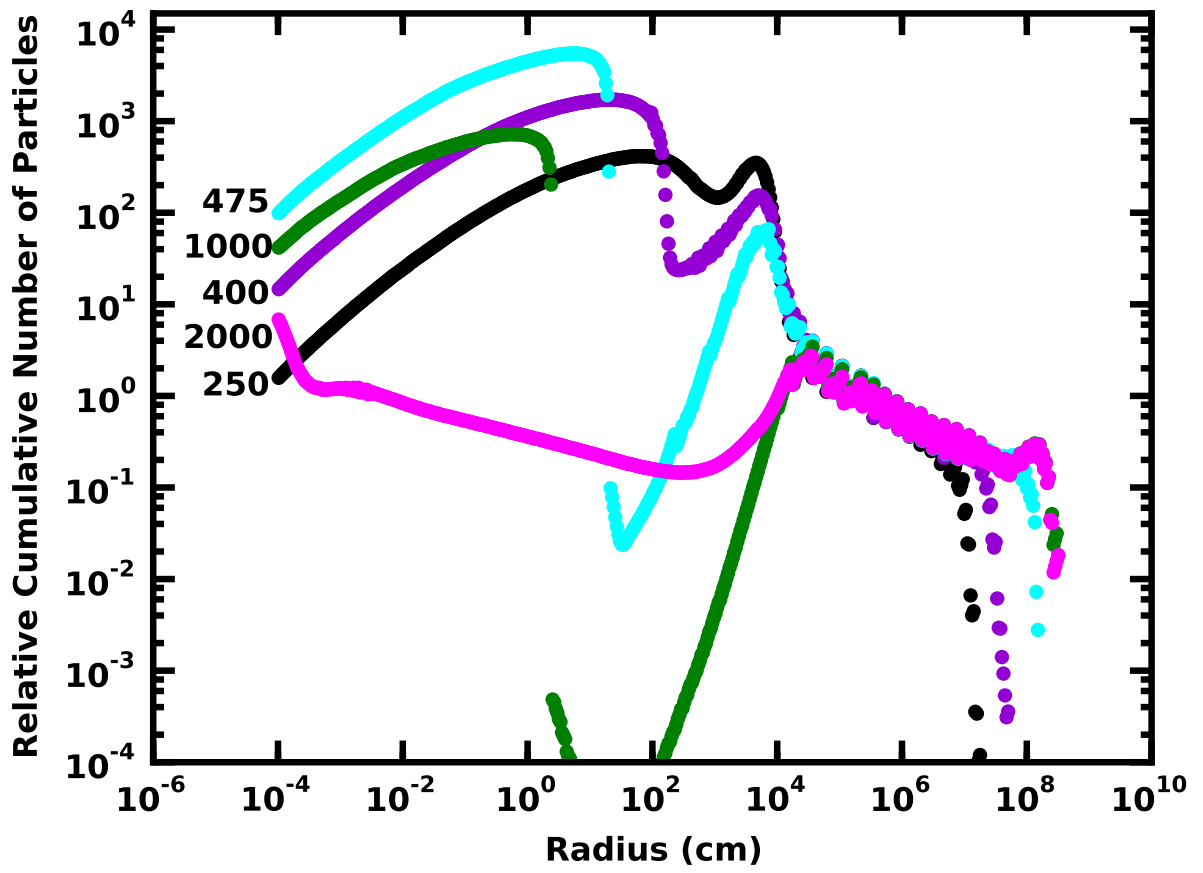


Fig. 8.— As in Fig. 7 for later epochs.

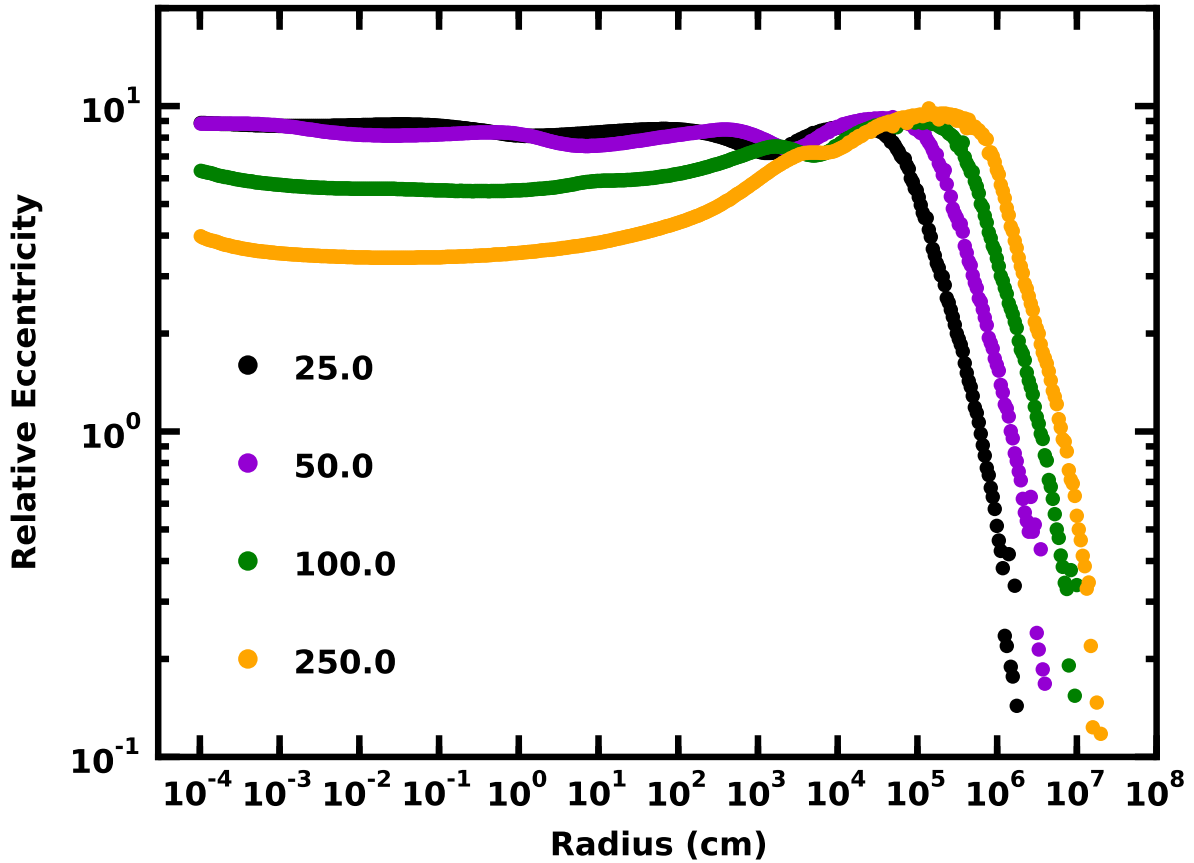


Fig. 9.— Evolution of the relative eccentricity e_H in Hill units for a calculation with $r_0 = 1$ cm, $B = 9/8$, and $q = 3.5$ at times (in Myr) indicated in the legend. As the maximum particle size grows, small particles maintain $e_H \approx 10$. At larger sizes ($r \gtrsim 0.03 r_{max}$), the eccentricity follows a power law $e_H \approx 0.2(r/r_{max})^{-1}$.

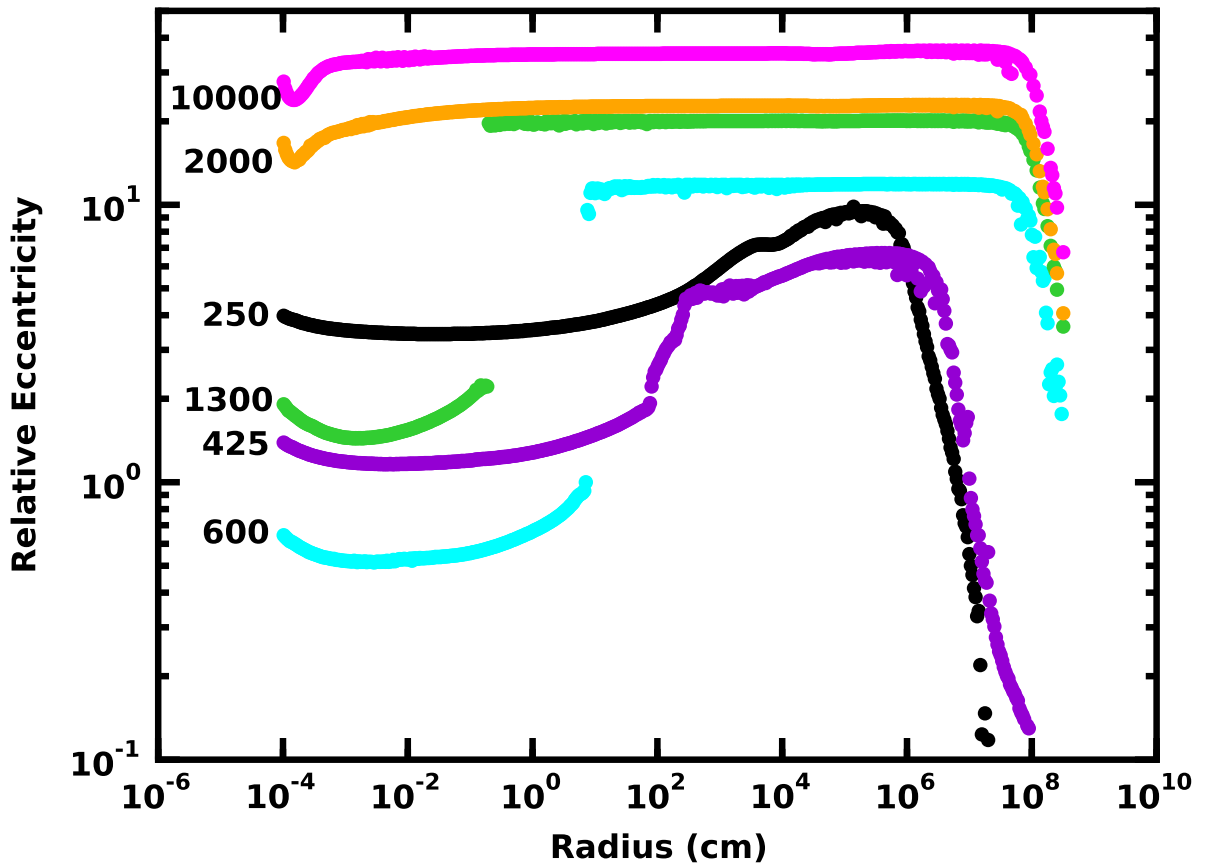


Fig. 10.— As in Fig. 9 for later epochs. As the evolution proceeds, collisional damping depresses the eccentricity for small particles. Once these particles have been swept up or destroyed, the eccentricity of small particles rises.

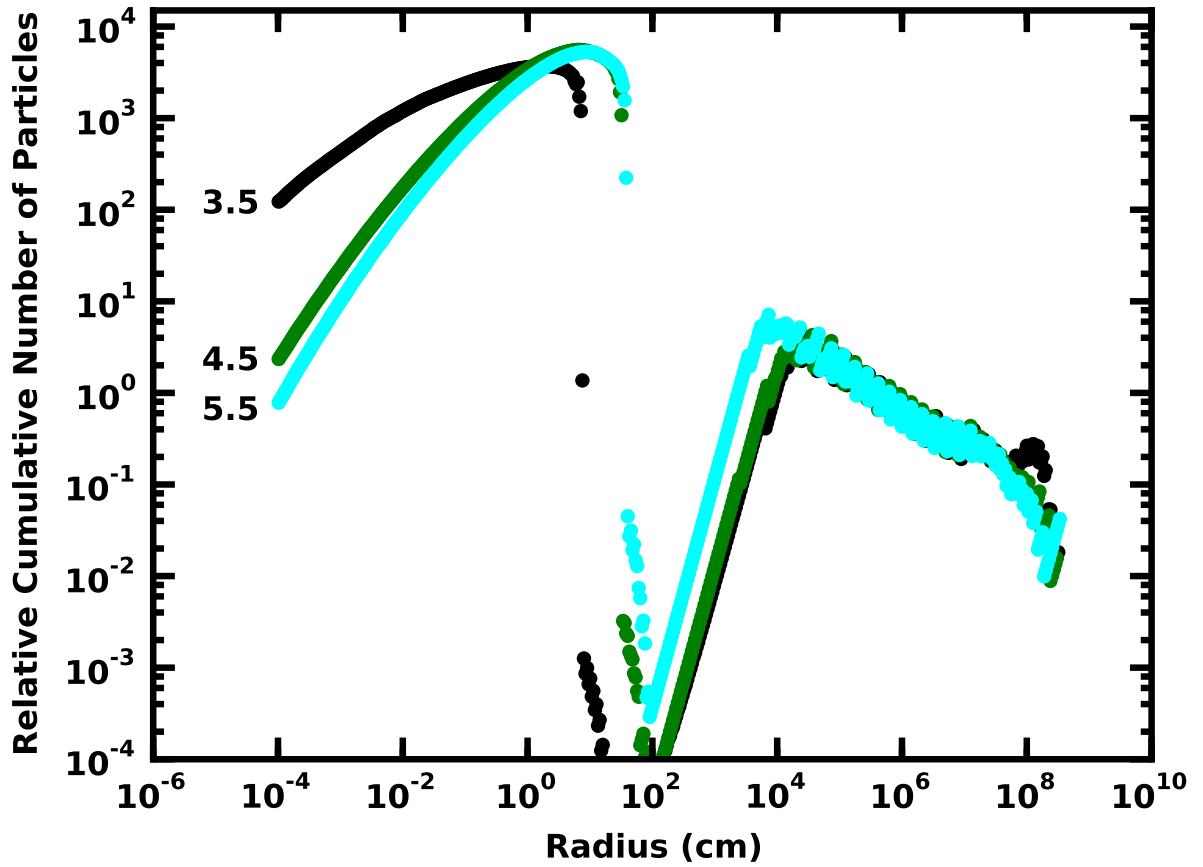


Fig. 11.— Relative cumulative size distributions when $r_{max} = 3000$ km for calculations with $q = 3.5$ (black points), 4.5 (green points), and 5.5 (cyan points). Calculations with larger q have more material in particles with $r = 1$ cm to 0.1 km and less material in particles with $r \gtrsim 1$ cm.

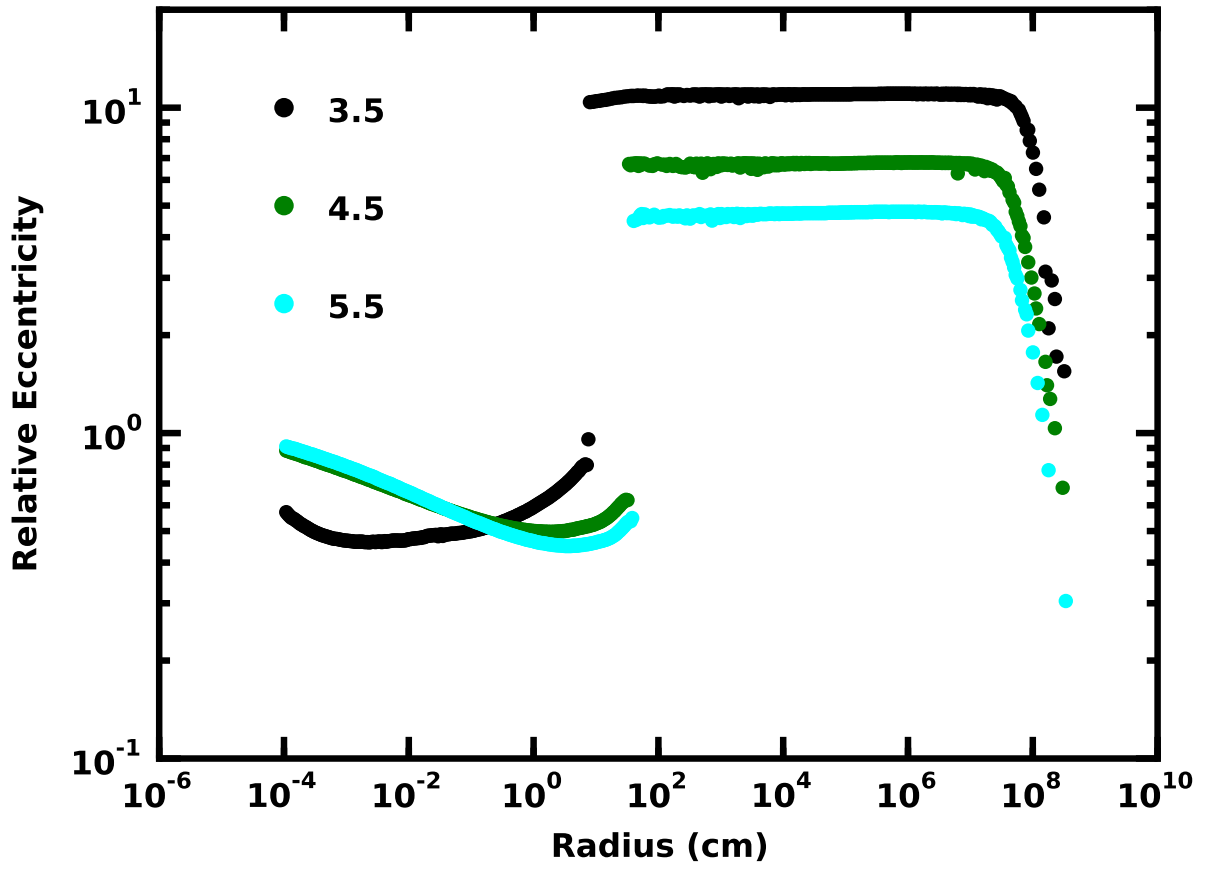


Fig. 12.— As in Fig. 11 for the relative eccentricity. In calculations with larger q , particles with $r \gtrsim 1$ cm have smaller $e_{k,rel}$; smaller particles have larger $e_{k,rel}$.

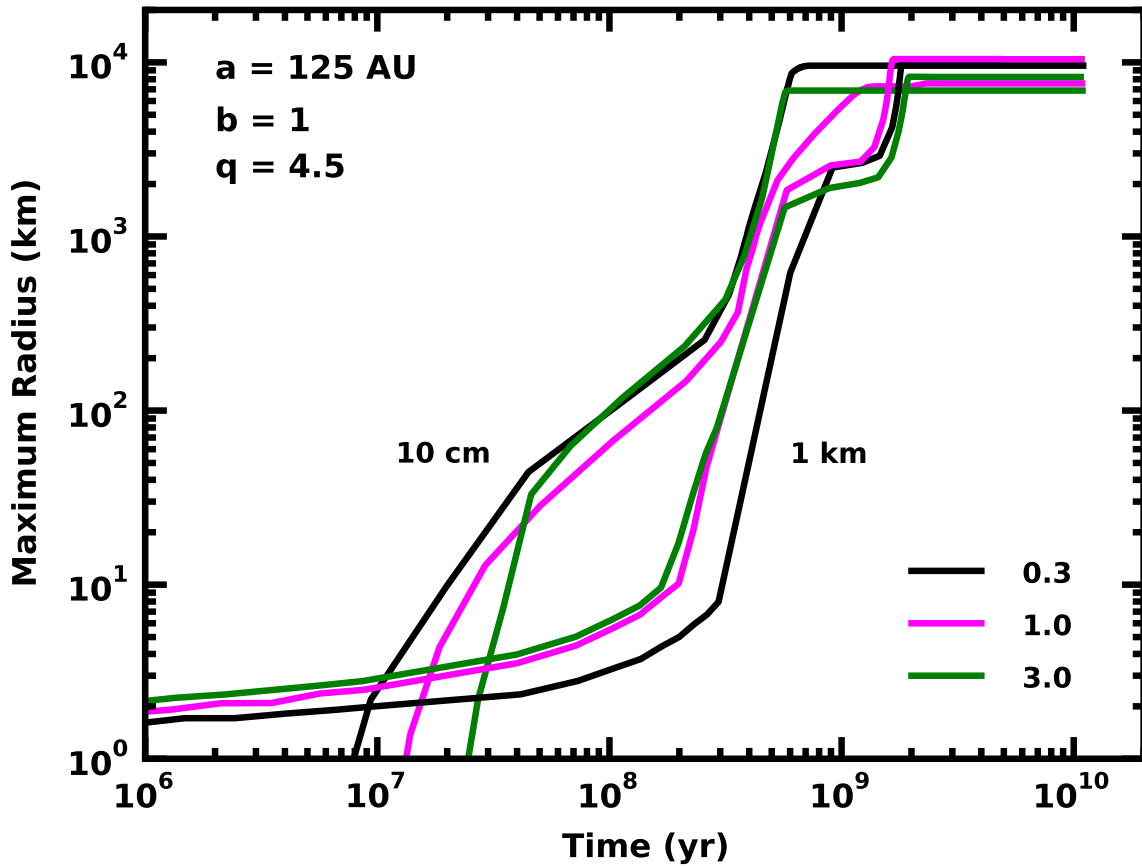


Fig. 13.— Growth of the largest object as a function of initial eccentricity. For the two particle sizes considered ($r_0 = 10$ cm and 1 km), the legend in the lower right corner indicates the initial eccentricity relative to the nominal e_0 . Overall, growth is fairly independent of the initial e and i .

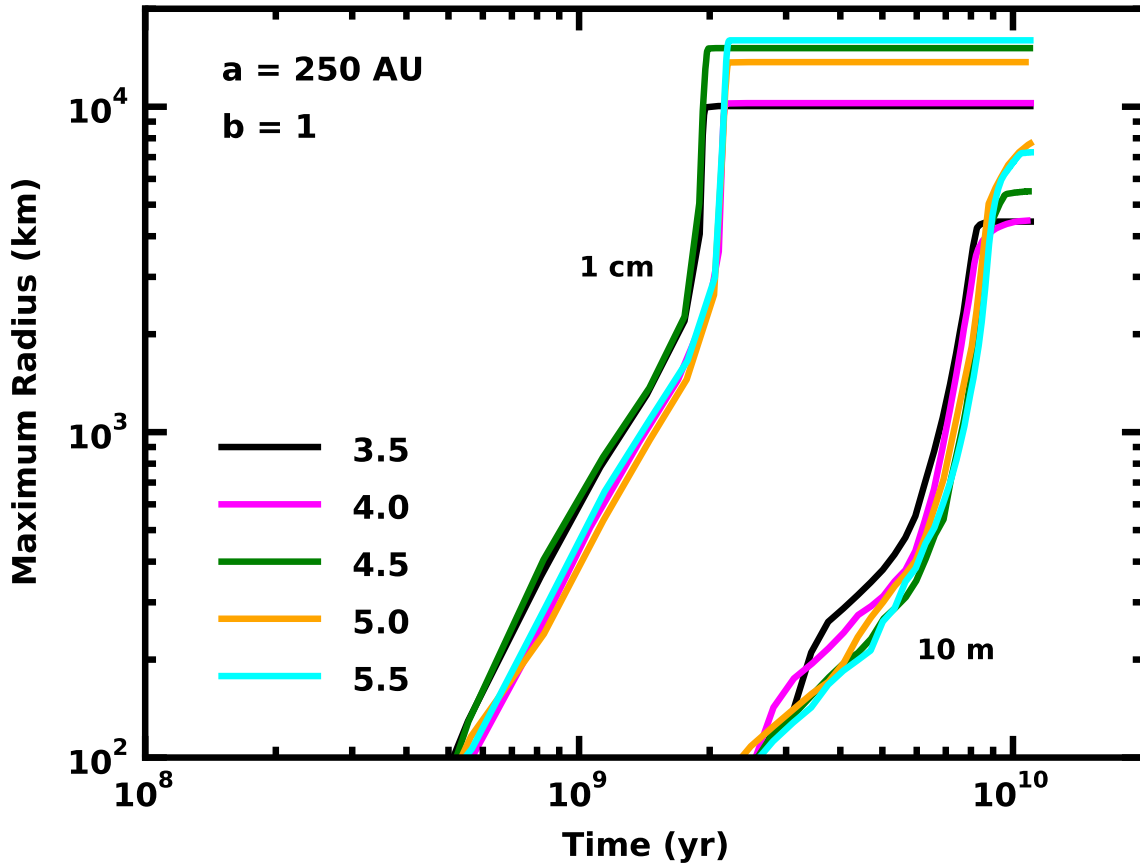


Fig. 14.— Growth of the largest object at 250 AU as a function of q for $b = 1$ and $r_0 = 1$ cm and 10 m. For rings of small particles with $r_0 = 1$ –10 cm, coagulation produces super-Earth mass planets for all q in 2–4 Gyr. Larger particles with $r_0 \gtrsim 10$ m cannot grow into super-Earths over the age of the Solar System.

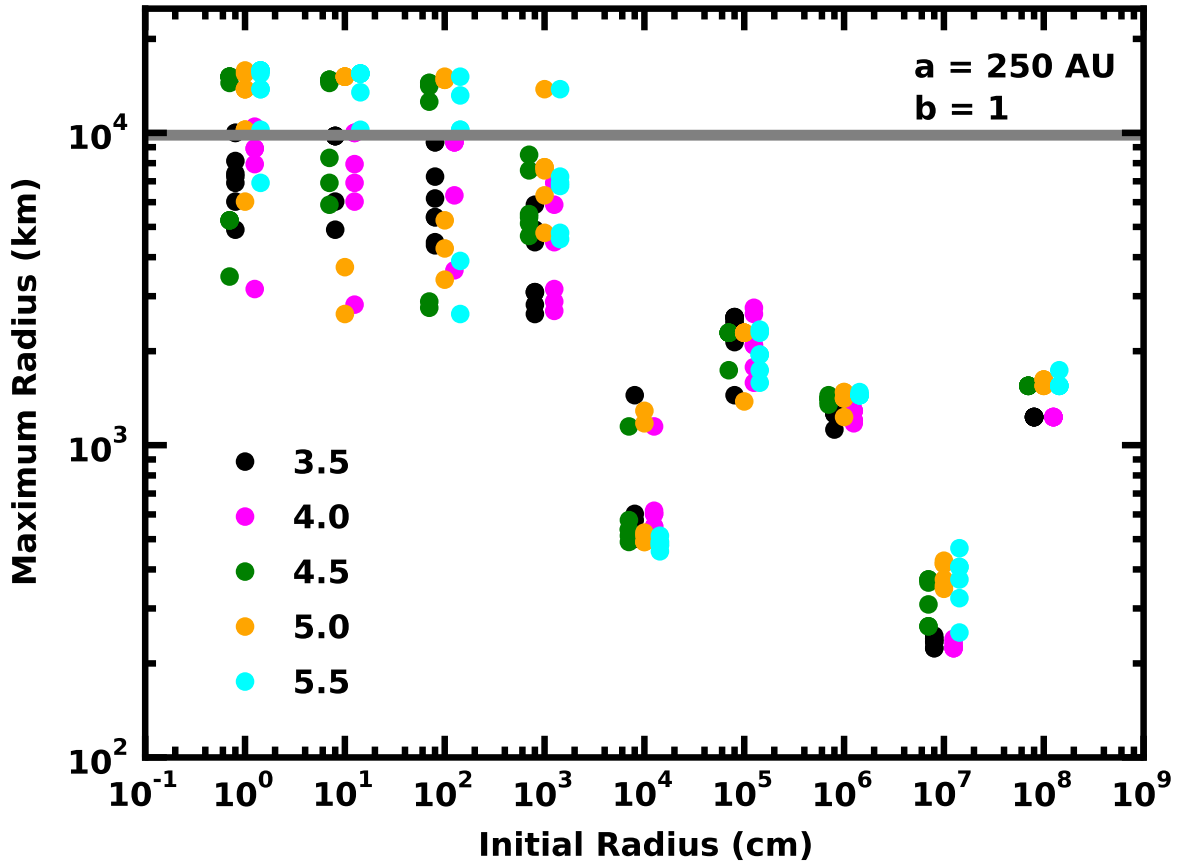


Fig. 15.— Maximum planet radius at $a = 250$ AU as a function of r_0 and q for $b = 1$. To improve clarity, points are slightly offset from the nominal r_0 . The horizontal grey bar indicates the radius of an Earth-mass planet with $\rho_s = 1.5 \text{ g cm}^{-3}$. Calculations with $r_0 = 1 \text{ cm}$ to 1 m produce super-Earth mass planets. Larger planetesimals evolve into much smaller planets on 1–10 Gyr time scales.

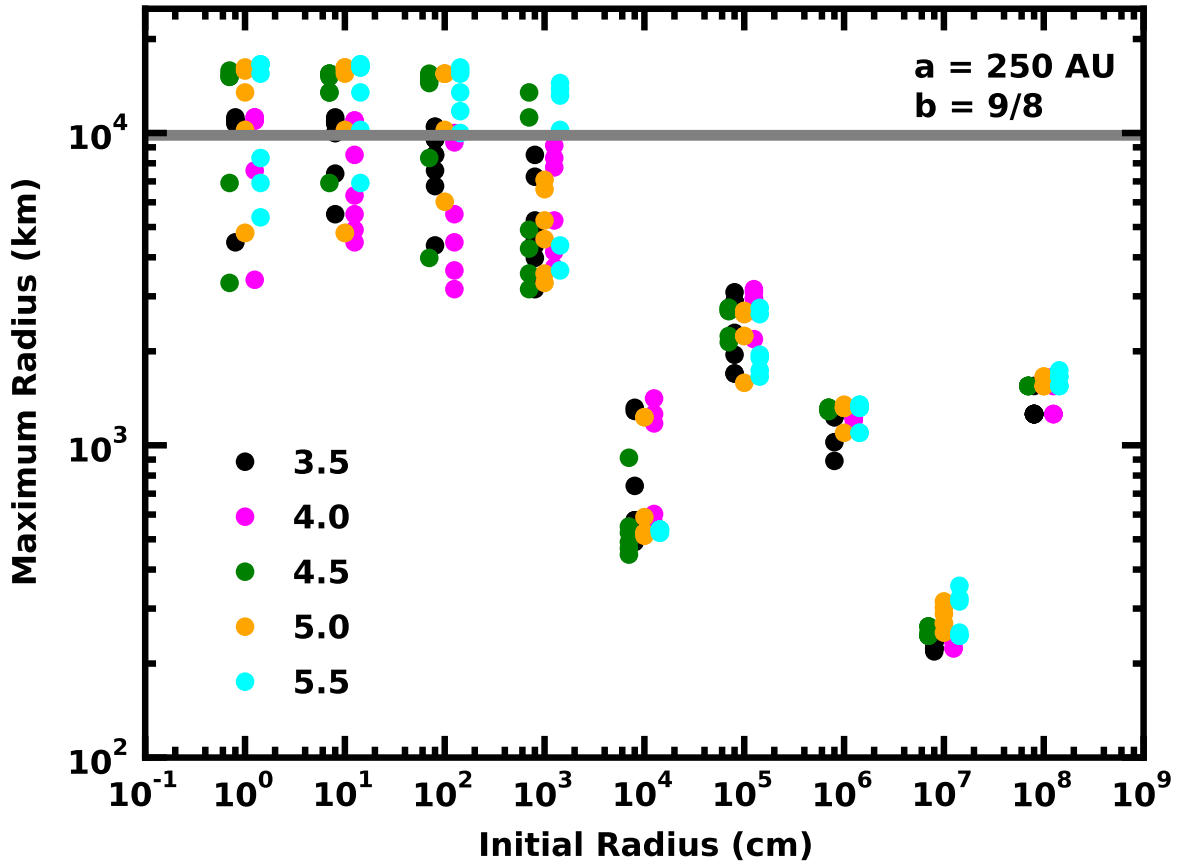


Fig. 16.— As in Fig. 15 for calculations with $b = 9/8$. On 1–4 Gyr time scales, super-Earths form from planetesimals with $r_0 = 1$ cm to 1 m. Occasionally, ensembles of 10 m planetesimals can grow into 1–2 super-Earths if $q \gtrsim 4.5$. Larger planetesimals produce planets with radii ranging from a few hundred km to a few thousand km.

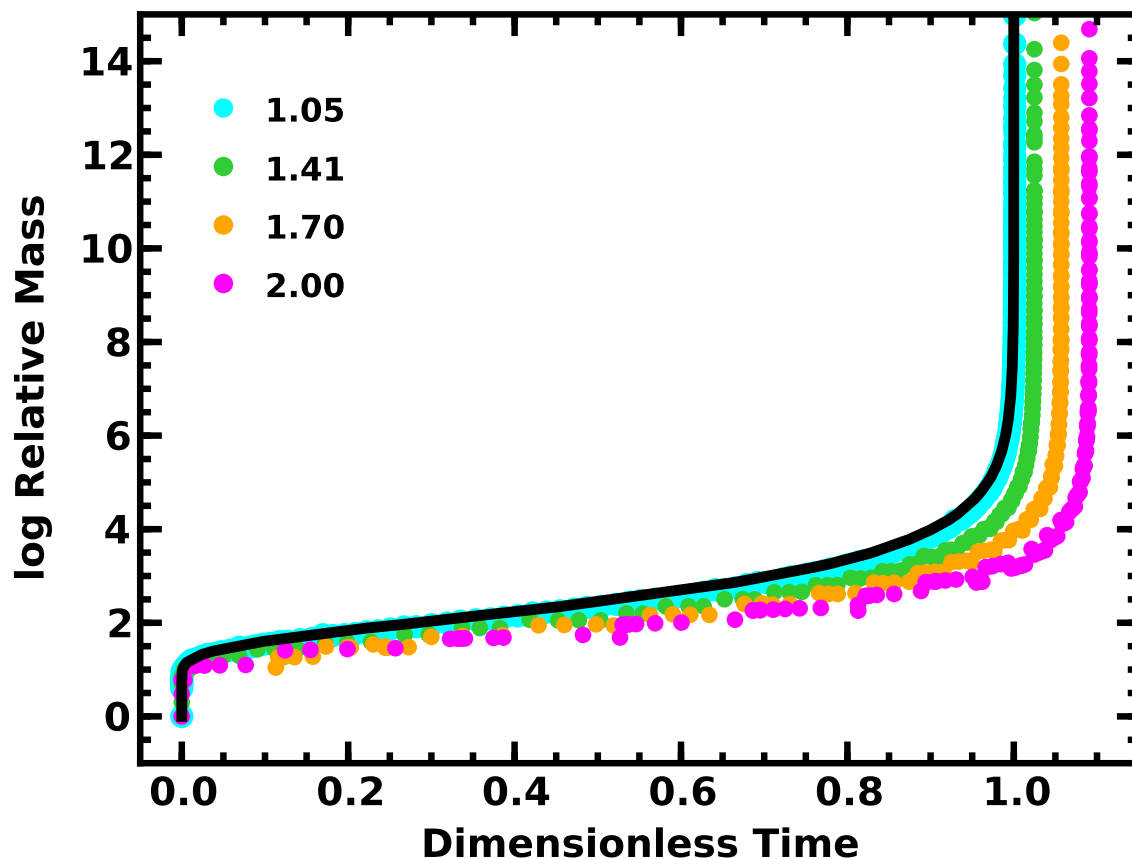


Fig. 17.— Mass of the largest object as a function of dimensionless time η for cross-section $A_{ij} \propto m_i m_j$. The solid black line plots the analytic solution. Colored points show results for numerical solutions with different values for the mass spacing factor δ as summarized in the legend. The numerical solutions lag the analytic solution by 9.1% ($\delta = 2.0$), 5.7% ($\delta = 1.7$), 2.5% ($\delta = 1.4$), 2.0% ($\delta = 1.25$), 0.3% ($\delta = 1.1$), and 0.1% ($\delta = 1.05$). Although calculations with $\delta = 1.05$ follow the analytic result almost exactly, solutions with $\delta \leq 1.4$ yield satisfactory approximations to the exact result.

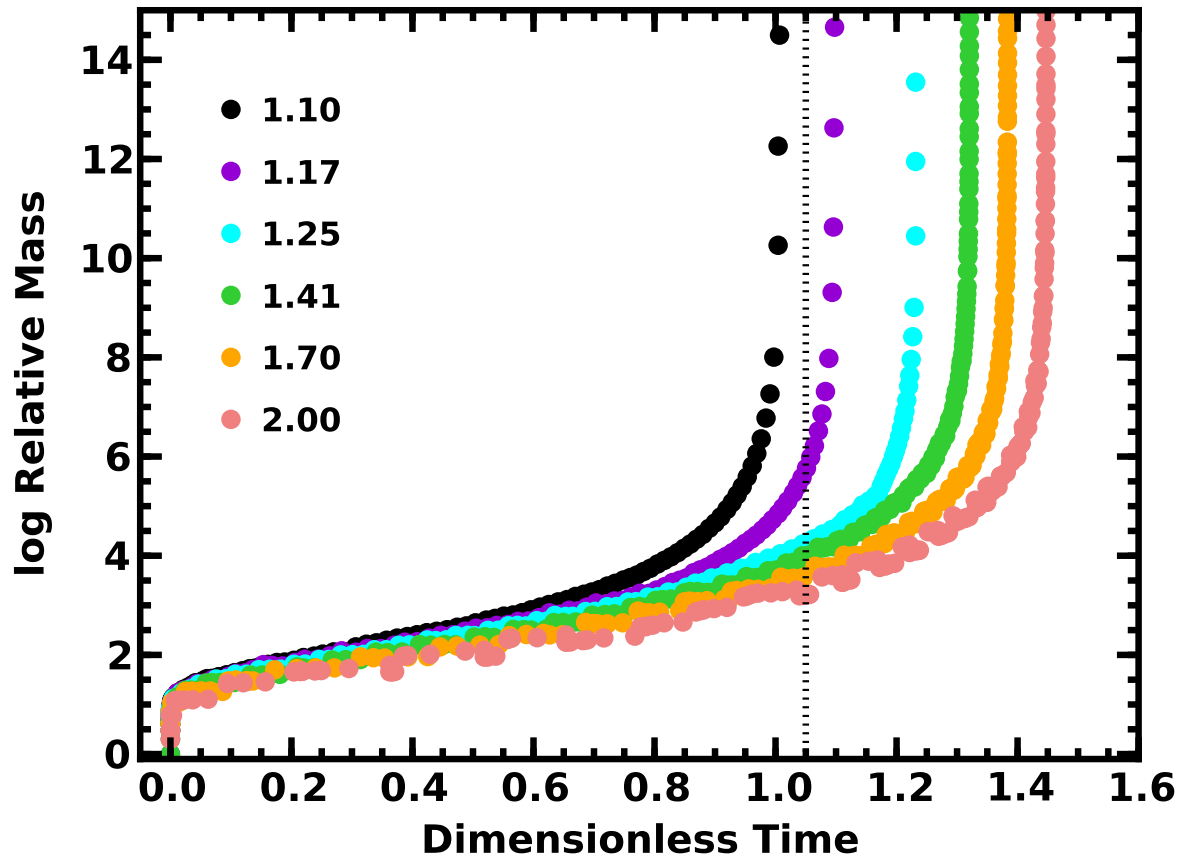


Fig. 18.— As in Fig. 17 for $A_{ij} \propto (m_i m_j)^{2/3}$. The numerical solutions lag the $\delta = 1.10$ result by 43.7% ($\delta = 2.0$), 37.4% ($\delta = 1.7$), 31.1% ($\delta = 1.4$), 22.5% ($\delta = 1.25$), and 9.0% ($\delta = 1.17$).

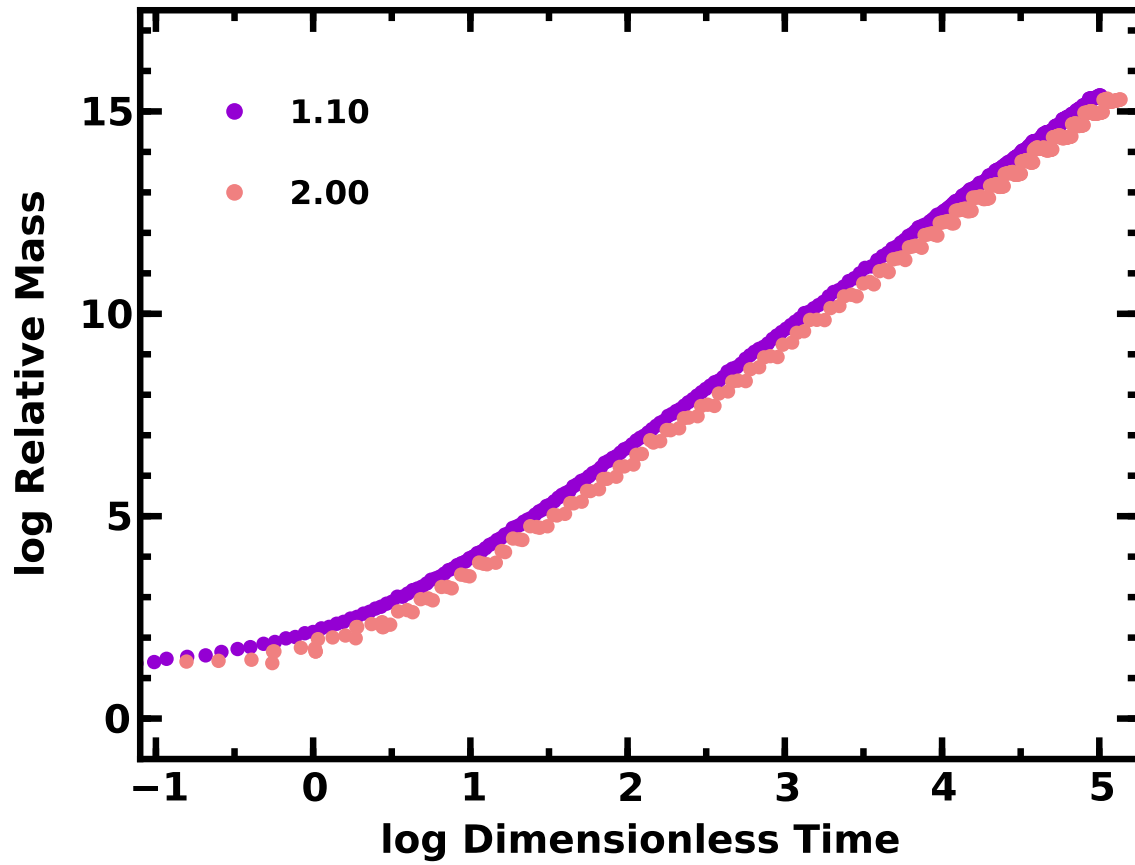


Fig. 19.— As in Fig. 18 for $A_{ij} \propto (m_i m_j)^{1/3}$. The numerical solutions lag the $\delta = 1.10$ result by 1.9% ($\delta = 2.0$), 1.6% ($\delta = 1.7$), 1.3% ($\delta = 1.4$), 1.0% ($\delta = 1.25$), and 0.5% ($\delta = 1.17$).

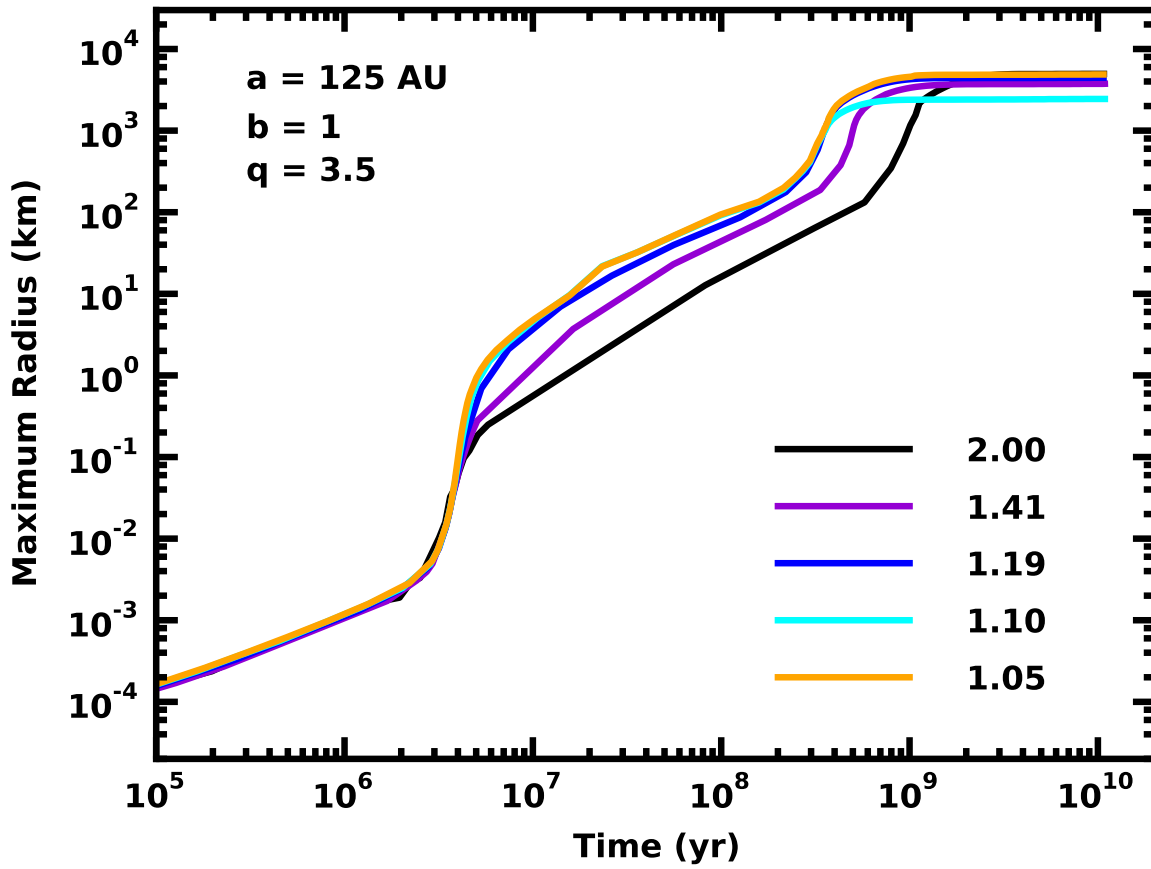


Fig. 20.— Growth of 1 cm particles at $a = 125$ AU as a function of mass spacing parameter δ . Although all calculations produce objects with similar r_{max} , simulations with large δ lag those with smaller δ .

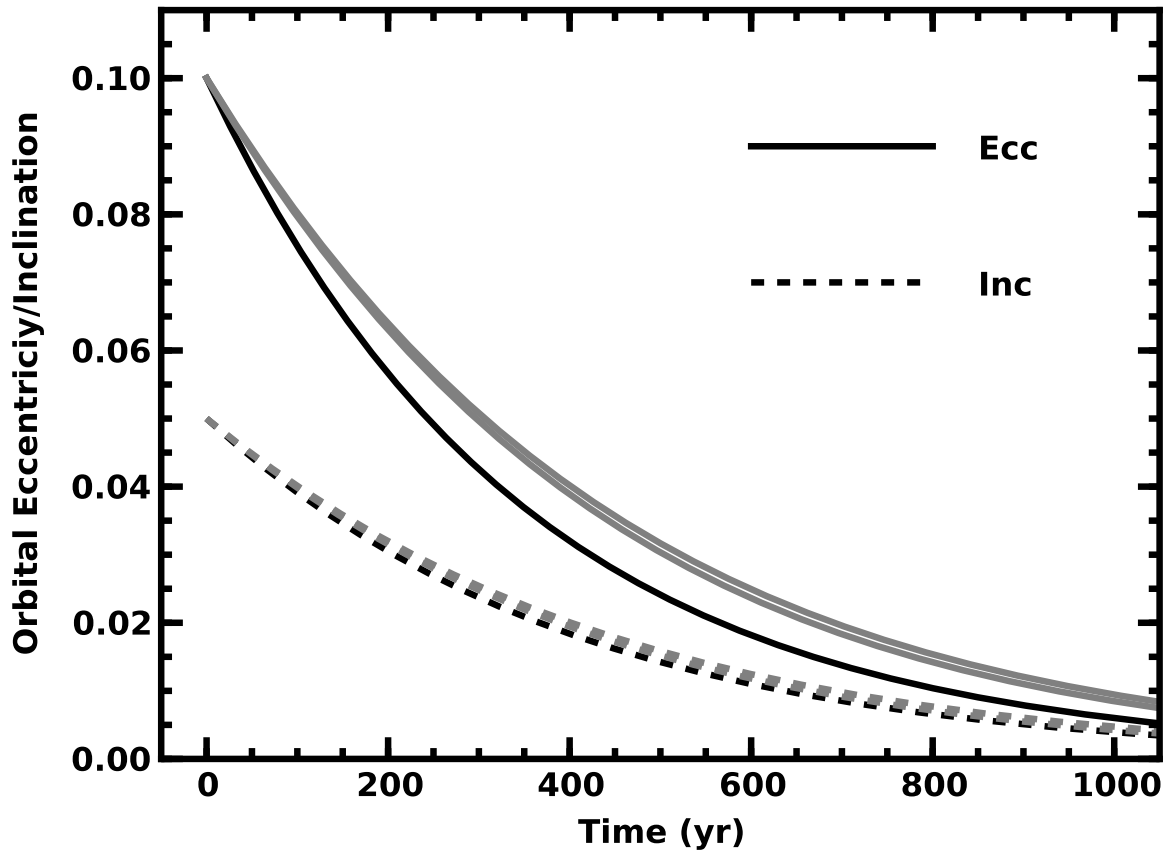


Fig. 21.— Collisional damping within a ring of small particles at 30–35 AU (Levison & Morbidelli 2007). The ring contains $10 M_{\oplus}$ in 1 cm particles. Heavy lines: damping for inelastic collisions. Light lines: damping for elastic collisions with coefficient of restitution $c_0 = 0.99$ (upper line) and $c_0 = 0.01$ (lower line).

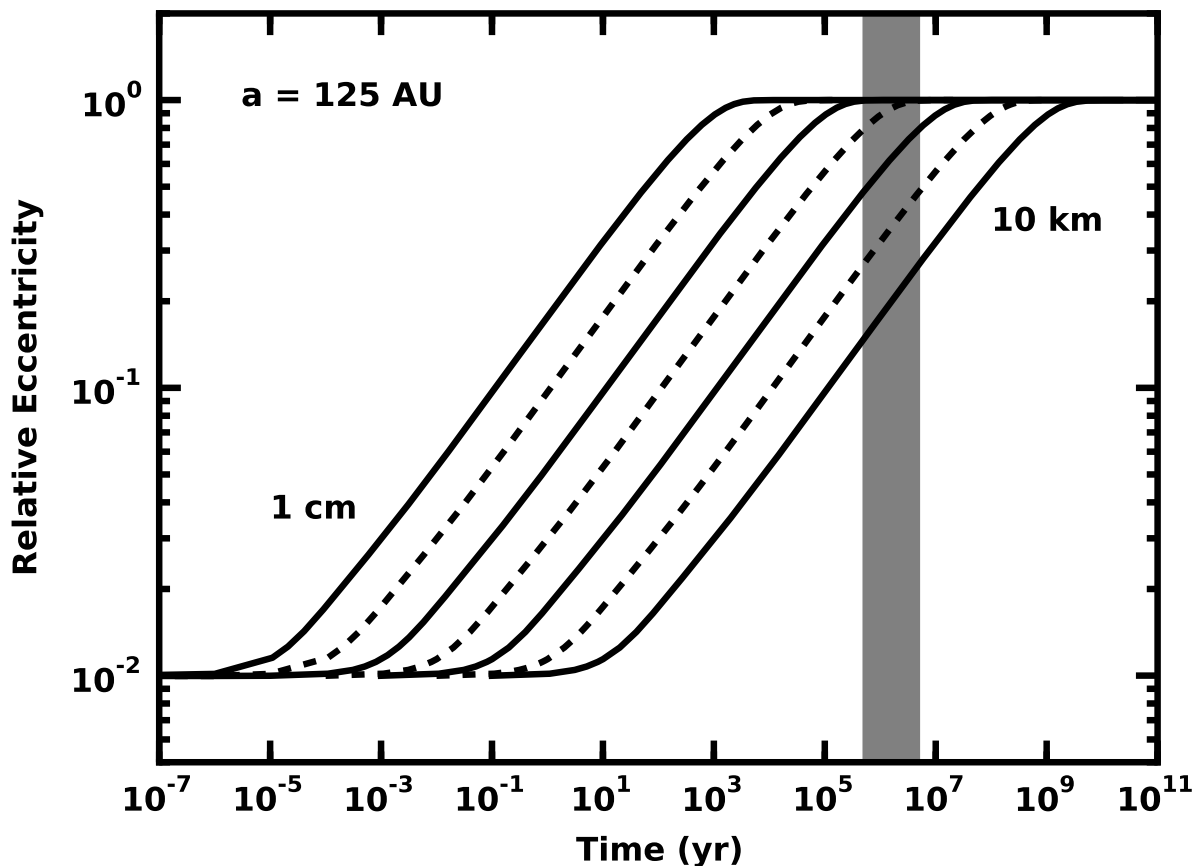


Fig. 22.— Gravitational stirring within a ring of particles at 112.5–137.5 AU. The ring has surface density $\Sigma = 0.0215 \text{ g cm}^{-2}$ and contains $15.8 M_{\oplus}$ in mono-disperse particles. Solid and dashed lines: evolution of the eccentricity e relative to the equilibrium eccentricity $e_0 = 2.38 \times 10^{-4}(R/1 \text{ km})$ for 1 cm, 10 cm, 1 m, 10 m, 100 m, 1 km, and 10 km particles. The time to reach e^{-1} of the equilibrium eccentricity is $t_{stir} = 1.67(R/1 \text{ km}) \text{ Myr}$. Vertical grey bar: epoch of planetesimal formation and gas dispersal in a protoplanetary disk (e.g., Kleine et al. 2009; Dauphas & Pourmand 2011; Williams & Cieza 2011, and references therein).

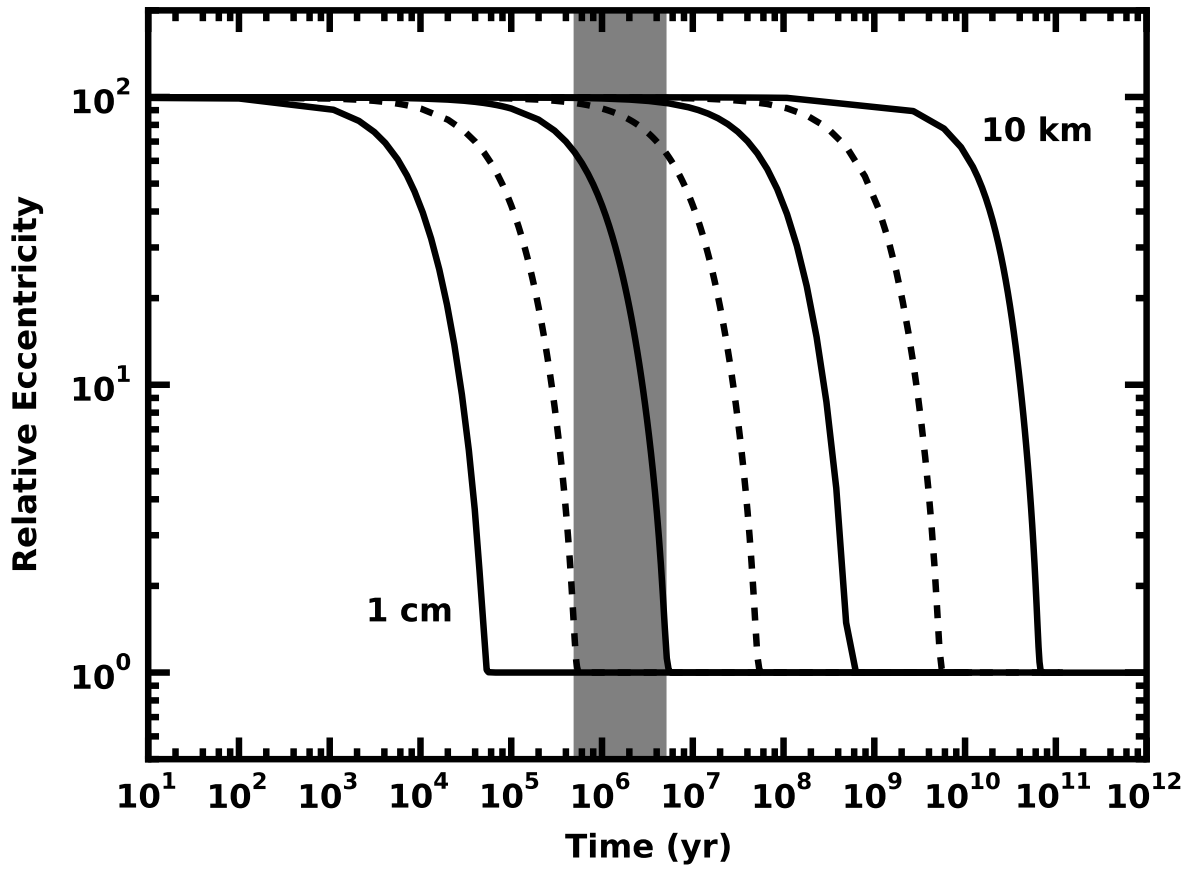


Fig. 23.— As in Fig. 22 for collisional damping. The e -folding time is $t_{damp} = 1.15 \times 10^9 (R/1 \text{ km}) \text{ yr}$.